Automatic 3D extraction of pleural plaques and diffuse pleural thickening from lung MDCT images

Author:

Pazokifard, Banafsheh

Automatic 3D extraction of pleural plaques and diffuse pleural thickening from lung MDCT images

Banafsheh Pazokifard

A Thesis in Fulfilment of the Requirements for the Degree of

Doctor of Philosophy

School of Computer Science and Engineering

Faculty of Engineering

April 2016

To my daughter, Tara.

ABSTRACT

Pleural plaques (PPs) and diffuse pleural thickening (DPT) are very common asbestos related pleural diseases (ARPD). They are currently identified non-invasively using medical imaging techniques. A fully automatic algorithm for 3D detection of calcified pleura in the diaphragmatic area and thickened pleura on the costal surfaces from multi detector computed tomography (MDCT) images has been developed and tested. The algorithm for detecting diaphragmatic pleura includes estimation of the diaphragm top surface in 3D and identifying those voxels at a certain vertical distance from the estimated diaphragm, and with intensities close to that of bone, as calcified pleura. The algorithm for detecting thickened pleura on the costal surfaces includes: estimation of the pleural costal surface in 3D, estimation of the centrelines of ribs and costal cartilages and the surfaces that they lie on, calculating the mean distance between the two surfaces, and identifying any space between the two surfaces whose distance exceeds the mean distance as thickened pleura. The accuracy and performance of the proposed algorithm was tested on 20 MDCT datasets from patients diagnosed with existing PPs and/or DPT and the results were compared against the ground truth provided by an experienced radiologist. Several metrics were employed and evaluations indicate high performance of both calcified pleura detection in the diaphragmatic area and thickened pleura on the costal surfaces. This work has made significant contributions to both medical image analysis and medicine. For the first time in medical image analysis, the approach uses other stable organs such as the ribs and costal cartilage, besides the lungs themselves, for referencing and landmarking in 3D. It also estimates fat thickness between the rib surface and pleura (which is usually very thin) and excludes it from the detected areas, when identifying the thickened pleura. It also distinguishes the calcified pleura attached to the rib(s), separates them in 3D and detects calcified pleura on the lung diaphragmatic surfaces. The key contribution to medicine is effective detection of pleural thickening of any size and recognition of any changes, however small. This could have a significant impact on managing patient risks.

List of Publications

- Pazokifard, B.; Sowmya, A., "Efficient graph cuts based extraction of vertebral column and ribs in lung MDCT images," in *Image Processing (ICIP), 2013 20th IEEE International Conference on* , vol., no., pp.1182-1186, 15-18 Sept. 2013.

- Pazokifard, B.; Sowmya, A., "Lung segmentation with graph cuts: Graph size versus performance," in *AIP Conference Proceedings: Proceedings of Computational Models for Life Sciences (CMLS), 2013 International Symposium on*, vol. 1559, pp. 315-322, 27-29 Nov. 2013.

- Pazokifard, B.; Sowmya, A., "3-D segmentation of human sternum in lung MDCT images," in *Engineering in Medicine and Biology Society (EMBC), 2013 35th Annual International Conference of the IEEE* , vol., no., pp.3351-3354, 3-7 July 2013.

- Pazokifard, B.; Sowmya, A.; Moses, D., "Patient-customized 3D reconstruction of human ribs from lung MDCT dataset," in *Biomedical Imaging (ISBI), 2014 IEEE 11th International Symposium on* , vol., no., pp.1131-1135, April 29 2014-May 2 2014.

- Pazokifard, B.; Sowmya, A.; Moses, D., "Automatic patient-customised 3D reconstruction of human costal cartilage from lung MDCT dataset," *IntJCARS, The International Journal of Computer Assisted Radiology and Surgery*, DOI: 10.1007/s11548-014-1086-9.

- Pazokifard, B.; Sowmya, A.; Moses, D., "Automatic 3D modelling of human diaphragm from lung MDCT images," *IntJCARS, The International Journal of Computer Assisted Radiology and Surgery*, DOI: 10.1007/s11548-015-1298-7.

- Pazokifard, B.; Sowmya, A.; Moses, D., "Automatic 3D extraction of pleural plaque and pleural thickening from lung MDCT images," *to be submitted as a journal article.*

Contents

List of Abbreviations

2D	2 Dimentions
3D	3 Dimentions
ARPD	Asbestos Related Pleural Disease
CADe	Computer Aided Detection
CADx	Computer Aided Diagnosis
CCJ	Costochondral Joint
CT	Computed Tomography
CXR	Chest X-Ray
DICOM	Digital Imaging and Communications in Medicine
Dmean	Distance mean
DPT	Diffuse Pleural Thickening
Drms	Distance root mean square
DSC	Dice Similarity Coefficient
EB	Encompassing Boundary
EM	Expectation Maximization
FN	False Negative
FNR	False Negative Ratio
FP	False Positive
FPR	False Positive Ratio
GMRF	Gibbs-Markov Random Field
HRCT	High Resolution Computed Tomography
ICJ	Interchondral Joint
LCG	Linear Combination of Gaussians
MDCP	Mean Distance to the Closest Point
MDCT	Multi Detector Computed Tomography
MRI	Magnetic Resonance Imaging
PE	Pectus Excavatum
PNG	Portable Network Graphics
PP	Pleural Plaque
PPs	Pleural Plaques
ROI	Region Of Interest
SCJ	Sternocostal Joint
TN	True Negative
TNR	True Negative Ratio
TP	True Positive
TPR	True Positive Ratio
VOI	Volume Of Interest

List of Figures

List of Tables

Chapter 1

Introduction

Asbestos is a silicate mineral that naturally exists on earth. The usefulness and desirable physical properties of asbestos made it a popular material for use in buildings and industries, leading to large scale mining in the past [58]. However, in the late 19th century, the link between prolonged exposure to asbestos and serious and fatal illnesses was confirmed, and since the mid 20th century its usage has been banned in most countries [3].

Prolonged exposure to asbestos can cause serious lung and pleural disorders. Two most common asbestos related pleural diseases (ARPDs) are pleural plaques (PPs) and diffuse pleural thickening (DPT) [13, 54, 112]. PP is defined as localised pleural thickening, induced by asbestos, and DPT refers to more generalised pleural thickening [60, 85]. PPs and DPT occur on the pleura and may eventually become calcified. The diaphragm is another potential organ for PP involvement [22, 85, 95].

Usually DPT shows no symptoms, however it may manifest as breathlessness and chest pain. On the other hand, PPs cannot be detected clinically, and can only be identified non-invasively using medical imaging techniques. Therefore medical imaging is necessary for diagnosis of both DPT and PPs. Computed tomography (CT) is the preferred imaging modality, as it can detect small calcified plaques, as well as non-calcified plaques/regions of mild DPT that are difficult to appreciate on chest X-ray (CXR). Multi-detector CT (MDCT) imaging, a new technology that acquires multiple high resolution CT images by a rotating x-ray tube, is currently

used in modern radiology centres for the purpose of chest imaging.

Detecting PPs of all sizes is important, because a tiny plaque signifies the same risk for developing more complicated lung disorders as extensive plaques [136]. Besides, PPs may involve diaphragmatic pleura and can range in size and number. Although extensive PPs and DPT are recognised easily on CT, the diagnosis of small or non-calcified plaques can easily be missed. A robust and accurate automated method for detecting PPs and DPT is a valuable goal that could have significant impact on managing and assessing patient risks. Also, automated and accurate measurement of the degree and area of pleural thickening would allow detection of any changes over time.

Despite the importance of accurate and automated methods for detecting PPs and DPT, not many works and techniques have been reported to date. As far as is known, detection of thickened pleura in the diaphragmatic area has not been reported.

Few techniques have been reported for detection of PPs and DPT on the pleural costal surfaces. The first technique reported [117] extrapolates and labels pixels beyond the pleura and lying on lung centroid radial lines, as rib, spine, fat or thickened pleura, based on the pixel intensity. Although the work is based on anatomy pre-knowledge, the approach for identifying PPs attached to the ribs is not clarified. In addition, as the fat layer may or may not be visible in CT images, differentiating between fat layer and thickened pleura is not highly reliable.

The other approach to detect PPs and DPT relies on the difference between the existing lung contour and its relaxed boundary to simulate the healthy pleura. The patient's normal pleural contour is estimated by convex hull algorithm [32], spline-based interpolation [34] and Gibbs-Markov random field (GMRF) relaxation [30]. The false positive error rate may be high in these approaches as human ribs naturally put pressure on the lungs and cause indentation on the lung surfaces. Furthermore, the formation of pleural thickening sometimes does not make a depression/dent on a section of the lung border and therefore, portions of existing PPs and/or DPT may be missed when subtracting the real lung contour from its estimated normal shape.

1.1   Thesis Goal

There is a need for accurate methods to detect PPs and DPT on the pleural costal surface and diaphragmatic area. The focus of this thesis is on automatic 3D extraction and accurate quantification of PPs and DPT from lung MDCT images.

1.2   Thesis Scope

The methodology used to develop the automatic algorithms is based on image processing and computer vision techniques. The study is limited to lung MDCT datasets, acquired from Medical Imaging Department, Prince of Wales Hospital, Sydney, NSW, Australia. An expert radiologist from the department marked the groundtruth and verified the results of the algorithms. Accuracy and performance of the algorithms were measured by appropriate metrics commonly used for evaluating similar techniques. The algorithm for detecting ARPD were tested on 20 datasets of patients diagnosed with PPs and/or DPT. Other proposed algorithms, employed as preliminary stages of ARPD detection, were tested on up to 50 MDCT datasets that were acquired for different medical reasons.

1.3   Thesis Overview

In order to detect PPs and DPT in 3D from a patient's MDCT dataset, two different lung areas are analysed with different approaches: diaphragmatic area and pleural costal surfaces.

For detecting calcified pleura in the diaphragmatic area, the diaphragm top surface is modelled in 3D. Next, areas within a certain vertical distance of the estimated surface are investigated for existing calcified pleura.

A high-level description for automatic PP and DPT detection on the pleural costal surfaces is shown in Figure 1.1. The basic idea is to measure $\overline{\mathbb{D}}$, the mean distance between pleural costal surfaces and rib centre-lines (see Figure 1.1b for

illustration of $\mathbb{D}$), and identify the locations in 3D where the distance $\mathbb{D}$ is relatively larger than $\overline{\overline{\mathbb{D}}}$. Comparisons are in cylindrical coordinate system (as shown in Figure 1.1c) between two layers:

(i) an outer layer as the stable comparison reference, which is a surface fitted to the centrelines of the ribs and costal cartilages ($\mathbb{O}$uter$\mathbb{L}$ayer hereafter)

(ii) an inner layer as the compared component, which is the pleural costal surface in 3D ($\mathbb{I}$nner$\mathbb{L}$ayer hereafter).

As mentioned earlier, any algorithm based on analysing the pleural surface to detect the pleural thickening may miss portions of thickened pleura. Moreover, since a rib puts pressure on the pleural surface and usually makes it indented, analysing the pleural surface to detect pleural thickening may dramatically increase the false positive error rate. Using the ribs as a stable reference for analysing pleural costal surfaces improves accuracy. Due to changes in size and shape of the rib cross-section along its length [96], instead of the rib surface, its centre-line is chosen as the stable and reliable reference.

When analysing a patient dataset that includes calcified pleura, there is a subtlety which may be overlooked and has not been considered in the literature. Usually calcified pleura are attached to a rib or series of ribs and it is a challenging task to automatically distinguish them during chest bone segmentation. Such a situation causes two problems: (i) error in rib centre-line estimation and (ii) calcified pleura identified as part of the rib (see Figure 1.2 for 2D and 3D examples).

Separation of the calcified PP from the rib(s) in 3D is achieved in three steps:

(i) cut the cross-section of the rib, where it is attached to the calcified plaque (see Figure 1.1e)

(ii) reconstruct the rib based on patient's anatomy (see Figure 1.1f)

(iii) subtract the reconstructed rib from primary segmented bone (see Figure 1.1g).

To accomplish the above, segmentation of the lung, ribs, sternum and reconstruction of the ribs and costal cartilage based on patient's anatomy as well as modelling
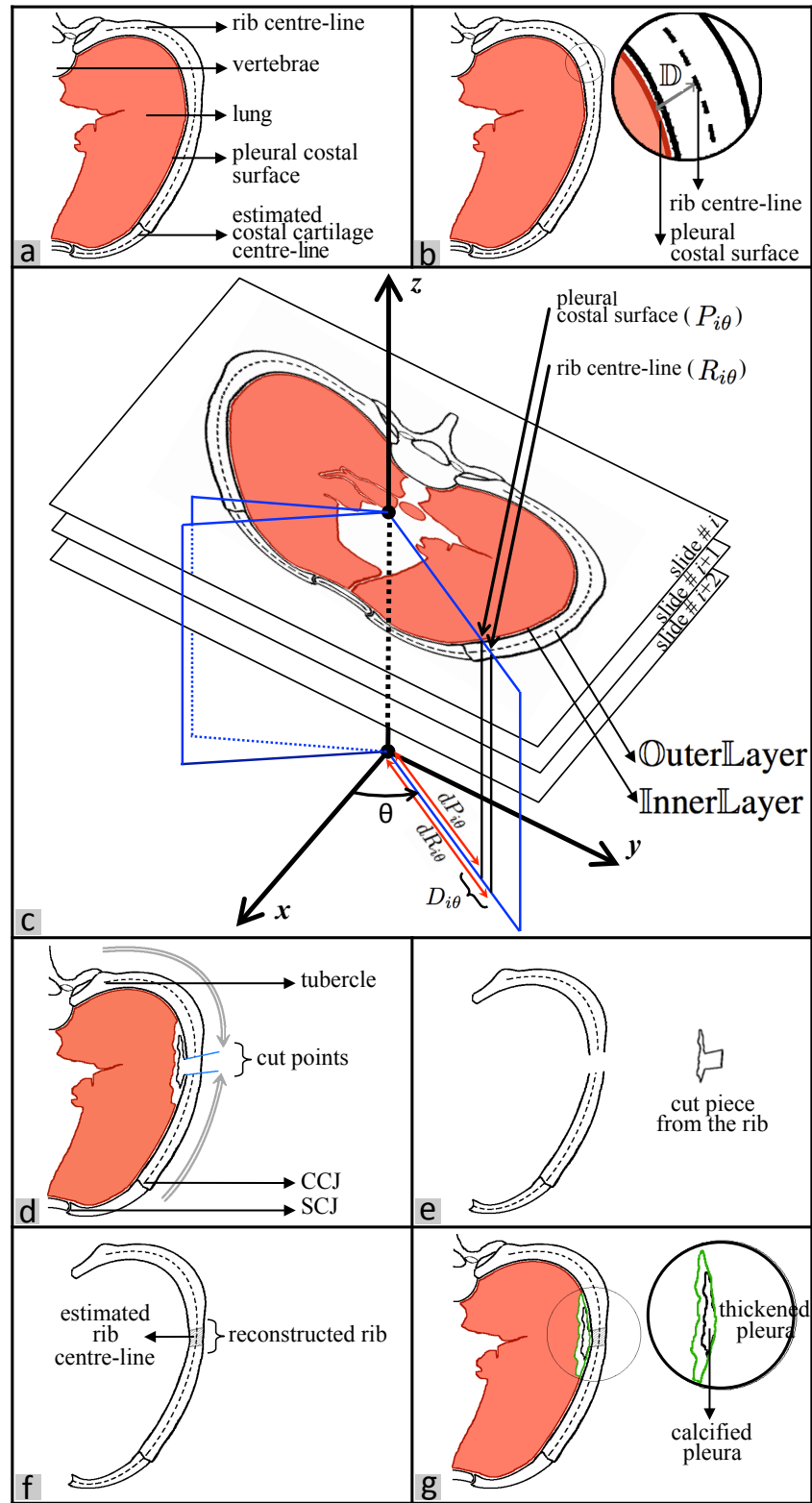
Figure 1.1: High-level description for detecting thickened pleura on the pleural costal surfaces: (a) anatomical notation for a lung cross-section at axial direction, (b) $\mathbb{D}$ is defined as the distance between a rib's centre-line and pleural costal surface, (c) illustration of cylindrical coordinate system, used in proposed algorithm, (d) calcified pleura attached to the rib and cut points, (e) removed calcified pleura from the rib structure, (f) patient-customised reconstructed rib and (g) segmented calcified pleura and detected thickened pleura.
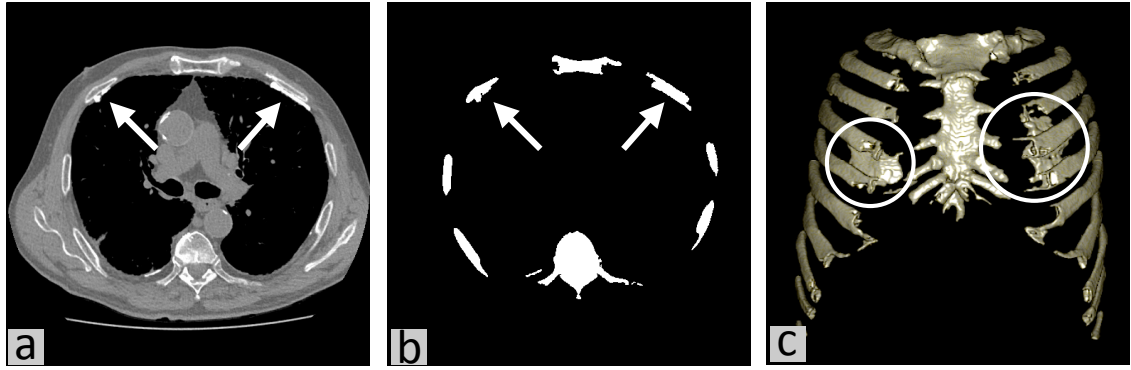
Figure 1.2: Calcified pleura attached to ribs: (a) slide number 197 of a test dataset, calcified pleura attached at two points, pointed to by white arrows, (b) and (c) results of bone segmentation in 2D and 3D (half-front coronal view) which show how calcified pleura at two locations are mis-segmented as parts of rib structure.

of the diaphragm are necessary. All these steps are performed in 3D and their performance evaluated separately by testing on a large number of MDCT datasets.

1.4   Thesis Contributions

The presented method for detecting the thickened pleura from MDCT images contributes to medical image analysis by identifying the attached calcified pleura to a rib or series of ribs and separating it in 3D, detecting the calcified pleura at lung diaphragmatic surfaces for the first time and also using stable organs i.e. ribs and costal cartilage, besides a patient's lung features, for the purpose of landmarking in 3D.

The main contributions of the presented technique to medicine includes accurate measurement of the degree and area of pleural thickening to detect any changes over time and detecting PPs of all sizes, that play an important role in patient risk management

1.5   Thesis Organisation

Asbestos and respiratory issues due to long term exposure to asbestos are reviewed in Chapter 2. The basics of X-ray CT imaging and MDCT, anatomical terms, asbestos

related pleural disease (ARPD), PPs and DPT pathological features and also current approaches in medical science for their diagnosis are included in the chapter. Current knowledge, methodological contributions as well as the gaps in the literature for segmenting and modelling different organs, necessary for detecting thickened pleura in CT images, are discussed and the chapter ends with key elements of performance evaluation.

Algorithms for 3D segmentation of the lungs, ribs, vertebral column and sternum as well as costal notches localization in 3D are presented in Chapter 3. All presented techniques are necessary steps for detecting PPs and DPT in MDCT datasets. Experiments to evaluate the algorithms performance are explained at the end of the chapter, followed by discussion of the achieved results.

Frameworks and techniques for ribs and costal cartilage reconstruction and diaphragm modelling in 3D are provided in Chapter 4. The algorithms provide important information for automatic detection of thickened pleura. The performance of the algorithms was evaluated, using several criteria. Outcomes of experiments are presented and discussed at the end of the chapter.

In Chapter 5, comprehensive details of the technique to detect calcified pleura in the diaphragmatic area and thickened pleura on the costal surfaces from a lung MDCT dataset are provided. The chapter includes a detailed flowchart with an example for each step. Several experiments performed to measure the accuracy and performance of the detection algorithm are provided and discussed at the end of the chapter.

In Chapter 6, a summary of contributions made to medical image analysis and medicine is provided. Future work and limitations to be investigated are discussed as well and the chapter ends with concluding remarks.

Chapter 2

Asbestos Related Pleural Disease and Its Detection

Two of the commonest disorders of asbestos related pleural disease (ARPD) are pleural plaque (PPs) and diffuse pleural thickening (DPT) [13, 54, 112], both of which affect the lung pleura, the membrane around the lungs. These two disorders are categorised as non-malignant and currently are identified non-invasively, using medical imaging techniques. This thesis develops automatic detection techniques for PPs and DPT in 3D from lung multi detector computed tomography (MDCT) images. Relevant background knowledge, terms and concepts that are necessary to understand the methods are presented in this chapter. In addition, related works in PPs and DPT detection are discussed and the challenges and gaps in literature are analyzed.

In section 2.1, anatomical terms are defined and human organs involved in the algorithms for PPs and DPT detection are briefly discussed. Asbestos, lung disorders and issues related to long term exposure to asbestos are described in section 2.2. The section also describes pathological features of PPs and DPT and current approaches in medical science for their diagnosis. The basics of X-ray CT imaging and MDCT, the new technology for CT scanning, are described in section 2.3.

As clarified in Chapter 1, several steps are necessary to detect PPs and DPT in a lung MDCT dataset. These include segmentation of the lungs, sternum, ribs and

vertebral column, reconstruction of the ribs and costal cartilages and modelling of the diaphragm. Current knowledge, methodological contributions and the gaps in the literature are reviewed in section 2.4. The section also presents used methods and techniques for detecting thickened pleura in the pleural diaphragmatic area and pleural costal surface.

The final section of the chapter includes description of techniques. The theory behind the main algorithms in use, namely graph cut, region growing, active contours and smoothing splines, are explained in sub-section 2.5.1. Key elements of performance evaluation including the test dataset and evaluation metrics are discussed thereafter in sub-section 2.5.2. The chapter concludes with brief remarks in section 2.6.

2.1 Anatomy of the Human Upper Trunk

The trunk is the anatomical term employed for the central part of the human body and includes the thorax (chest) and the abdomen. The chest contains the most critical organs such as the heart and lungs. The abdomen contains the major organs responsible for digestion, including the liver and kidneys. In the following sections, the organs involved in PPs and DPT detection are briefly described.

2.1.1 Respiratory System

Ventilation or the air-breathing process in animals, including humans, occurs in two steps: inhalation and exhalation. The anatomical organs associated with breathing include the trachea, bronchi, bronchioles, lungs (covered by pleura) and the diaphragm.

2.1.1.1 Trachea, Bronchi and Bronchioles

The trachea is a moveable cartilaginous and membranous tube, which begins from the sixth cervical vertebra (see Figure 2.1a), and ends at the upper border of the
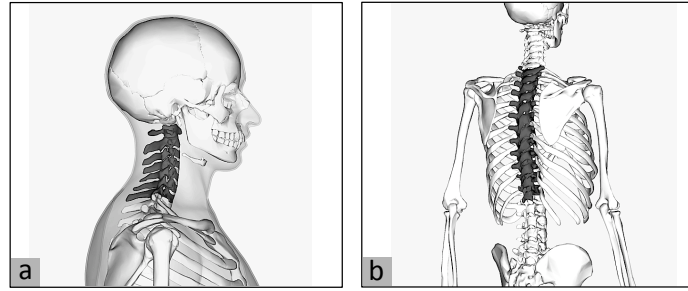
Figure 2.1: (a) Cervical vertebrae are immediately below the skull [11] and (b) thoracic vertebrae are blow the lowest cervical vertebra [12].
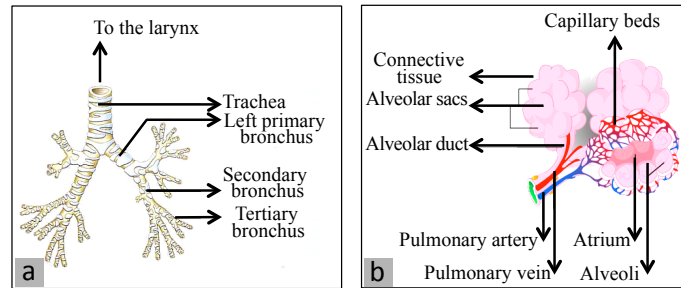
Figure 2.2: (a) Dstribution of respiratory tree [50] and (b) alveolus diagram [40].

fifth thoracic vertebra (see Figure 2.1b) by dividing itself into the main left and right bronchi, one for each lung (see Figure 2.2a) [128]. In air breathing process, air follows from the larynx, the organ protecting the trachea against food aspiration, into the main (primary) bronchi. Next, air goes into the lobar (secondary) and segmental (tertiary) bronchi which then branch into smaller bronchi and bronchioles (see Figure 2.2a) [87]. Each terminal bronchiole divides into two or three respiratory bronchioles, which then divide into two or three alveolar ducts as well [55]. In the respiratory part of the lung, the blood flows in capillaries, which are the smallest of blood vessels, and in alveoli wall (see Figure 2.2b) [122]. Alveoli, with polyhedral structure, are groups of small pouches which are placed around alveolar sacs, alveolar ducts and respiratory bronchioles [122].

2.1.1.2 Pleura

Each lung is covered by the pleura, a serous membrane in the form of a flattened sac [87]. The outer and the inner layers of this sac are called parietal pleura and visceral pleura respectively (see Figure 2.3a) [87]. The space between the parietal pleura and
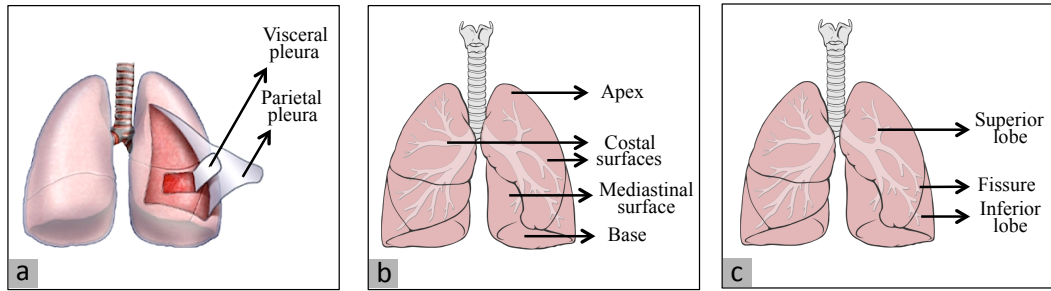
Figure 2.3: Anatomy and terminology of the lung [7, 86].

visceral pleura, called the pleural cavity, is filled with a thin layer of pleural fluid and is maintained at negative pressure [50]. This negative pressure helps the lungs to stay attached to the thoracic wall tightly, and as the capacity of the thoracic cavity increases and decreases during breathing, air gets in and gets out the lung [87].

2.1.1.3 Lungs

The lungs are the vital parts of respiration [50]. As shown in Figure 2.3b, each lung with the shape of a half cone has an apex, base, two surfaces (costal and mediastinal) and three borders (inferior, posterior and anterior) [50]. They are positioned on each side of the mediastinum, surrounded by the ribs and surrounding the heart and great blood vessels [128]. The right and left lung are divided into three and two lobes respectively by the fissures (see Figure 2.3c) [97] and except for their roots to the mediastinum, are suspended freely in the pleural cavity [50].

2.1.2 Diaphragm

The thoracic diaphragm is a double dome- or parachute- shaped sheet of muscle and is located under the lungs and surrounded by the ribs and costal cartilages, and partially the spinal column at the back (see Figure 2.4) [50]. The diaphragm separates the thoracic and abdominal cavities and serves as the main muscle in respiration. It also plays an important role in localizing and separating other organs in the thorax and the abdominal cavity.

In X-ray CT images, there is low contrast between the diaphragm and adjacent organs. In Figures 2.5a to 2.5c, low contrast boundary between the diaphragm and
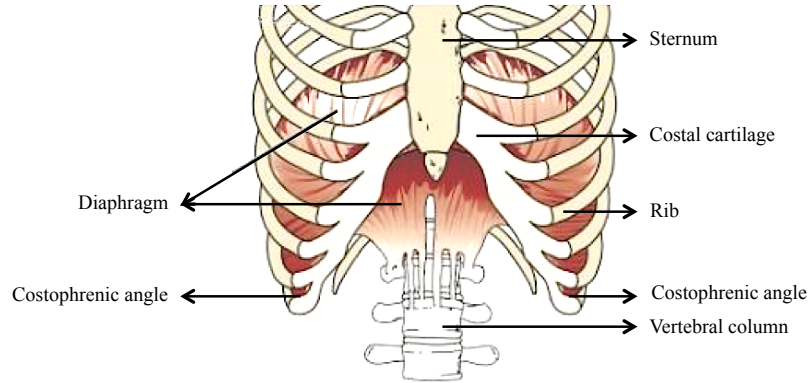
Figure 2.4: Human diaphragm is located under the lungs and surrounded by the ribs and costal cartilages, and partially the spinal column at the back [70].
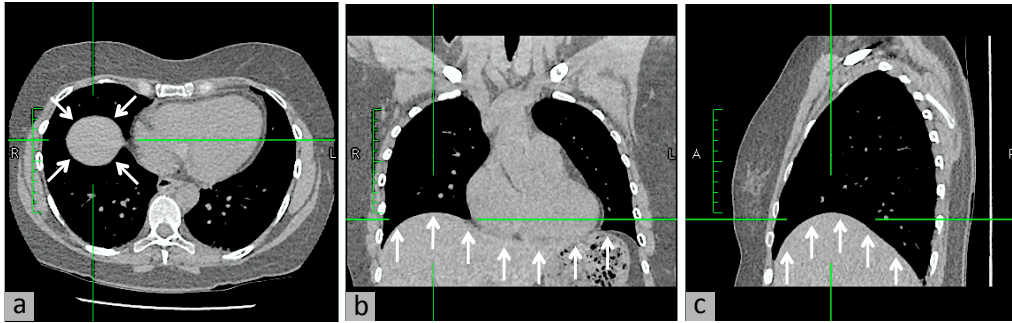
Figure 2.5: (a) to (c) location of the diaphragm in axial, coronal and sagittal directions are shown with arrows (images are chosen from test datasets).

surrounding organs is indicated with arrows.

2.1.3 Upper Trunk Skeleton

The trunk, also called the torso, is an anatomical term that refers to the central part of the human body and is divided into the thorax and abdomen. The upper trunk includes critical organs such as the heart and the lungs, which are protected by the rib cage. The upper trunk skeleton includes the ribs, vertebral column, clavicles, scapulas, humerus and the sternum (see Figure 2.6).

2.1.3.1 Ribs

The ribs are 12 pairs of long curved bones that form a cage to support the internal organs in the upper trunk. A rib articulates with a vertebra at the tubercle, a junction between the neck and head of the rib (see Figure 2.7). In human anatomy,
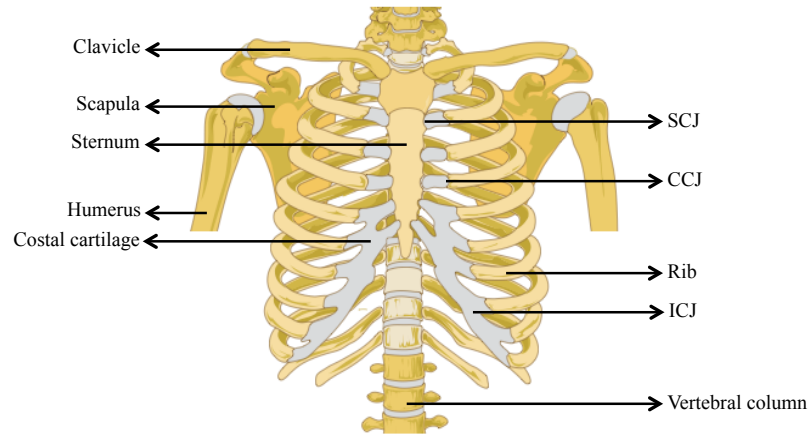
Figure 2.6: Upper trunk skeleton [141].
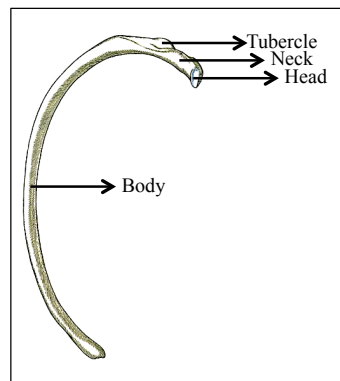
Figure 2.7: Illustration of a human rib [50].

the first seven ribs are known as "true ribs" and the others are "false ribs". True ribs and the first three false ribs are connected to the sternum through direct costal cartilage attachment or by sharing a cartilaginous connection respectively. Ribs number eleven and twelve are called floating ribs as their heads are connected to the vertebrae only and the other ends are not attached to the sternum [101].

The first rib has rather different geometry than the other ribs as it is broad, horizontally flat and has the highest curvature. Ribs three through nine share the most features. In general, human ribs increase in length from ribs one through seven and decrease in length again through to rib twelve. Ribs vary in direction. The upper ribs are less oblique than the lower ones and the obliquity reaches its maximum at the ninth rib and then decreases to the last rib [50].
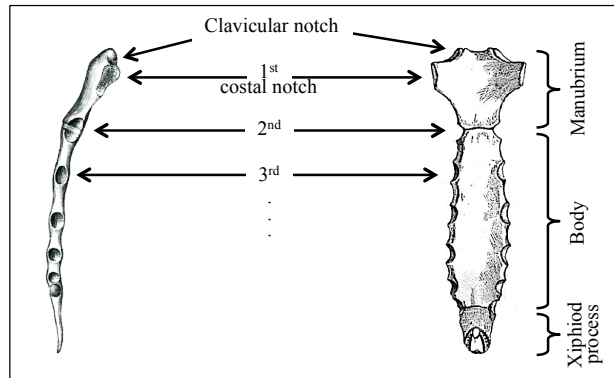
Figure 2.8: Illustration of anterior projection and lateral projection of human sternum [50].

2.1.3.2   Sternum

The sternum is a thin, flat, elongated bone. It is located anteriorly in the centre of the chest and helps to protect the inner vital organs from physical trauma. The upper end of the sternum supports the clavicles. The sternum has seven costal notches, called sternocostal joints (SCJs), on each side for articulation with the costal cartilages of ribs 1-7 (see Figures 2.6 and 2.8). Its average length in the adult is about 17 cm [50].

The sternum consists of three bony parts, connected by two joints (see Figure 2.8). From top to bottom, the three parts are called the manubrium, body and xiphoid process. The first two parts have a bony structure while the last one is cartilaginous in structure in youth and becomes calcified with age [99].

2.1.4   Costal Cartilage

The costal cartilages are bars of cartilage that prolong the ribs forward in a way that facilitates the chest wall elasticity [99]. As shown in Figure 2.6, the first seven costal cartilages are directly connected to the sternum, while the following three are joined to the lower border of the preceding cartilage via interchondral joints (ICJs). The last two costal cartilages end in the wall of the abdomen [50]. The joints between the ribs and costal cartilages are called costo-chondral joints (CCJs).

Like those of ribs, the lengths, directions and curvatures of the costal cartilages

vary. From the first costal cartilage to the seventh, the lengths increase and then gradually decrease to the twelfth. The first and third costal cartilages slightly descend and ascend respectively, while the second one is horizontal and the rest angular [99].

2.2   Asbestos Related Pleural Disease

Asbestos is a silicate mineral that has been used worldwide in more than 3000 applications. Its desirable physical properties such as heat, fire and electricity insulation, flexibility, low price and tensile strength made it one of the popular materials used in buildings and industries in the past [58]. However, in early 1900 a large scale death and lung problems were noticed in a asbestos-mining towns [93] and in the late-19th century, the link between prolonged exposure to asbestos and death or serious disease was confirmed. Until the mid 20th century, public awareness of the dangers of asbestos kept increasing, and since then its usage has been banned in most countries. Australia was one of the highest users of asbestos in the world until it was banned in the mid 1980s [3].

2.2.1   Epidemiology

According to the world health organisation (WHO), more than 107,000 deaths each year can be attributed to occupational exposure to asbestos and despite the widespread ban of asbestos, approximately 125,000,000 persons are currently exposed to asbestos at the workplace [2]. It is expected that the rate of mortality and morbidity attributable to asbestos exposure will rise in future [112].

It is now known that prolonged exposure to asbestos can cause serious lung disorders including lung cancer, asbestosis, malignant mesothelioma, rounded atelectasis, benign asbestos pleural effusion, PPs and DPT [112]. The most common ARPDs, are PPs (up to 58% and 8% of the disorders from exposure at the workplace and general environment respectively) and DPT (22% of the disorders) [13, 54, 112].
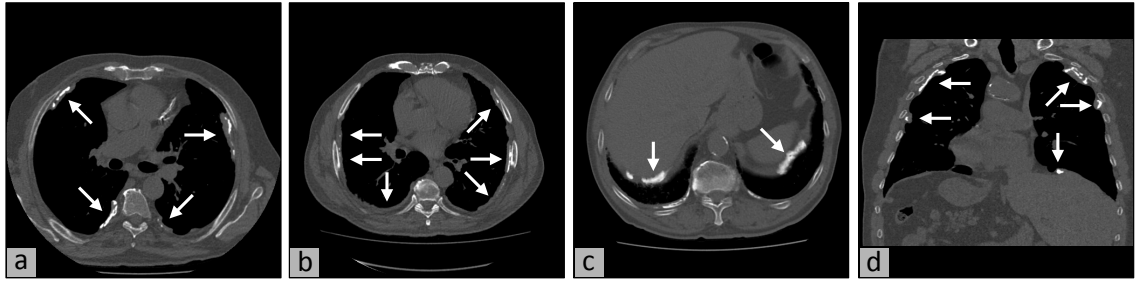
Figure 2.9: Examples of PPs and DPT in real patient studies: (a) PPs, multiple calcified and partially calcified PPs involving the costovertebral pleura bilaterally (b) DPT, regions of diffuse thickening of the costovertebral pleura (c) diaphragmatic PPs, calcified PPs involving the diaphragmatic pleura bilaterally and (d) PPs (coronal direction view), multiple calcified PPs involving the costovertebral pleura bilaterally and the right diaphragmatic pleura (images are chosen from test datasets).

2.2.2 PPs and DPT Pathological Features

PPs are defined as localised pleural thickening, induced by asbestos; it is called DPT if the thickening is more generalised [60, 85]. Both PPs and DPT are prominent in the lower half of the thorax [48] and may eventually become calcified. PP follows the course of the ribs at the posterior and lateral walls of the thoracic cage [22], over the fifth to the ninth rib, and rarely extends superior to the third rib [85]. The diaphragm is another potential organ for PPs involvement [22, 85, 95]. DPT occurs on the lower parts of the pleura and, in contrast to PPs, almost always involves the costophrenic angles (the angle at which the diaphragm and the chest meet, see Figure 2.4) [85]. Examples of PPs and DPT from real studies are shown in Figure 2.9.

2.2.3 Medical Approaches to PPs and DPT Diagnosis

PPs cannot be detected clinically, and can only be identified non-invasively using medical imaging techniques. DPT is usually asymptomatic, but uncommonly results in clinical manifestations such as breathlessness and chest pain [95]. Although large PPs and extensive DPT can be diagnosed with a chest x-ray (CXR), computed tomography (CT) is the preferred imaging modality because it can detect small calcified plaques, and also non-calcified plaques/regions of mild DPT that are difficult to appreciate on CXR. CT has an accuracy greater than 95% in detecting PPs and

DPT [119]. CT is also more accurate in detecting changes in PPs and DPT, and assessing for the development of other complications of asbestos exposure including mesothelioma and lung cancer.

It is well demonstrated in the literature that the presence of PPs relates to asbestos exposure, which in turn relates to the risk of developing more sinister asbestos related diseases such as asbestosis, mesothelioma an lung cancer. Somewhat paradoxically, however, the surface volume of plaques has been found not related to cumulative asbestos exposure [136]. Therefore the presence of a tiny plaque signifies the same risk for these sinister complications as that of extensive plaques. It is therefore important to detect plaques of all sizes. In addition, patients with calcified PPs who also have other risks of lung cancer should be screened. Some risk factors for increased risk of lung cancer include cumulative exposure to tobacco, age, and exposure to other lung carcinogens such as silica and radon.

PPs involve principally the costovertebral and diaphragmatic pleura and can range in size and number. Extensive disease is easy to recognise on CT, but where there is only small or non-calcified plaques, the diagnosis can easily be missed, particularly in chest CTs performed for other reasons. Having a robust accurate automated method for detecting PPs and DPT is important in identifying patients at risk of the more sinister complications of asbestos exposure. As many patients have chest CT scans for other reasons, the ability to screen these studies automatically, and detect PPs and DPT could have a significant impact on managing patient risk.

In addition, mesothelioma, which is a dreaded complication of asbestos exposure, usually appears as an area of pleural thickening in the early stages. Automated and accurate measurement of the degree and area of pleural thickening would allow detection of any changes over time. These changes can then be screened by a radiologist to assess the risk of newer regions resulting from mesothelioma. This would be of great benefit to the patient because as with any cancer, the earlier the detection and treatment, the better the prognosis.
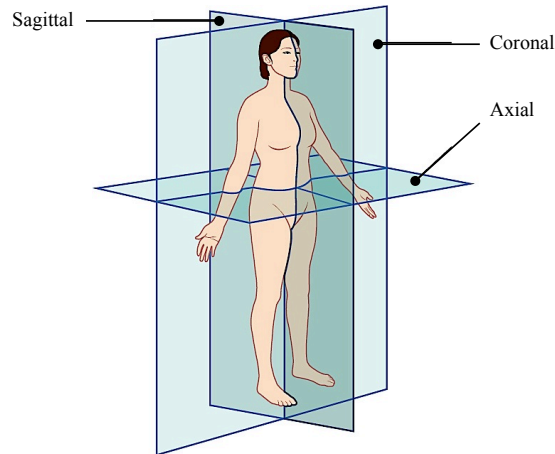
Figure 2.10: Anatomical planes, referring to two-dimensional sections of the body: axial, coronal and sagittal [79].

2.3 Computed Tomography Imaging

X-ray computed tomography (CT) is generated by an X-ray source that rotates around the object, acquires X-ray images from different angles and uses computer processing to create cross-sectional slides. The slides produced are called tomographic images (virtual slices) and they provide more detailed information than plain X-rays do [132].

High resolution computed tomography (HRCT) is CT at very high resolution. Although HRCT is performed using a conventional CT scanner, the imaging parameters are chosen to maximize spatial resolution. To perform a chest scan with a conventional CT scanner and ensure contiguous chest coverage in a reasonable time period, HRCT is performed at widely spaced sections (e.g. 10mm thick). On the other hand, scan parameters for conventional and HRCT examinations are different and if both images are required for a patient, the scanning has to be performed sequentially. To address these issues, modern multi-detector computed tomography (MDCT) scanners are able to solve the interdependency, and also perform a fast full resolution imaging.

Figure 2.11: Toshiba Aquilion PRIME MDCT scanner [1].

2.3.1   MDCT Technology

In MDCT technology, the number of detectors is increased and the scan acquisition time is reduced. MDCT images are reconstructed afterwards from the volumetric raw data and sections are selected with 1 mm thickness. As CT scanners acquire data as isotropic voxels, images can be viewed in all imaging planes i.e. axial, coronal and sagittal (see Figure 2.10 for plane directions) [4]. Images in the different directions have similar spatial resolution, which facilitates the employment of 3D visualization tools e.g. OsiriX [5].

MDCT scanning is performed in hospitals or special outpatient clinics. To perform the scan, the patient is asked to lie down on a table connected to the MDCT scanner and the table slowly moves inside the machine. During imaging, the scanner arches around the patient's body but does not touch it. The exam is painless. In Figure 2.11 the Toshiba Aquilion PRIME MDCT scanner is illustrated.

2.3.2   MDCT Dataset

Acquired data from MDCT scanners can be saved as an object in the digital imaging and communications in medicine (DICOM) format. DICOM is a standard format for handling, storing, printing and transmitting information in medical imaging. Besides to pixel data, a DICOM image includes additional patient information in a loader. To save a DICOM image, 16 bits are used. The image can be converted
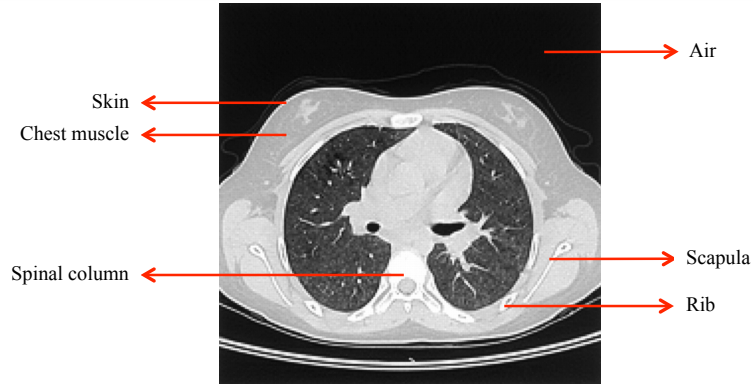
Figure 2.12: An example of normal lung MDCT image, chosen from a test dataset.

to a conventional grayscale image e.g. portable network graphics (PNG), and pixel values from 0 (air) to 255 (bone structure). An example of a normal lung MDCT image is shown in Figure 2.12.

A typical chest DICOM image is 512×512 pixels and for a patient of normal height, approximately 400 slices are required to cover the complete chest. In other words, the size of a typical chest MDCT dataset is 512×512×400 pixels.

2.4 ARPD Detection Methods, Challenges and Gaps

To detect the PPs and DPT in a patient lung dataset, different organs need to be either segmented or modelled in 3D. The steps required to deliver the final results include reconstruction and modelling of the ribs, costal cartilage and diaphragm and also segmentation of the lungs, sternum, ribs and vertebral column in 3D.

Current approaches to 3D detection of PPs and DPT in a lung dataset, the challenges and gaps are reviewed in section 2.4.1. State of the art algorithms for segmenting and modelling the organs are described in sections 2.4.2 and 2.4.3 respectively.

2.4.1   PPs and DPT Detection in 3D

As far as can be ascertained, not many works and techniques have been reported to date for automatic detection of PPs and DPT from medical images. Current methods for detecting PPs and DPT in the diaphragmatic area and pleural costal surfaces are discussed in sections 2.4.1.1 and 2.4.1.2 respectively.

2.4.1.1   Detection in the Pleural Diaphragmatic Area

Due to the nature of the diaphragm i.e. its low thickness, irregular shape and low contrast between the diaphragm and surrounding organs, not only has modelling of the diaphragm remained a challenging task [109], but also detection of thickened pleura in the diaphragmatic area has not been reported in the literature to date.

2.4.1.2   Detection on the Pleural Costal Surfaces

A technique for detection of PPs and DPT has been reported [117]. In the first step, the algorithm identifies different organs including ribs, spine, lungs and mediastinum area and then the boundary of each lung is determined. In the next step, lung centroid radial lines are extrapolated beyond the pleura and pixels lying on the dilated line are labelled as rib, spine, fat or thickened pleura based on the pixel intensity. Although the proposed algorithm [117] uses anatomy pre-knowledge of different organs and their landmarks on CT images, the approach to identify the calcified PPs attached to the ribs, is not clarified. Also differentiating between the fat layer and thickened pleura is not highly reliable due to the fact that the fat layer may or may not be visible in CT images.

In other proposed techniques, pleural thickening is detected by differentiating between the existing lung contour and modelled healthy pleura, estimated by the convex hull algorithm [32], spline-based interpolation [34] and Gibbs-Markov random field (GMRF) relaxation [30]. Detected pleural thickening based on these has been used [31, 33, 44, 45, 46] for follow-up assessment of the disorder. Later, the extracted pleural thickening is modelled [35] by 3D thin plate spline interpolation for illustration
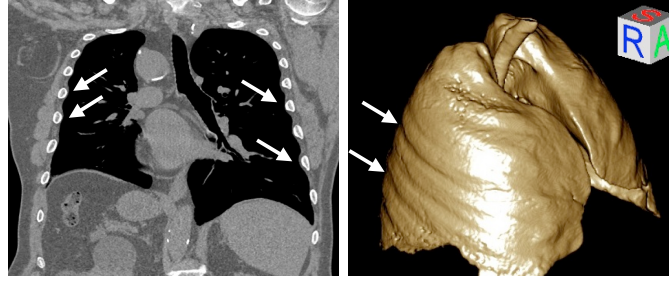
Figure 2.13: Examples of how ribs naturally cause indention on the lungs' surface. Pressure of the ribs on lungs on both 2D and 3D images are marked by white arrows (images are chosen from test datasets).

and for calculating the volume. The proposed methods [30, 34, 32] and other works rely on the difference between the existing lung contour and its relaxed boundary. The drawbacks of this approaches are:

(i) the rate of false positive error may be high as human ribs naturally put pressure on the lungs and cause indention on the lung surfaces (see Figure 2.13 for examples in 2D and 3D)

(ii) occasionally the formation of pleural thickening does not make a depression/dent on a section of the lung border. For instance, as shown in Figure 2.14, the existing left lung contour (Figure 2.14c) and its convex hull (Figure 2.14d) are almost similar, and a big portion of the PP is missed when subtracting the real lung contour from its convex hull (Figure 2.14e). In Figure 2.14f, manually marked PPs by an experienced radiologist are shown.

2.4.2 Automatic Segmentation and Extraction in 3D

Segmenting lungs, ribs, vertebral column and sternum in 3D are necessary steps for detecting PPs and DPT. Current methods for extracting mentioned organs are discussed in sections 2.4.2.1 to 2.4.2.3.

2.4.2.1 Ribs and Vertebral Column Segmentation in 3D

Precise segmentation of the vertebral column and ribs from CT images is a clinically valuable goal. As stable structures, ribs can be used to localize other organs such as
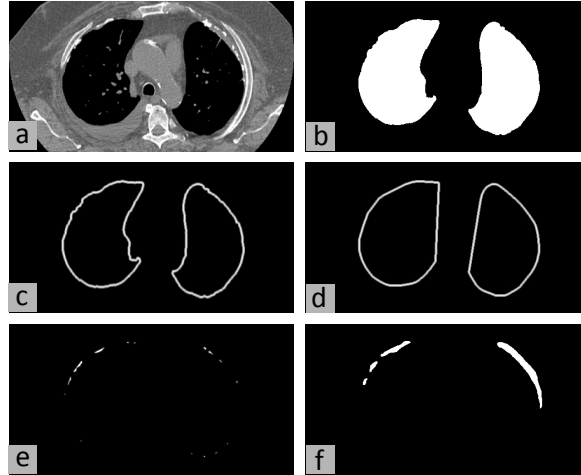
Figure 2.14: (a) Slide number 175 of patient number 5 MDCT dataset (chosen from a test dataset) (b) segmented lungs (c) lungs contours (d) convex hull of the lungs contours (e) result of subtracting lungs contours from their convex hull and (f) manually marked PPs by radiologist.

the lungs. 3D segmentation and reconstruction of a patient's vertebral column and ribs can be used in implant applications and are also beneficial for clinicians who deal with patients' chest bone abnormalities.

In most works, segmentation of the chest bony structure occurs in the initial stages and the result is mainly used as landmarks to localize other organs [64, 83]. These works generally use threshold-based methods followed by morphological operations to segment the vertebral column and/or ribs.

Recently, some methods have been proposed for extracting rib centrelines. A method based on the Random Walker algorithm and Kalman filter [113] and another using a learning based deformable template matching technique to extract rib centrelines [146] have been presented. A shape-based method for rib centreline detection to define the outline of lungs with cancer [134] and another using lung contours to determine candidate ribs derived from thresholding [148] have been proposed. A number of segmentation/reconstruction methods have also been proposed for biplanar [43] or scintigraphy [144] images.

In addition, some work that specifically focuses on vertebral column and ribs volume segmentation has been presented. A general framework including 1D ridge detection followed by construction, classification and grouping has been used for rib

segmentation [131]. Model-based methods are another approach for rib cage [73] and vertebra [74] segmentation.

2.4.2.2 Sternum Segmentation in 3D

The precisely segmented sternum is a stable reference for registration of chest images, analysis of human anatomy and localization of the costal notches (sternocostal joints) in 3D. In addition, it contributes to sternum implant surgery and pre- and post-surgical analysis related to sternum deformity correction surgery. Positioning of the costal notches positioning helps to estimate the costal cartilage centre points from CCJ to the sternum more accurately.

The aesthetic outcome of surgery to correct for Pectus excavatum (PE), the most common deformity of the chest wall, is very important in medicine. Recently, some methods have been proposed to predict the surgery outcome before the operation [116]. A model of the sternum has been presented [133] based on geometry and was used to fabricate an implant. The algorithm uses healthy sternum samples to generate clouds of points and a polygonal model. The technique to extract the sternum samples includes thresholding, region growing and editing. However, the details and accuracy of the sternum segmentation have not been provided. To extract pleural effusion in CT images, the sternum has been used for registration [71]. 3D sternum was obtained by setting a regular triangle ROI at the anterior region and extending it to volume of interest (VOI) in the z direction, yet the performance of the sternum segmentation method has not been discussed. Another method [98] uses the sternum and 3D position of costal notches to approximate the costal cartilage both before and after sternum displacement, without details of the segmentation technique and accuracy evaluation.

To sum up, limited attempts have been made on sternum segmentation to date. In related publications, sternum segmentation is a part of other segmentations and purposes.

2.4.2.3 Lung Segmentation in 3D

Accurate segmentation of the lungs in CT images has been of great interest to both clinicians and engineers. Extraction of the lungs in 2D or 3D is useful in computer aided detection (CADe) and diagnosis (CADx) and analysis of a patient's CT and anatomy. The first attempts to extract lungs from CT images started many years ago and new work continues to be done to improve both segmentation performance and speed.

According to a survey [126], most of the techniques for lung segmentation are based on specified rules. For instance, the methods proposed [27, 63, 14, 80, 84, 123, 125, 143, 149] are based on gray-level thresholding, followed by algorithms such as morphological operations, region growing, size and location restriction and component analysis. Other work [76] uses wavelet feature or is based on fuzzy connectedness segmentation [67].

In addition, other features and algorithms have been used to improve the segmentation robustness in pathological cases. Active shape model combined with snakes [82] is a statical approach. Registration with a pre-segmented reference scan [127] increases the robustness in datasets with high density pathologies.

A widely employed algorithm for lung segmentation is graph cut, which provides a high performance solution. Graph cut algorithm is described later in section 2.5.1.1. According to the graph cut theory and in order to segment an image with the graph cut algorithm, different neighbourhood sizes may be chosen to build the graph. For instance, the algorithm proposed [100] employs multi-shape graph cut with neighbour prior constraints to extract the lungs and 8 and 26 neighbours were considered for obtaining synthetic images and segmentation respectively. Graph cut algorithm combined with a statistical atlas-based shape estimation is another technique proposed [124] for lung segmentation and 6 neighbours were considered to built the graph. Graph cut with Gibbs-Markov random field (GMRF) is used [10, 9, 47] to model the spatial interaction for lung segmentation and different neighbourhood and graph sizes including 4 and 6 neighbours were considered to test and deliver the result.

2.4.3 Automatic Reconstruction and Modelling in 3D

Results of rib and costal cartilage reconstruction and diaphragm modelling in 3D contribute important information for detecting PPs and DPT and current approaches to deliver the result are discussed in sections 2.4.3.1 to 2.4.3.3

2.4.3.1 Ribs Reconstruction in 3D

Attempts at computational reconstruction of the ribs from radiology images have been mainly on biplanar images [53, 75]. Ribs are generally assumed to have a simple geometrical structure for purposes of tracing, segmenting, centre-line extraction and labelling. For example ribs are assumed to have a hollow cylindrical [81] or hollow tube [120] structure and also elliptical [73, 137] or circular [49] cross-sectional shape.

2.4.3.2 Costal Cartilage Reconstruction in 3D

Costal cartilage segmentation, reconstruction and modelling have been used frequently in analysis of chest wall deformities such as pectus excavatum [21, 145], and to predict post-surgical cosmetic appearance [98]. It has also been used [36] in quantitative evaluation of cartilage changes after Ravitch thoracoplasty to correct the deformity of pectus excavatum.

3D modelling of costal cartilages has been performed [137] to study the effects of age-related thoracic cage calcification on the respiratory system. Finite element (FE) modelling of the fourth costal cartilage was developed from CT scans of cadavers [6] and used to predict automobile collision injuries and overall structural behaviour. In addition, benefits of preoperative costal cartilage imaging over physical examination and chest radiograph have been found [72] for auricular reconstruction for microtia, a congenital deformity where the external ear is underdeveloped. Furthermore, costal cartilage extensions to the sternum were modelled in 3D via reverse modelling [133], before fabrication for sternum implant surgery when the sternum is affected by cancer.

In reconstruction techniques, the intensity feature has been used [21, 145] for

segmentation of costal cartilages. Manual costal cartilage segmentation was performed as part of recent quantitative geometric analysis of rib, costal cartilages and sternum [118] and for generating a FE model of the human thorax [121]. Considering that the liver and cartilage share an overlapping range of CT values, marker-based watershed segmentation has been proposed [61] for segmenting the costal cartilages in CT dataset.

2.4.3.3   Full Diaphragm Modelling in 3D

3D modelling of the diaphragm has been used in different ways including:

 (i) simulating diaphragm deformation during free breathing [140]

 (ii) as a reference for dividing the abdominal cavity and for localizing some internal parts when there is uncertainty due to low contrast between adjacent organs such as heart and liver [115]

(iii) as an effective landmark to localize lung tumours [78] and abdominal tumours (for example tumours caused by Neuroblastoma [114])

(iv) as a principal organ for modelling respiratory motion [89, 90, 91, 138].

Despite the value of full diaphragm modelling, diaphragm segmentation has only been performed manually [17, 103] which is a time consuming task, taking about 3 hours per dataset [139], and may be inaccurate due to human error. To date, some attempts have been made on semiautomatic [88] and automatic [18, 19, 20, 68, 147, 150] segmentation of the diaphragm dome and top surface and a few articles represent the full diaphragm in 3D. Available methods [114, 115] use the lower surfaces of the lungs to model the diaphragm as two unified quadratic surfaces and refine the result using a deformable contour model. However, modelling of the diaphragm relies only on the lower surfaces of the lungs and does not use other stable references and organs (such as the ribs). Furthermore, the refinement step for improving the result is performed on axial slices and does not use any inter-slice information [147].

2.5 Related Algorithms and Performance Evaluation

This section describes the basic algorithms, employed in segmentation and modelling. In addition, the concept of the test dataset and performance evaluation metrics are described thereafter.

2.5.1 Segmentation and Modelling Methods

Different segmentation techniques employed in this thesis are described including graph cut algorithm, region growing and active contours. In addition, smoothing spline is described, which may be used for rib and costal cartilage centre-lines interpolation.

2.5.1.1 Graph Cut Algorithm

The theory of graph cut was proposed in computer vision as early as 1989 [52]. Later, the efficiency and applicability of Markov random fields and graph cut in a wide range of computer vision problems have been shown [24, 25, 26]. Graph cut segmentation became popular in the medical imaging domain and has been used to extract different parts of the human body in various medical images including magnetic resonance imaging (MRI), HRCT, MDCT etc. Recent attempts have been made to extract kidneys [77], liver [38], lungs [100, 106], sternum [104], ribs and vertebral column [105] from medical image datasets using graph cut.

Graph cut is a min-cut/max-flow algorithm that minimizes a certain graph energy. Boykov and Kolmogorov provide several experimental comparisons [24] to prove the power of the graph cut algorithm for low-level vision problems and object segmentation. Later graph cut was developed for object extraction in higher dimensional images [23].

In graph cut algorithm, image pixels/voxels are modelled as vertices connected by weighted edges, with each vertex also connected by weighted edges to two terminals,
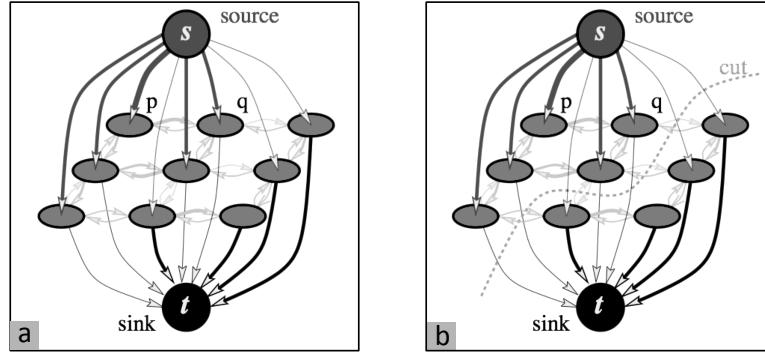
Figure 2.15: (a) Example of a directed graph G and (b) a "cut" divides nodes of G into two parts such that each terminal is in one part [24].
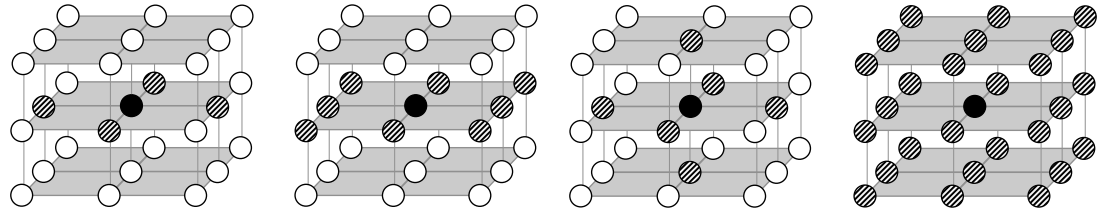
Figure 2.16: Different neighbourhood sizes. From left to right: hatched pixels are 4 (2D), 8 (2D), 6 (3D) and 26 (3D) neighbours around the black pixel.

namely source and sink. As shown in Figure 2.15a, vertices, terminals and edges make up a directed weighted graph $G = \langle V, E \rangle$. After building the graph, a subset of edges called an $s - t$ cut can be employed to separate the source from sink (see Figure 2.15b). As shown in Figure 2.16, a graph may be built in 2D and 3D with different neighbourhood sizes.

In mathematical terms, let P denote a set of pixels/voxels, N a set of all neighbouring pairs $\{p, q\}$ in P, and components of the vector $A = (A_1, ..., A_p, ..., A_{|P|})$ refer to object/background labelling of pixels p in P. Optimal image segmentation is achieved by optimal pixels/voxels labelling via minimizing the following energy function [23]:

$$E(A) = \lambda . \sum_{p \in P} R_p(A_p) + \sum_{\{p,q\} \in N} B_{p,q} \cdot \delta_{A_p \neq A_q} \qquad (2.1)$$

The first and second part of this energy function may be interpreted as a regional and boundary term respectively. The regional term penalizes mislabeling of each pixel/voxel based on its dissimilarity with terminals, and $B_{p,q}$ penalizes the

discontinuity between p and q. If I_p represents the pixel intensity p, the two terms of Equation (2.1) may be defined as [23]:

$$R_P(A_p) = -\ln \Pr(I_p \mid A_p) \tag{2.2}$$

and

$$B_{p,q} = \exp(-\frac{(I_p - I_q)^2}{2\sigma^2}) \cdot \frac{1}{dist(p,q)} \tag{2.3}$$

If $A_p \neq A_q$, then the coefficient $\delta_{A_p \neq A_q}$ is equal to 1, otherwise to 0, and λ reflects the relative emphasis on regional versus boundary terms. More details of the energy function and graph cut algorithm may be found [24].

2.5.1.2 Region Growing

In image processing, a region is described as points with at least one common property. Region growing is a simple region-based image segmentation method that starts from a seed point(s) and determines whether the neighbouring pixels belong to the region. If I denotes an image and P is a logical predictor, then region growing is defined as follows [152]:

$$\bigcup_{i=1}^{N} I_i = I \tag{2.4}$$

$$I_i, \quad i = 1, 2, ..., N \tag{2.5}$$

$$P(I_i) = TRUE \tag{2.6}$$

for $i = 1, 2, ..., N$

$$P(I_i \cup I_j) = FALSE \tag{2.7}$$

for $i \neq j$, where I_i and I_j are adjacent.

There are three approaches for region growing [152] including regional neighbour search, multi-regional heuristics and functional approximation and merging. More details may be found [57, 92, 152].

2.5.1.3   Active Contours Model

Originally called snakes [69], active contours is an energy-minimising spline that delineates objects in a given image I_0. Starting from a predefined contour, the spline curve is guided towards image features such as edges. In the classical active contours model, an edge-detector stops the evolving curve based on the gradient of I_0. If $V(s) = (X(s), Y(s))$ represents the position of a snake, then the energy function may be defined as [69]:

$$E_{snk} = \int_0^1 (w_{int} E_{int}(V(s)) + w_{img} E_{img}(V(s)) + w_{con} E_{con}(V(s)))ds \qquad (2.8)$$

where each energy component is controlled by the corresponding weighting factor w. E_{int} represents the snake internal energy and controls the smoothness of the spline [69]. The other two energies are related to the external energy i.e. E_{img} is the image force which pushes the spline to the image salient features and E_{con} represents the external forces determined by the user interface.

The internal energy is defined as a combination of a first and second order spline, forcing the active contour to act like a membrane and spline respectively and their effect is controlled by weights $\alpha(s)$ and $\beta(s)$ as follows:

$$E_{int} = (\alpha(s) |V_s(s)|^2 + \beta(s) |V_{ss}(s)|^2)/2 \qquad (2.9)$$

Features of the image, including lines and edges, affect the snake behaviour via E_{img} and in mathematical terms is defined as:

$$E_{img} = w_{line} E_{line} + w_{edge} E_{edge} \qquad (2.10)$$

E_{line} is simply defined so that it is attracted to the lines based on their intensity i.e. $E_{line} = I(x, y)$. By defining $E_{edge} = - |\nabla I(x, y)|^2$, the snake is attracted to large

gradients in the image. A termination function term may be added to E_{img} as:

$$E_{term} = \partial\theta/\partial n_\perp = (\partial^2 C/\partial^2 n_\perp)/(\partial C/\partial n) \tag{2.11}$$

$$= (C_{yy}C_x^2 - 2C_{xy}C_xC_y + C_{xx}C_y^2)/(C_x^2 + C_y^2)^{3/2}$$

where $C(x,y) = G_\sigma(x,y) * I(x,y)$ is a smoothed version of the image with gradient angle $\theta = tan^{-1}(C_y/C_x)$ and $n = (cos\theta, sin\theta)$ and $n_\perp = (-sin\theta, cos\theta)$, the unit vectors. E_{term} controls E_{img} by the weighting factor w_{term}. More details about the classic active contours may be found [28, 29, 69].

2.5.1.4 Smoothing Spline

If a sequence of observations (x_i, Y_i); $x_1 < x_2 < \cdots < x_n$ is modeled by the relation $Y_i = \mu(x_i)$, the smoothing spline $\hat{\mu}$ is an estimation of function μ that minimizes:

$$\sum_{i=1}^{n}(Y_i - \hat{\mu}(x_i))^2 + \lambda \int_{x_1}^{x_n} \hat{\mu}''(x)^2 dx \tag{2.12}$$

where the smoothness is controlled by λ [59].

2.5.2 Performance Evaluation

The protocol for performance evaluation employed in this thesis includes the following steps:

(i) run each proposed algorithm on a test dataset

(ii) compare the results against the corresponding ground truth to evaluate the performance, using different criteria.

The gold standard for comparing the result was marked and confirmed by an experienced radiologist. All processing and evaluations were performed on a standard computer with 2.53 GHz CPU speed and 4 GB RAM. The following subsections

Table 2.1: Technical data of MDCT studies, used for testing and evaluating proposed algorithms.

Image	
Slice thickness	1 mm
Slice increment	1mm
In plane resolution	0.625 mm x 0.625 mm
Protocol name	Chest non-contrast
Image size	512 x 512
Image Type	Original/Primary/Axial
Scanner	
Manufacture	Toshiba
Model Name	Aquilion PRIME

provide technical description of the datasets employed and the metrics, used for performance evaluation.

2.5.2.1 Test Datasets

All algorithms were tested on complete lung MDCT datasets. After ethics approval and over a five year period, anonymized MDCT images were provided by the *Radiology Department of Prince of Wales Hospital, Sydney, Australia*. Since the datasets were anonymized and the radiologist did not provide information on whether the datasets belong to the same patient/study, the datasets could not be tracked back. Technical data about the MDCT studies is summarized in Table 2.1.

2.5.2.2 Performance Evaluation Metrics

All evaluation metrics were chosen carefully based on state-of-the-art metrics of similar algorithms in the literature. More specifically, a superset of chosen criteria was used to test the proposed techniques. Variance was not chosen as an appropriate metric because (i) it has not been used to evaluate similar algorithms in published articles and (ii) evaluations were performed on a limited number of datasets, wherein the full range of variations may not have been covered.

Different criteria, used to measure the accuracy of the proposed algorithms,

include: Dice Similarity Coefficient (DSC), *Sensitivity*, *Specificity*, False Negative Ratio (FNR), False Positive Ratio (FPR), *Accuracy*, *Precision*, mean distance (d_{mean}), root mean square distance (d_{rms}), Euclidean distance, Hausdorff distance and Mean Distance to the Closest Point ($MDCP$). All metrics are divided into three groups: similarity, classification and distance metrics.

2.5.2.2.1 Similarity Metrics

One common metric for comparing the similarity of two samples is DSC [41, 130]. This metric is a simple and useful statistical validation metric and has been used frequently in detection problems in medical image processing [8, 15, 16, 94, 151]. DSC between the result of an automatic algorithm (A) and the corresponding ground truth (G) ranges between 0 to 1 and is calculated as follows:

$$DSC = (2 \times |G \cap A|) / (|G| + |A|) \tag{2.13}$$

2.5.2.2.2 Classification Metrics

Appropriate error metrics for detecting problems are *Sensitivity* and *Specificity* [129] and they are known in statistics as classification functions. *Sensitivity* measures how frequently the metric reports that an abnormality exists where it actually exists. In detection problems in image processing, *Sensitivity* is about a pixel and whether it is a member of ground truth or not. *Specificity* refers to how frequently the method correctly reports normal when no abnormality exists. *Sensitivity* and *Specificity* are computed as follows:

$$Sensitivity = TP/(TP + FN) \times 100 \tag{2.14}$$

$$Specificity = TN/(TN + FP) \times 100 \tag{2.15}$$

where based on the algorithm decision, TP (true positive) means it is correctly decided that an abnormality exists, FP (false positive) means it is wrongly decided

that an abnormality exists, TN (true negative) means it is correctly decided that an abnormality does not exist and FN (false negative) means it is wrongly decided that an abnormality does not exist. Two other metrics i.e. *FNR* and *FPR* are calculated as follows:

$$FNR = 1 - Sensitivity \tag{2.16}$$

$$FPR = 1 - Specificity \tag{2.17}$$

Accuracy and *Precision* are defined in terms of systematic and random errors. *Accuracy* is used as a statistical measure of how well a binary segmentation correctly detects or excludes pixels of an image. *Precision* or positive predictive value is defined as the proportion of the true positives against all the positive results (both true positives and false positives). *Accuracy* and *Precision* are computed as follows:

$$Accuracy = (TP + TN)/(TP + FP + FN + TN) \times 100 \tag{2.18}$$

$$Precision = TP/(TP + FP) \times 100 \tag{2.19}$$

2.5.2.2.3 Distance Metrics

To compute the distance between A and G, if pG and pA are the number of pixels defining the G contour and A contour respectively, then:

$$d_{mean} = (\sum_{q=1}^{pG} d(q, G) + \sum_{q=1}^{pA} d(q, A))/(pG + pA) \tag{2.20}$$

$$d_{rms} = \sqrt{(\sum_{q=1}^{pG} d(q, G)^2 + \sum_{q=1}^{pA} d(q, A)^2)/(pG + pA)} \tag{2.21}$$

where:

$$d(q, G) = min_r\{\sqrt{(x_q^A - x_r^G)^2 + (y_q^A - y_r^G)^2}\} \tag{2.22}$$

$$d(q, A) = min_r\{\sqrt{(x_r^A - x_q^G)^2 + (y_r^A - y_q^G)^2}\} \tag{2.23}$$

d_{mean} and d_{rms} measure the mean and average squared distance between A and

G respectively.

Another popular metric for comparing segmentation results with the ground truth is the Hausdorff distance. This metric measures the maximum distance of a set to the nearest point in the other set [65, 66] i.e. how far two subsets of a metric space are from each other. In mathematical terms, if $p = p_1, p_2, ..., p_M$ and $q = q_1, q_2, ..., q_N$ are points in sets P and Q respectively, directed Hausdorff distance from P to Q is a max-min function defined as:

$$h(P,Q) = max[min(dist(p,q))], \quad p \in P, \ q \in Q \tag{2.24}$$

and a more general definition for Hausdorff distance is:

$$H(P,Q) = max\left\{h(P,Q), h(Q,P)\right\} \tag{2.25}$$

which measures dissimilarity and mismatch between two sets.

As a more general measure of distance compared to the Hausdorff distance, $MDCP$ measures the closeness of two sets. Using the above notation, $MDCP$ is determined as:

$$MDCP(P,Q) = (1/M) \times \sum_{i=1}^{M} DCP(p_i, Q) \tag{2.26}$$

where

$$DCP(p_i, Q) = min \left\| p_i - q_j \right\|, \ j = 1, 2, ..., N \tag{2.27}$$

and $\|.\|$ represents distance norm.

2.6   Summary

Two commonest types of ARPD i.e. PPs and DPT, their epidemiology, pathological features, imaging techniques and current approaches in medical science for their diagnosis were discussed in this chapter. Anatomical terms and background knowledge were defined. State of the art techniques, that are required for automatic PPs and DPT detection in MDCT datasets have been reviewed as well as gaps in the

literature and the challenges involved. In addition, key evaluation criteria and technical descriptions of the basic algorithms used for PPs and DPT detection have been covered in this chapter.

The next chapter provides details of proposed segmentation techniques to extract the lungs, ribs, vertebral column and sternum from MDCT datasets. Also the experiments to evaluate the performance and accuracy of the techniques are presented and their results are discussed.

Chapter 3

Automatic Segmentation and Extraction in 3D[1]

Image segmentation refers to the partitioning of a digital image into sets of pixels by assigning the same label to pixels that share certain characteristics. In other words, a segmented image consists of labeled pixels (super-pixels) that are useful for further analysis and have more meaningful representation. The main goal of image segmentation is to identify objects or other relevant information in digital images. Image segmentation has various applications in medical image analysis including diagnosis of diseases, tumours and other pathologies localization and study of anatomical structure [111].

Segmentation of some organs including the lungs, ribs, vertebral column and sternum are necessary steps for PPs and DPT extraction in 3D. The result of the organs segmentation contributes important information to subsequent steps, including ribs and costal cartilage reconstruction, diaphragm modelling and pleural costal surface estimation in 3D. This chapter presents novel methods for 3D segmentation of the lungs, ribs, vertebral column and sternum as well as costal notches localization in 3D.

The motivation and goals to be achieved are explained in section 3.1. Frameworks of the proposed algorithms and technical details of the steps are provided in section

---

[1]Portions of the work have been published [104, 105, 106]

3.2. All techniques are tested and evaluated by several experiments and the details are presented in section 3.3. The results of evaluations are discussed therafter in section 3.4.

3.1 Motivation and Goals

The efficiency of graph cut algorithm in image segmentation has been established [26, 23], specially in the medicall imaging domain [24]. However, as far as is known, it has not been used for segmenting the human vertebral column and ribs in CT images. A novel graph cut based algorithm is proposed for extracting the ribs and vertebral column in lung MDCT images. The fully automatic approach starts with an initialization step, and is followed by an isolation technique to refine the segmentation results as well as remove mis-segmented bones. The proposed technique was tested to evaluate the performance and accuracy.

A fully automatic algorithm for 3D lung extraction from lung MDCT datasets is presented. According to the graph cut theory (see section 2.5.1.1), different neighbourhood sizes may be chosen to build the graph. Increasing graph size increases the segmentation time dramatically, while not necessarily improving the segmentation performance. Considering the fact that beside accuracy, fast segmentation is always desired, lung segmentation with different graph sizes was tested on a large dataset (50 complete MDCT datasets). The algorithm was employed to investigate the effect of change in neighbourhood size on the performance and speed.

A fully automatic algorithm that specifically focuses on sternum segmentation is presented. The proposed algorithm accurately isolates the human sternum in MDCT dataset and localizes the costal notches in 3D. More precisely, the main contributions of the algorithm are:

(i) the perimeter of the sternum front-view, as illustrated in Gray's anatomy [51] (see Figure 3.1), is used to refine the sternum segmentation result by removing the attached calcified costal cartilages

(ii) all costal notches are localized in 3D in Cartesian coordinate system by using
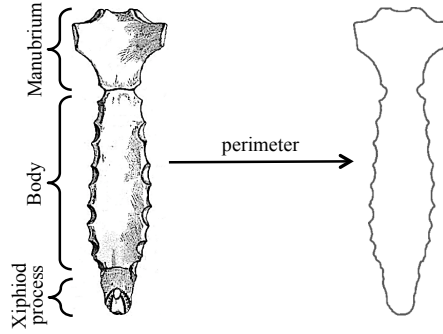
Figure 3.1: Sternum mask is assumed as perimeter of the the sternum front-view, illustrated in Gray's anatomy [51].

pre-knowledge of costal notch locations on the 2D sternum mask.

3.2 Segmentation Framework

To perform segmentation and extract organs from an MDCT image, several steps should be taken. An initialisation step provides an intensity image with no extraneous pixels around the patient's body. The next step provides preliminary results including chest hard structure (bone) and soft tissue (respiratory organs) in 3D. Lungs, ribs, vertebral column and sternum are segmented and isolated from preliminary results by fully automatic algorithms. Also, all costal notches are localized in 3D from the segmented sternum. Details of the different steps are explained in sections 3.2.1 to 3.2.3.

3.2.1 Initialisation

In each dataset, after converting MDCT slides to conventional intensity images, extraneous pixels around the patient's body are removed as they do not carry useful data for lungs and bone segmentation. These include air, patient's clothes and other artefacts, which are removed from each slice using thresholding, followed by morphological operations. Pseudo code for removing artefacts from the original dataset is provided in Appendix A. An example of a patient's original and trimmed slices are presented in Figure 3.2.
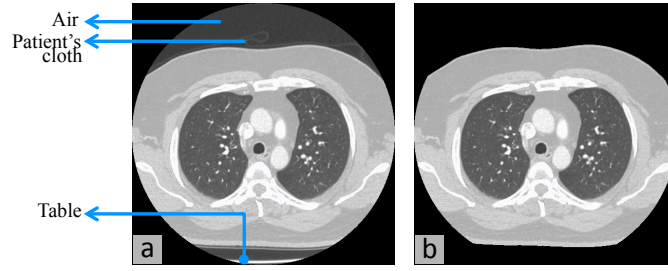
Figure 3.2: (a) Patient number 8, slide number 122 and (b) patient's body without extraneous pixels.

3.2.2 Preliminary Segmentation in 3D

The main algorithm for 3D extraction of the chest soft tissue and hard structure is the graph cut algorithm, explained earlier in section 2.5.1.1. Segmenting of respiratory organs and chest bone from the original datasets are considered as preliminary results and are explained in sections 3.2.2.1 and 3.2.2.2.

3.2.2.1 Respiratory Organ Segmentation

To segment the respiratory organ i.e. the darkest pixels in a patient's body dataset, the graph cut algorithm is used. The Gaussian function is chosen as the regional term of the graph cut energy function (Equation (2.1)) for both object and background, and the expectation maximization (EM) algorithm is employed to estimate their parameter values. From each dataset, three consecutive slices in the middle of the dataset are selected and for each slice, the EM algorithm is used to estimate its pixel grey level distribution as a mixture of five Gaussian distributions.

To extract the soft tissue, it is assumed that the Gaussian distributions, from dark to bright, are related to (i) extraneous pixels (ii) respiratory organ tissue (iii) chest muscle and fat (darker part) (iv) chest muscle and fat (brighter part) and (v) bone structure. To minimize error, the Gaussian parameters are computed as the means of the three chosen slices. All these parameter values are passed to the graph cut algorithm to extract the respiratory organ in 3D.

3.2.2.2   Chest Bone Segmentation

To segment the chest bone from MDCT datasets, the respiratory organs are removed, using the technique in section 3.2.2.1. The reason for removing the lungs is that they do not carry helpful data for bony structure segmentation.

Similar to respiratory organ segmentation, to segment the chest bone using graph cut algorithm, the Gaussian function is chosen as the regional term of the graph cut energy function (Equation (2.1)), for both object and background and EM algorithm to estimate their parameter values. For each dataset, five consecutive slices are chosen in the middle of the dataset and for each slice, EM algorithm is used to estimate its pixel grey level distribution as a mixture of three Gaussian distributions. The first Gaussian distribution is assumed to be related to dark areas i.e. extracted respiratory organs, air etc. The second and the third Gaussian distributions are assigned to the background (patient's other soft tissue i.e. muscles and fat) and the object (bone structure) respectively. To minimize error, Gaussian parameters are chosen as the means of the five chosen slices. All these parameter values are passed to the graph cut algorithm for segmenting the bone structure in 3D.

3.2.3   Organs Extraction in 3D

Several steps are taken to refine the preliminary outcome to extract the lungs, ribs, vertebral column and the sternum in 3D. The algorithms for lung segmentation and ribs and vertebral column isolation in 3D are explained in sections 3.2.3.1 and 3.2.3.2 respectively. After extracting the sternum from the already segmented chest bone, the result may still include attached calcified costal cartilages. Novel algorithms for segmenting the sternum, by removing existing attached calcified costal cartilage as well as localizing the costal notches in 3D, are provided in section 3.2.3.3.

3.2.3.1   Lung Segmentation

As mentioned in section 3.2.2.1, the graph cut algorithm is used for extracting the respiratory organs from the trimmed intensity images (original intensity images
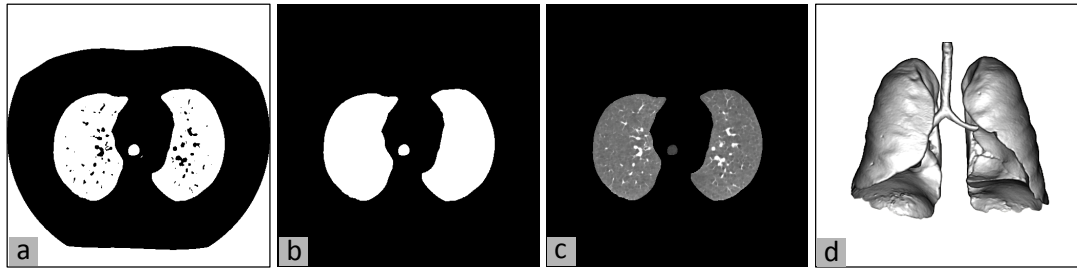
Figure 3.3: (a) Result of applying graph cut algorithm on Figure 3.2b (b) identified respiratory organs (c) illustration of lungs extraction as an intensity image and (d) segmented lungs, trachea and bronchi of patient number 8 in 3D.

without extraneous pixels around the body). The graph cut algorithm returns a binary image i.e. pixels belonging to source or background. The result of segmenting the lungs in Figure 3.2b with graph cut is shown in Figure 3.3a. It is clear that dark areas around the body and within lungs are both assigned to the source while other soft tissues with higher intensity values are segmented as background. To identify the lungs in the 3D binary image, first white pixels around the body are removed. Next the biggest component in the 3D binary image is chosen as the lungs, trachea and bronchi. In the final stage and as shown in Figure 3.3b, dark spots in the lungs (Figure 3.3a) are filled to draw the lungs contour. Pseudo code to identify the lungs in the graph cut algorithm result (binary image) is provided in Appendix B. An example of segmented lungs, trachea and bronchi in 3D is shown in Figure 3.3d.

3.2.3.2 Ribs and Vertebral Column Segmentation

As mentioned in section 3.2.2.2, the graph cut algorithm is used for segmenting the chest bone from MDCT images and the result are binary slices. To identify the ribs and vertebral column in the extracted chest bone, a 3D binary image is created for each dataset and the biggest component is labeled as the spinal column and ribs. Next, each slice is improved by applying morphological operations including the closing operation and filling holes.

Occasionally some other bony structures such as the sternum, clavicle and scapula get included in the final result. This could be due to cartilage calcification associated with ageing, or inadequate resolution in CT images. Examples of segmentation without and with mis-segmented parts are shown in Figures 3.4b and 3.4f respectively.
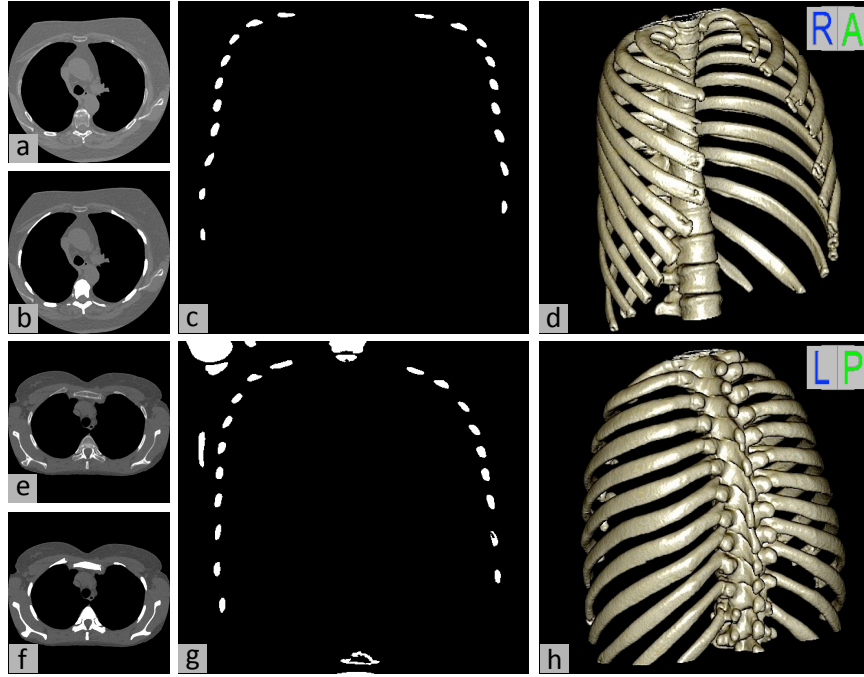
Figure 3.4: (a) and (e) examples of slices without extraneous pixels around the body (images belong to different patients), (b) and (f) result of bone segmentation by employing graph cut algorithm with 2D (8 neighbours) and 3D (26 neighbours) graph, (c) and (g) bone cross-sections at mid-coronal plane, (d) and (h) 3D view of segmented vertebral column and ribs.

The mis-segmented parts can dramatically decrease the accuracy of localization and landmarking based on vertebral column and ribs, and should be removed. To do this, the vertebral column and the ribs are isolated in 3D with two novel algorithms, explained in the following two sub-sections.

3.2.3.2.1 Sternum Removal

To remove the sternum, all N cross-sections of bones in mid-coronal plane are found and A, the mean area of N objects, is calculated. The N objects are the cross-sections of ribs and occasionally the vertebral column, clavicle(s) and/or scapula(s) (see Figures 3.4c and 3.4g for examples). The N objects are traced separately in the coronal direction toward the sternum with a region growing technique. Each tracing procedure is stopped when the area of the traced object is larger than twice A.

3.2.3.2.2   Scapula Removal

Sometimes the scapula is included in the final segmentation results, due to attachment to the clavicle, which in turn is attached to the sternum. In such a situation, if the sternum is removed, the scapula will also be removed automatically. However, sometimes in the segmentation results, the scapula(s) is still attached to the rib(s) due to inadequate CT resolution or high pairwise potential cost in graph cut energy function (Equation (2.1)).

The technique to localize the scapula(s) attachment point(s) in 3D is the same as for sternum removal with two considerations: (i) the tracing algorithm starts with existing objects at 1/5 of the top first axial plane at left and right and (ii) the direction of the tracing is downward in the axial direction. Pseudo code for removing the scapula and the clavicle from segmented chest bone in 3D is provided in Appendix C.

After localizing all attachment points and cutting the 3D binary image at such points, the biggest 3D component is the isolated vertebral column and ribs. (see Figures 3.4d and 3.4h for two examples in 3D).

3.2.3.3   Sternum Segmentation

Human sternum has a bony structure and is included in the 3D segmented chest bone (as explained in section 3.2.2.2). The segmented chest bone may include existing calcified xiphoid process as well as calcified costal cartilage, attached to the sternum. The algorithm and the detailed steps for sternum isolation are summarized in Figure 3.5, with an example for each step.

The algorithm for sternum isolation is almost similar to the technique presented in section 3.2.3.2.1 for sternum removal with minor differences, and is summarized as follows:

  (i) ignore the half-back of the segmented bone in 3D (see Figure 3.5b)

  (ii) find N number of bone cross-sections in mid-coronal plane (see Figure 3.5c)
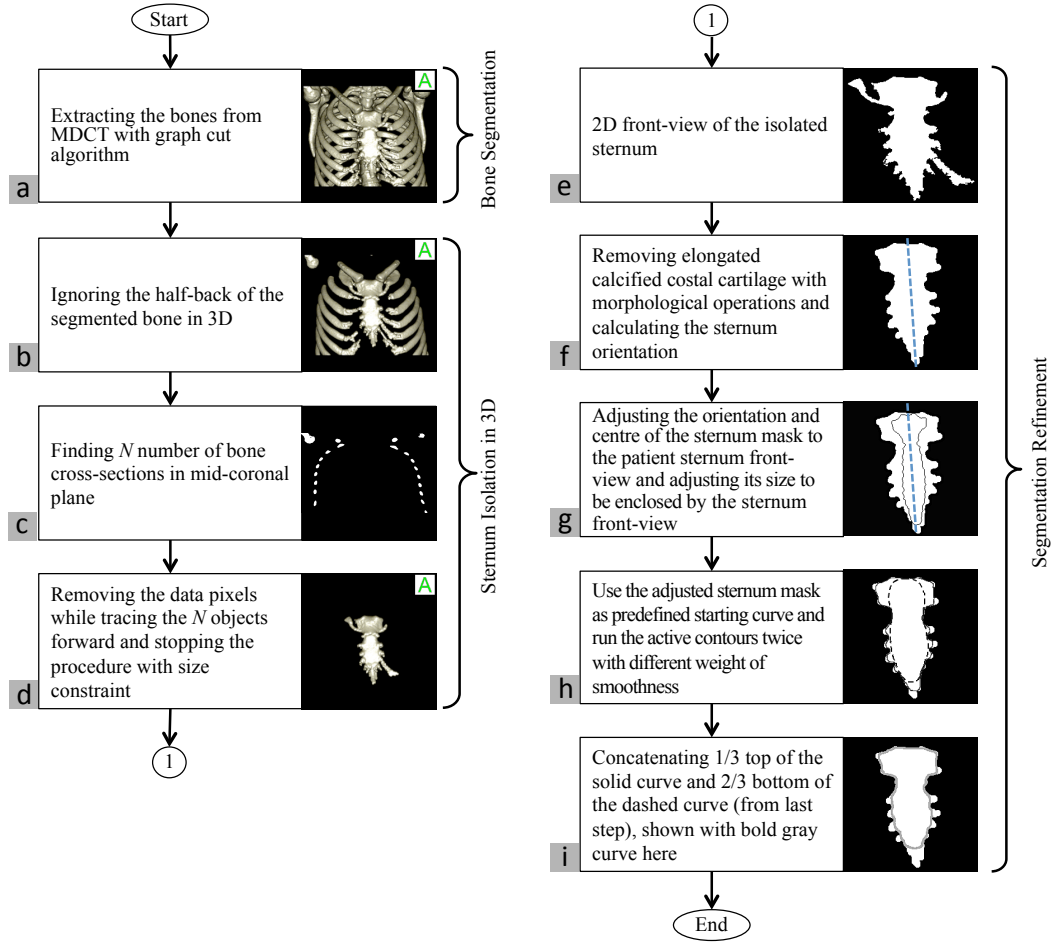
Figure 3.5: Flowchart of 3D sternum segmentation, tested on patient number 7. (Images shown in (e) to (i) are magnified front-view of the 3D sternum illustrated in (d)).

(iii) remove while tracing, all the N objects forward (tracing is based on region growing technique)

(iv) apply size constraint to stop the tracing procedure for each N objects.

The result of the 4-step procedure is the isolated sternum in 3D which may include calcified costal cartilage (see Figure 3.5d). A novel method based on active contours model is employed to remove the undesired parts from the sternum segmentation result. The proposed algorithm to remove any attached calcified costal cartilage from the sternum is summarized as follows:

(i) Add binarized coronal planes together to get 2D front-view of the isolated sternum (Figure 3.5e).
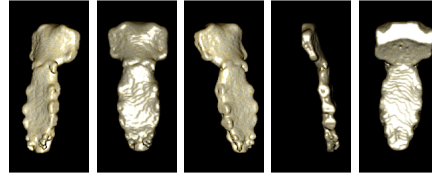
Figure 3.6: Different views of the patient number 7 segmented sternum.

(ii) Calculate θ, the orientation of the sternum front-view. Since the elongated calcified costal cartilages attached to the sternum may change the sternum orientation significantly, they are removed by applying morphological operations e.g. image erosion (Figure 3.5f).

(iii) Adjust the orientation of the sternum mask (as shown in Figure 3.5g) to θ. Also, move its centre to the centre of the sternum front-view

(iv) Adjust the sternum mask size to be enclosed by the border of the sternum front-view (Figure 3.5g).

(v) Set the sternum mask as a predefined starting curve for 2D active contours. Run the active contours algorithm twice. First, run it with low weight of smoothness to define the manubrium (the sternum upper part) border. The weight of the smoothing term is chosen so that the starting curve moves toward the manubrium details well enough. In that case, the moving curve enters the calcified costal cartilages at the costal notch positions (Figure 3.5h, solid curve). Second, run the active contours with higher weight of smoothing term to define the border of the sternum body more accurately (Figure 3.5h, dashed curve). The final result of segmentation refinement is the concatenation of one-third top of the first active contour result and bottom two-third of the second active contour result (Figure 3.5i).

(vi) Apply the result of the last step to all coronal planes of the isolated sternum and remove pixels outside it in sagittal and axial directions.

Different views of the final sternum segmentation, tested and illustrated in the flowchart, are shown in Figure 3.6. More examples, showing removal of attached calcified costal cartilage from the isolated sternums, are in Figure 3.7.
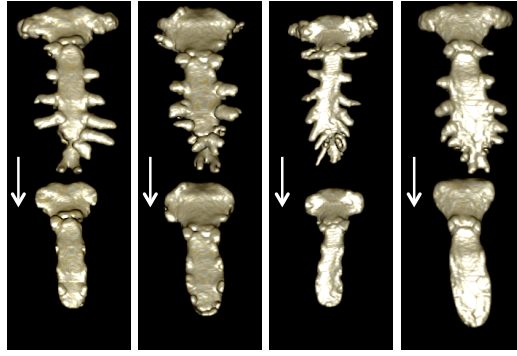
Figure 3.7: Examples of isolated sternum from four studies (top images of each pair) and sternum with removed attached calcified costal cartilage (bottom images of each pair).
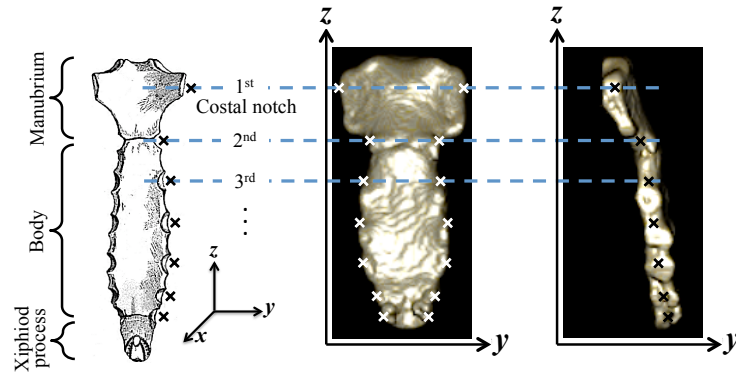
Figure 3.8: Manually marked costal notches on the sternum mask is used to localize them in z direction in real studies, which ,in turn, determine their locations in x and y directions.

3.2.3.3.1 Costal Notches Localization in 3D

The sternum mask (as shown in Figure 3.1) and seven manually marked costal notches in the z direction (see Figure 3.8) are used to determine the position of fourteen costal notches in 3D.

Assuming the x, y and z directions in Figure 3.8, the ratio of mask height to marked costal notches is used to determine the location of costal notches in the z direction on final sternum segmentation front-view. The costal notches are determined in y direction as the leftmost and rightmost pixels of the sternum front-view. Also, the costal notches are localized in x direction as the middle pixel of side-view, found at determined z directions.

3.3   Performance Evaluation

To measure the performance and accuracy of the algorithms, they were tested separately. Each algorithm was run on a set of MDCT datasets and the results were evaluated using different criteria. The following subsections provide details about the datasets used, experiments and evaluations.

3.3.1   Material

The proposed algorithms for lung, ribs, vertebral column and sternum segmentation in 3D were tested on a large number of MDCT datasets. All datasets share the same technical description, provided in section 2.5.2.1 and Table 2.1. Datasets used for evaluating the different segmentation algorithms were not identical, however they mostly overlapped. The reasons for using slightly different datasets for different algorithms are:

(i) MDCT images were provided and obtained at different times

(ii) all datasets did not necessarily contain the organ being segmented. For instance, some datasets used for evaluating the lung segmentation algorithm were not used to test the rib and vertebral column segmentation, as the complete rib cage was not covered in the MDCT images.

Demographic data of MDCT datasets, used for lung, ribs, vertebral column and sternum segmentation are summarised in Table 3.1.

3.3.2   Experiments and Results

Each presented technique for lung, ribs, vertebral column and sternum segmentation as well as costal notches localization was tested to measure its accuracy and performance. The results of each experiment were compared with corresponding ground truth using different criteria. Selected images for evaluation were marked and corrected by an experienced radiologist [1] to obtain reference mask. The following

---

[1]Medical Imaging Department, Prince of Wales Hospital, Sydney, NSW, Australia.

Table 3.1: Demographic data of MDCT studies, used for testing and evaluating lung, ribs, vertebral column and sternum segmentation techniques.

Lung Segmentation	
MDCT Dataset	
Number of studies	50
Number of slices (per dataset)	411 (on average)
Patient	
Sex	
Male	2%
Female	8%
Unidentified	90%
Age	
Mean	54.7
Range	14 - 87
Ribs and Vertebral Column Segmentation	
MDCT Dataset	
Number of studies	18
Number of slices (per dataset)	346 (on average)
Patient	
Sex	
Male	30%
Female	40%
Unidentified	30%
Age	
Mean	71.5
Range	41 - 82
Sternum Segmentation	
MDCT Dataset	
Number of studies	16
Number of slices (per dataset)	380 (on average)
Patient	
Sex	
Male	19%
Female	37%
Unidentified	44%
Age	
Mean	65.5
Range	58 - 81

Table 3.2: Evaluation of the lungs extraction in 50 MDCT datasets using different graph sizes.

Performance Metric → Graph Dimension, Neighbourhood Size ↓	DSC (%)	$Sensitivity$ (%)	$Specificity$ (%)	FNR (%)	FPR (%)	d_{mean} (%)	d_{rms} (%)
2D, 4 n	95.00	88.39	99.99	11.61	0.01	0.32	0.56
2D, 8 n	95.00	88.39	99.99	11.61	0.01	0.32	0.56
3D, 6 n	95.00	88.41	99.99	11.59	0.01	0.32	0.56
3D, 26 n	95.00	88.46	99.99	11.54	0.01	0.32	0.55

sub-sections provide details of the evaluations.

3.3.2.1 Experiments on Lung Segmentation Algorithm

The lung segmentation algorithm was run on 2D and 3D neighbourhood graphs, with 4 and 8 neighbours for 2D graphs, and 6 and 26 neighbours for 3D graphs. With λ equal to 1 in the graph cut energy function (Equation (2.1)), the question "How do graph dimension and neighbourhood size affect the segmentation performance and running time?" was investigated.

For evaluating the lung segmentation algorithm, results were compared against the ground truth. Since manual marking and segmentation of nearly 20,500 slices is practically impossible, 5 slices in each dataset were chosen for evaluation. These slices were chosen at the 1/6, 2/6, ... and 5/6 points of the total slices in each dataset individually. In the chosen slices (250 in total), lung tissue was initialized using thresholding, and the results were marked and corrected manually. Extracted parts were approved by the radiologist as reference lung masks. Trachea and bronchi were included in the landmarks.

The segmentation algorithm with different graph sizes was evaluated with seven metrics and the result are summarized in Table 3.2. The running times for segmenting a 411-slice dataset, using 4 (2D), 8 (2D), 6 (3D) and 26 (3D) neighbours are illustrated in Figure 3.9.
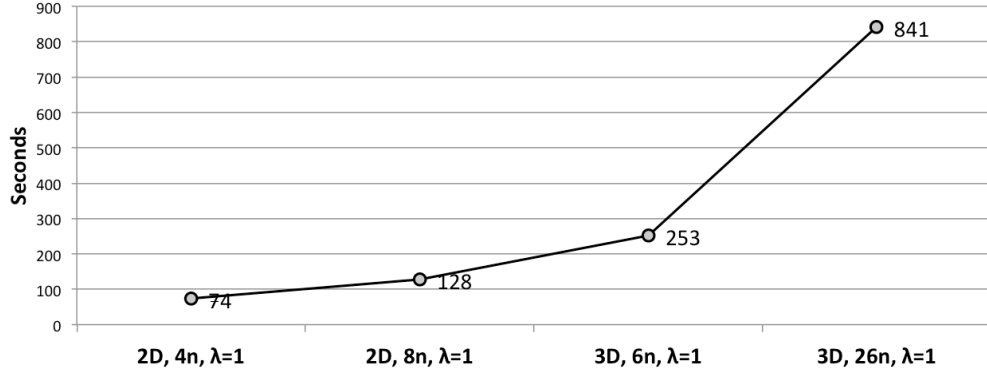
Figure 3.9: Running time for segmenting lungs from a 411-slice MDCT dataset with different graph sizes.

As presented in Table 3.2, performance is almost the same for the different graph sizes, and any one graph size hardly provides any improvement over other graph sizes. On the other hand, segmentation time increases dramatically when the size of neighbourhood is increased (see Figure 3.9). Clearly, for lung segmentation based on graph cut algorithm, the smallest graph size is as good as other larger graph sizes. More specifically, the 4 neighbourhood is to be preferred to 8, 6 and 26 neighbourhood for lung extraction from MDCT dataset.

3.3.2.2   Experiments on Ribs and Vertebral Column Segmentation Algorithm

To evaluate the accuracy and performance of the ribs and vertebral column segmentation technique, the proposed algorithm was tested by employing different graphs with different sizes. The algorithm was run on 2D graphs with 4 and 8 neighbours and 3D graphs with 6 and 26 neighbours. λ in graph cut energy function (Equation (2.1)) was set to 1 to investigate the effect of graph dimension and size on the segmentation performance. Next, the graph providing the best result on performance and time complexity was chosen to investigate the performance with different λ values.

For evaluating the ribs and vertebral column segmentation algorithm, results were compared against the ground truth. Since manual marking and segmentation of nearly 6,300 slices is practically impossible, 5 slices in each dataset were chosen for evaluation. These slices were chosen from the top 1/6, 2/6, ... and 5/6 of the total number of slices in each dataset individually. In the chosen slices (90 in total),

Table 3.3: Evaluation of the ribs and vertebral column extraction in 18 MDCT datasets using thresholding and graph cut algorithm with different graph sizes.

Performance Metric → Algorithm (and Graph Size) ↓	DSC (%)	$Sensitivity$ (%)	$Specificity$ (%)	FNR (%)	FPR (%)	d_{mean} (%)	d_{rms} (%)
GC, 2D, 4 n	**92.46**	**87.78**	**99.91**	**12.22**	**0.09**	**1.83**	5.69
GC, 2D, 8 n	92.41	87.70	**99.91**	12.30	**0.09**	**1.83**	**5.68**
GC, 3D, 6 n	92.24	85.03	99.78	14.97	0.22	3.45	9.79
GC, 3D, 26 n	91.82	86.74	**99.91**	13.26	**0.09**	**1.83**	5.90
Thresholding	83.16	80.71	99.71	19.29	0.29	5.97	17.0

the bony structure of each slice was initialized using graph cut at a default setting, and the results were marked and corrected by the radiologist to obtain reference vertebral column and rib masks.

Performance of the proposed algorithm and comparison of the result to the reference masks were evaluated using different criteria. A summary of the evaluations is listed in Table 3.3.

The results of the proposed segmentation algorithm were analyzed as follows:

(i) Based on evaluations, graph cut segmentation with the lowest number of neighbours (2D graph with 4 neighbours) has highest/near highest performance compared to other graphs with higher dimension and higher number of neighbours. Also evaluation shows that the proposed algorithm outperforms the threshold method, the most commonly used method for vertebral column and ribs segmentation.

(ii) The result of the proposed algorithm was studied numerically to evaluate the effect of changing λ in graph cut energy function (equation(2.1)) on the performance of ribs and vertebral column segmentation. The study was performed on the 2D (4 neighbours) graph. The behaviour of Dice similarity coefficient (DSC) for a wide range of λ value is shown in Figure 3.10. Middling size is recommended for parameter value λ to segment the ribs and vertebral
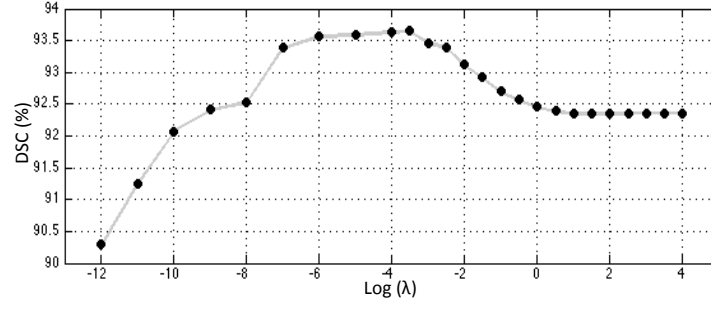
Figure 3.10: Dice similarity coefficient between the ribs and vertebral column segmentation algorithm and corresponding ground truth for a wide range of λ in Equation (2.1).
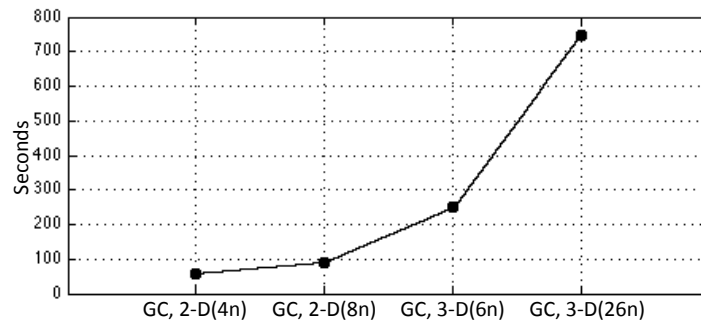
Figure 3.11: Run time for segmenting a 346 slice dataset with different graph sizes.

column.

(iii) Run time for segmentation with graph cut algorithm (in 2D and 3D with different neighbourhoods) is illustrated in Figure 3.11. From the time graph, it may be concluded that time complexity increases dramatically with number of neighbours and graph dimension.

(iv) Finally, the results of ribs segmentation with 2D (4 neighbours) graph cut and λ in graph cut energy function (Equation (2.1)) equal to 1, were analyzed in 3D. It was found that ribs 2, 5, 6, 7 and 8 at left and ribs 2, 3, 4, 5, 6, 8, 9 and 10 at right were detected in all datasets. Ribs 1, 3, 4, 9, 10 and 11 at left and ribs 1, 7 and 11 at right, were each missed once and rib 12 at left and right was missed twice, in all 18 datasets.

Table 3.4: Evaluation of the sternum segmentation in 16 MDCT datasets.

DSC (%)	$Sensitivity$ (%)	$Specificity$ (%)	FNR (%)	FPR (%)	d_{mean} (%)	d_{rms} (%)
91.76	92.49	99.51	7.51	0.49	1.07	1.72

3.3.2.3   Experiments on Sternum Segmentation Algorithm

To refine the sternum segmentation, active contours algorithm needs to be run twice with different parameters. To perform the experiments, the weight of the smoothing term and the number of iterations for the first running of actice contours were set to 15 and 2000 respectively, and for the second running they were set to 30 and 1000.

The front-view of the sternum segmentation results were compared to the corresponding reference masks. The sternum reference masks were delineated by the radiologist on OsiriX [5] output images. The xiphoid process was excluded from the reference mask, as the level of calcification of the xiphoid process is variable in different individuals.

The performance of the proposed algorithm for sternum segmentation and comparisons of the results to the reference masks were evaluated using different criteria. A summary of the evaluations is shown in Table 3.4.

To evaluate the accuracy of costal notches localization, the positions of fourteen costal notches on all datasets were manually marked in 3D and confirmed and corrected by the trained radiologist. The 3D Euclidean distance between the marked and automatically localized costal notches was measured individually. The average of the Euclidean distance error for fourteen costal notches, calculated from 16 datasets, is shown in Figure 3.12.

The comparison between the sternum segmentation from different studies and corresponding ground truth shows that the proposed algorithm works with high performance. DSC was 91.76% and d_{mean} and d_{rms} are as small as 1.07 mm and 1.72 mm respectively.
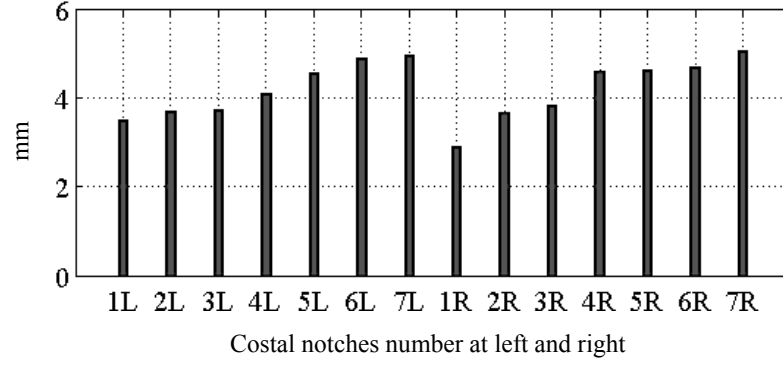
Figure 3.12: 3D Euclidean distance error of costal notches localization in 16 MDCT datasets.

Costal notches were localized in x, y and z directions accurately. The Euclidean distance error was only 4.2 mm on average over all notches of all datasets. Based on the Euclidean distance error bar chart in Figure 3.12, the first costal notches at left and right sides were estimated closest to their actual location. Also, as shown in Figure 3.12, it may be concluded that notches localization error increases as the notch number increases with almost the same pattern on both left and right sides.

3.4   Discussion

Graph cut based algorithm for 3D segmentation of the human lungs in MDCT images was tested, by varying the graph size and its effect on segmentation performance and speed. Evaluations show that increasing the graph size does not necessarily improve segmentation performance, but does affect the running time negatively. Based on evaluation, the 2D graph with 4 neighbours shows high performance with low running time, and is recommended for accurate and fast lung segmentation.

For 3D segmentation of the ribs and vertebral column in MDCT images, a novel and efficient algorithm based on graph cut followed by a two-step isolation refinement was presented and tested. Similar to the lung segmentation result, the evaluations show high performance and speed when 2D (4 neighbours) is used for ribs and vertebral column segmentation. In other words, the results of these experiments may help researchers interested in using graph cut for medical image segmentation. For those using graph cut as a part of the segmentation procedure, testing of different

graph sizes on a few datasets is recommended before running the algorithm on a larger dataset, to check the segmentation speed and performance.

The proposed algorithm for the ribs and vertebral column segmentation has potential to be used for other views of CT images, namely coronal and sagittal views. Furthermore, it can be developed for CT images that are saved with protocols other than non-contrast. The results of the proposed algorithm can assist clinicians to visualize quickly and accurately the segmented vertebral column and ribs in 3D. Also, it may be used as part of CAD systems to help identify abnormal lung tissue patterns by eliminating bony structure. Different λ values for different anatomical parts may be beneficial in improving the segmentation accuracy.

The proposed algorithm for 3D segmentation of the human sternum in lung MDCT images is novel and fully automatic. After the segmentation step, the isolation result was refined by employing active contours to remove existing calcified costal cartilage that is attached to the sternum. For each dataset, costal notches were localized in 3D by using a sternum mask and positions of the costal notches on it as reference.

The result of 3D sternum segmentation can be useful in sternum implant surgeries as well as studies involving sternum geometry analysis [39]. It can assist cosmetic surgeons performing sternum deformities correction to visualize the sternum in 3D and also in procedures predicting surgery outcome before the operation.

In most CT images, costal cartilages are low in contrast and the proposed costal notches positioning, will assist in prediction of costal cartilage centre points from CCJ to the sternum [98].

3.5   Summary

Proposed techniques for lung, ribs, vertebral column and sternum segmentation as well as costal notches localization were presented in this chapter. Details and different steps of each algorithm were covered. All techniques were tested for measuring the accuracy and the results were compared against corresponding ground truth. Evaluations proved that the algorithms accurately segment the organs in

3D. Furthermore, distance error of costal notches localization in 3D was measured. Average Euclidean distance between the marked and automatically localized costal notches was very small.

Graph cut based segmentation algorithms were tested to investigate how graph dimension and neighbourhood size affect the performance and running time. The experiments show state that increasing the graph size does not necessarily improve segmentation performance, but does affect the running time negatively.

Reconstruction and modelling of human organs will be dealt with in the next chapter. Techniques to automatically reconstruct human ribs and costal cartilages in 3D based on a patient's unique anatomy will be discussed. Moreover, an automatic algorithm for full diaphragm modelling in 3D will also be presented.

Chapter 4

Automatic Reconstruction and Modelling in 3D[1]

The importance of medical image computing is growing in medical diagnostics and image-guided therapy and 3D modelling is increasingly important. The objective for 3D modelling is to statistically model the anatomy of organs across subjects [56]. Medical image modelling has a wide range of applications in practice, for example to extract quantitative image parameters to support the surgeon during navigated intervention [56].

Ribs and costal cartilage reconstruction and diaphragm modelling are necessary steps for PPs and DPT extraction in 3D. Segmented upper trunk organs including the lung, rib, vertebral column and sternum provide necessary information for reconstruction. Techniques to extract the organs in 3D were presented in Chapter 3. Further, the results of the modelling contribute important information to subsequent steps in turn, including extraction of calcified pleura in the diaphragmatic area, estimation of the ribs and costal cartilage centre-lines as a surface, and calculation of its mean distance to the pleural costal surface, in order to extract the thickened pleura on the pleural costal surface.

The motivation and goals to be achieved of this work are explained in section 4.1. Frameworks of the proposed algorithms and technical details of the steps are provided

---
[1]Portions of the work have been published [107, 108, 109]

in section 4.2. All techniques are tested and evaluated by several experiments and the details are presented in section 4.3. The results of evaluation are discussed thereafter in section 4.4.

4.1 Motivation and Goals

Individual anatomy is variable and sometimes far from a standard atlas, and there is a need for a geometrically adjustable ribs and costal cartilage model. Accurate patient-customized rib reconstruction allows quantitative analysis of rib shapes. This would be useful in identifying deviations in anatomy that are associated with certain disease processes. It also allows detection of more subtle abnormalities, for example notching of a rib under its surface. Patient-customized rib reconstruction is valuable in rib implant surgery to reconstruct damaged rib(s) due to cancer or trauma.

The costal cartilage forms an integral part of the thoracic cage which is important in protecting the thoracic organs (e.g. heart, lungs) and assisting in respiration. Segmentation and therefore modelling of costal cartilage is more difficult than of the ribs, because their natural density is close to the adjacent soft tissue (e.g. muscles) and their degree of calcification varies considerably between individuals. The ability to accurately reconstruct costal cartilage has a wide range of benefits. In patients with structural abnormalities of the costal cartilage, such as chest wall deformities, (for e.g. pectus excavatum, pectus carinatum, microtia) availability of a quantitative model of the ribs and costal cartilages allows better surgical planning, and predictive modelling of potential anatomical and mechanical changes to the chest wall before any surgery. In cases of trauma or destruction (for e.g. from malignancy) of part of the costal cartilage, a quantitative model would allow mechanical and material properties of any potential synthetic chest wall to be assessed/investigated. Quantitative modelling of the costal cartilage and rib also has application in predicting the consequence of trauma/external forces to the chest wall, and in particular the entire thoracic cage.

A fully automatic algorithm for patient-customized rib and costal cartilage reconstruction in 3D is presented. In the presented algorithm, current geometric knowledge of the ribs and costal cartilage is employed for reconstruction of their

cross-sections along their lengths. The shapes of cross-sections are geometrically determined based on the patient's unique anatomy and the rib angle, length, curvature and mass. The main contributions of the algorithm are:

(i) 3D reconstruction of patient ribs directly from lung MDCT dataset

(ii) reconstruction of rib cross-sections individually at 100 sections along its length, using available rib geometry and anatomical studies

(iii) obtaining a patient specific and anatomically-faithful 3D reconstructed model, based on unique properties of each individual rib including angle, length, curvature and mass.

(iv) estimating the costal cartilage centrelines, based on patient's unique properties of sternum and corresponding rib's curvature and length

(v) 3D reconstruction of costal cartilage cross-sections along the estimated centreline, directly from lung MDCT dataset.

Despite the value of full diaphragm modelling, automatic diaphragm segmentation has remained a challenging task and mainly its top surface has been estimated in 3D. Strictly speaking, automatic segmentation of the full diaphragm directly from a patient's CT images is almost impossible due to (i) low thickness of the diaphragm (ii) irregular shape of the diaphragm and (iii) low contrast between the diaphragm and adjacent organs (see Figures 2.5a to 2.5c).

A novel algorithm for 3D modelling of the diaphragm from MDCT images is presented. Besides the accuracy achieved, the main contribution is the use of 3D spatial information of the ribs, costal cartilage and the vertebral column (as stable references), in addition to the lungs' lower surfaces to delineate the full diaphragm in 3D. The inner surfaces of the ribs, costal cartilage and the spinal column are used to model the diaphragm side boundary. Also the lower surfaces of the lungs determine the diaphragm top boundary and together with the side boundary, act as an encompassing boundary ($\mathbb{EB}$ hereafter) in 3D. By employing a 3D active contours model, starting from the centre of the boundary and expanding towards $\mathbb{EB}$, the full diaphragm is delineated accurately in 3D.

4.2 Reconstruction and Modelling Framework

In order to reconstruct the ribs and vertebral column and also model the diaphragm in 3D, the patient's anatomy information needs to be extracted from the MDCT dataset. The first step to obtain the patient's anatomy information is to segment organs in the dataset. The steps to segment the lung, ribs and sternum are explained in section 4.2.1.

By employing the anatomy information from the segmented ribs and sternum, the patient's ribs and costal cartilage are reconstructed accurately in 3D. A fully automatic algorithm is presented for reconstruction and its complete framework is provided in section 4.2.2. In addition to segmented organs with hard structure, the extracted lungs in 3D (already presented in section 3.2.3.1), provides information for full diaphragm modelling and the details are presented in section 4.2.3.

4.2.1 Preliminary Steps

The first stage for reconstructing and modelling the ribs, costal cartilage and diaphragm is the segmentation of organs in MDCT datasets. After converting MDCT slides to conventional intensity images, the lungs, ribs and vertebral column are extracted by the algorithms presented in section 3.2. Also, the sternum is isolated and costal notches are localized in 3D (see section 3.2.3.3 for details).

For accurate rib reconstruction, a key step is to estimate the rib centre-line. For this, isolating the rib in 3D and localizing its ends points are necessary. As mentioned earlier in section 2.1.3.1 and shown in Figures 2.7 and 4.2b, a rib articulates with a vertebra at the tubercle. The patient's ribs are segmented and tubercles are localized in 3D by:

(i) localizing the bone cross-sections at mid-coronal plane ($\mathbb{N}$ objects)

(ii) calculating $\mathbb{M}$, the mean area of $\mathbb{N}$ objects

(iii) tracing each of the $\mathbb{N}$ objects backward in the coronal direction in 3D
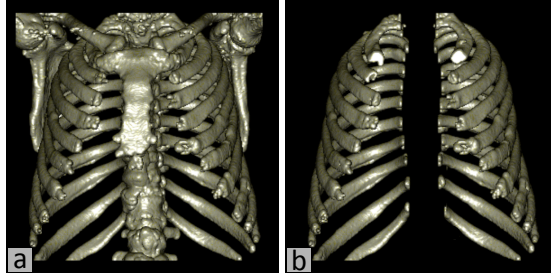
Figure 4.1: (a) Segmented bony structure (patient number 6, coronal view) and (b) ribs in 3D.
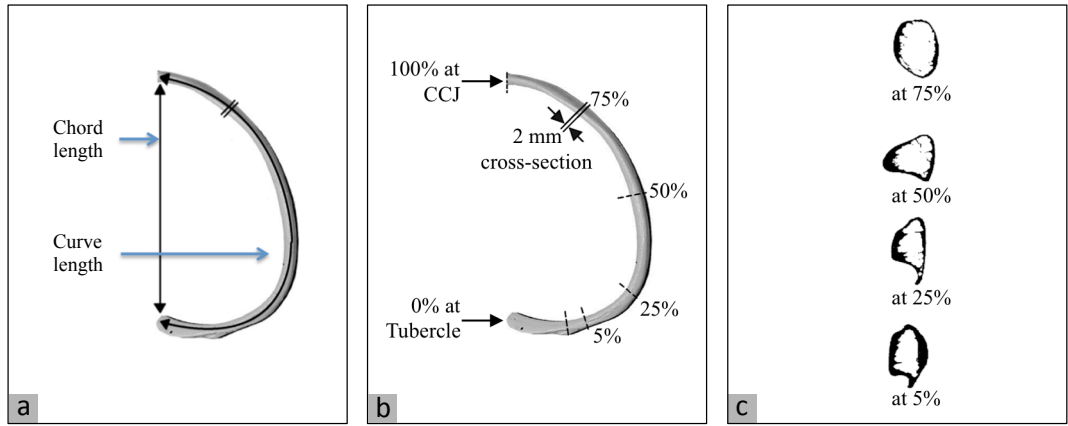
Figure 4.2: (a) The difference between chord and curve length of a rib (b) location of cross-sectional cut, between tubercle and CCJ [96] and (c) exemplary rib cross-sections [96].

(iv) stopping the tracing procedure for each object by applying a size constraint i.e. when area of a traced object is larger than twice $\mathbb{M}$

(v) cutting the ribs and vertebral column at the detected tubercle

(vi) identifying the biggest component as the vertebral column

(vii) removing the vertebral column in order to obtain the ribs.

Examples of segmented ribs, without other hard structures such as the sternum and vertebral column are shown in Figures 4.1 and 4.3c.
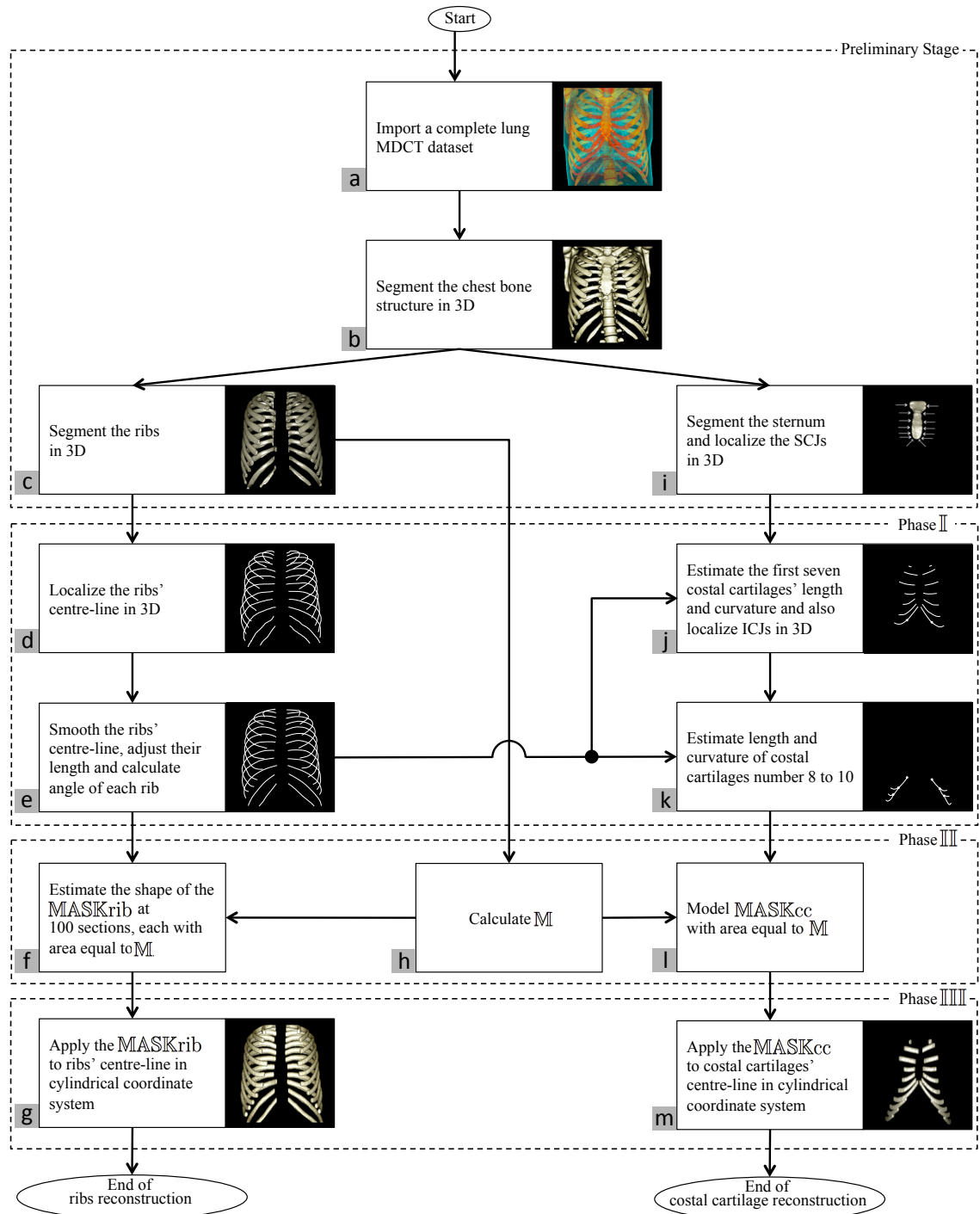
Figure 4.3: Flowchart of ribs and costal cartilage reconstruction in 3D, based on patient's MDCT dataset. Displayed images illustrate step-by-step reconstruction for patient number 11.

4.2.2   Patient-customized Ribs and Costal Cartilage Reconstruction

Ribs and costal cartilage are reconstructed in 3D based on patient's unique anatomy and the whole flowchart is shown in Figure 4.3. By using the results of the preliminary segmentation step (section 4.2.1), reconstruction is achieved in three phases: estimating the centre-line, customizing the cross-sectional shape and modelling in 3D. Each phase includes several steps that are summarized as follows:

Phase $\mathbb{I}$: The correct locations of ribs' and costal cartilages' centre-lines are estimated in 3D, based on a patient's dataset by:

   (i) localizing each rib's centre-line

  (ii) smoothing all centre-lines' curvature

 (iii) adjusting each rib's curve length (hereinafter length, see Figure 4.2a for illustration of the difference between chord and curve length of a rib)

  (iv) estimating angle of each rib

   (v) estimating the length and curvature of the first seven costal cartilages

  (vi) localizing all ICJs in 3D

 (vii) estimating lengths and curvatures of centre-lines corresponding to costal cartilages number 8 to 10.

Phase $\mathbb{II}$: Customize cross-sectional shape in the cylindrical coordinate system by:

   (i) calculating $\mathbb{M}$, mean area of all rib cross-sections at mid coronal plane

  (ii) customizing the rib cross-sectional shape in the cylindrical coordinate system in 100 sections

 (iii) estimating the model and size of costal cartilage cross-sectional shape.

Phase $\mathbb{III}$: Ribs and costal cartilage reconstruction in 3D by:

(i) modelling each rib by applying corresponding 100 customized cross-sections to the estimated centre-line

(ii) modelling the costal cartilages by applying the customized cross-sections to the estimated centre-line.

Details of the three phases and steps are presented in subsections 4.2.2.1 to 4.2.2.3.

4.2.2.1 Phase I: Centre-line Estimation in 3D

Often, rib segmentation from MDCT images returns discrepant rib lengths with inaccurate cross-sectional borders. This may be the result of low resolution, inaccurate rib segmentation technique or excessive costal cartilage calcification. A novel algorithm is presented to reconstruct each rib individually based on the patient's individual skeleton and the unique angle, length, curvature and mass of each rib. The algorithm also provides a technique for costal cartilage reconstruction in 3D.

To estimate the ribs and costal cartilage centre-lines on the left and right sides, the following steps are followed:

(i) Localize and smooth each rib's centre-line in 3D:
The centre-line of each rib is localized in 3D in the cylindrical coordinate system (with longitudinal axis perpendicular to the axial plane and the origin at the centre of the plane, see Figure 4.4 for illustration of ribs in the cylindrical coordinate system).

Due to the discrete nature of CT images and the fact that image segmentation is not completely accurate, the rib centre-lines do not present a smooth curve in 3D (see Figure 4.5b for an example). As suggested [73, 98], irregular curvature of a rib's centre-line may be smoothed by using a smoothing spline (see section 2.5.1.4 for details about smoothing spline). In Figure 4.5c, the toothed centre-line in Figure 4.5b is smoothed by a smoothing spline.

(ii) Adjust each rib's curve length:
As mentioned earlier, some ribs are segmented shorter or longer than their
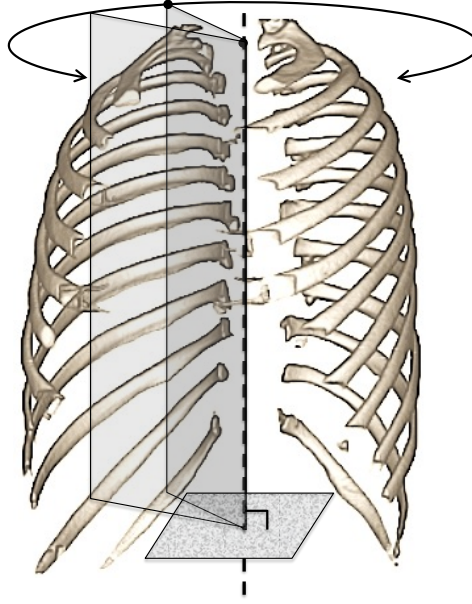
Figure 4.4: Illustration of ribs (chosen from a test dataset) in the cylindrical coordinate system.

actual lengths. Known anatomical knowledge [62] is used to adjust the rib lengths. Suppose $2 \times n$ is the total number of ribs in a dataset. If l_{li} and l_{ri} denote lengths of the segmented rib number i on the left and right respectively, then for each dataset:

$$LengthRatio = (\sum_{i=1}^{n} l_{ri} + \sum_{i=1}^{n} l_{li})/(2 \times \sum_{i=1}^{n} L_i) \qquad (4.1)$$

where L_i is the length of the characterized rib number i. $\mathbb{L}_{li}$ and $\mathbb{L}_{ri}$, the adjusted lengths of rib number i on the left and right, are estimated to have equal length i.e.

$$\mathbb{L}_{li} = \mathbb{L}_{ri} = \mathbb{L}_i \qquad (4.2)$$

and

$$\mathbb{L}_i = LengthRatio \times L_i \qquad (4.3)$$

If the length of a rib is adjusted to be longer (for example top rib in Figure 4.5a), the centre-line of the missing part towards the CCJ, is estimated by applying the smoothing spline parameters from step (i). Examples of smoothed rib centre-lines with adjusted lengths are shown in Figures 4.3e and 4.5c. Moreover, Figure 4.5d illustrates how irregularly segmented ribs, in terms of length, are
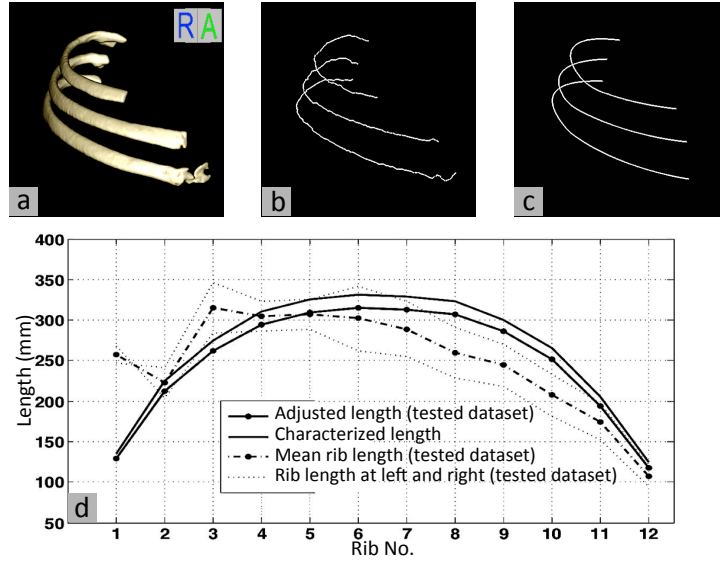
Figure 4.5: (a) 3D view of three consecutive ribs (patient number 7) (b) rib centre-lines (c) smoothed centre-lines with adjusted lengths and (d) patient number 7's adjusted rib lengths based on rib characterization [62].

adjusted.

(iii) Estimate angle of each individual rib:

There exists information and characterization of ribs mean angle [62] and curvature [96]. However, as a change in rib angle causes a significant change in cross-sectional shape (to be shown in step (ii) of section 4.2.2.2), each rib angle is estimated individually. The angle of each rib is calculated by:

   (iii.i) estimating the smoothed and adjusted length rib centre-line as a flat surface and

   (iii.ii) finding θ, the angle of the flat surface and horizontal plane.

In Figure 4.6c, the beginning and the end of the sixth rib are marked with white crosses and the plane labeled 3 illustrates the flat surface, fitted to the rib centre-line.

(iv) Estimate the length and curvature of the first seven costal cartilages:

As mentioned in step (i), rib centre-lines exhibit toothed curvature and are smoothed by a smoothing spline [73, 98]. See Figures 4.7b and 4.7d for examples of irregular and smoothed curvature of rib centre-lines respectively.
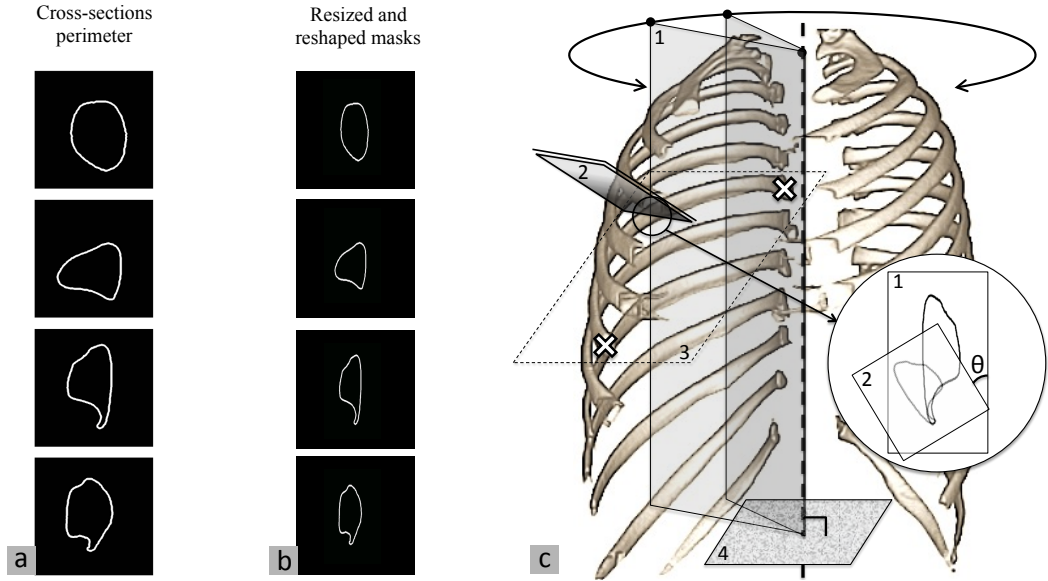
Figure 4.6: (a) perimeter of exemplary cross-sections ($\mathbb{R}$ib$\mathbb{EXMP}$) [96] (b) resized and reshaped $\mathbb{R}$ib$\mathbb{EXMP}$s based on individually tested rib characteristics and (c) illustration of how cross-sectional masks are stretched according to the rib angle (Surface 1 illustrates the cylindrical coordinate system and surface 4 shows the horizontal plane. Surface 3 is a flat surface, fitted to the rib centre-line and its start and end are marked with white crosses. Surface 2 is a perpendicular cut to the fitted surface. Angle θ between surfaces 1 and 2 equals to the angle between surfaces 3 and 4).

The centre-lines of ribs number one to seven bilaterally and their extensions from CCJ towards the related SCJ (i.e. centre-line of the first seven costal cartilages bilaterally) are approximated by a smoothing spline. Strictly speaking, a smooth curve is fitted to points on a rib centre-line (see Figure 4.7b) and forced to start from its tubercle and end in the corresponding SCJ (see Figure 4.7c).

(v) Localize all ICJs in 3D:

As explained in step (ii) and shown in Figures 4.7a and 4.7b, some ribs may be segmented shorter or longer than their actual lengths due to the low resolution of CT images or excessive costal cartilage calcification. Therefore, by adjusting the curve length of each rib individually (see Figure 4.7d), the first seven CCJs are localized in 3D. Next, the centre-lines of each of the first seven costal cartilages are determined, which are the fitted splines minus the rib centre-lines (see Figures 4.3j and 4.7e).
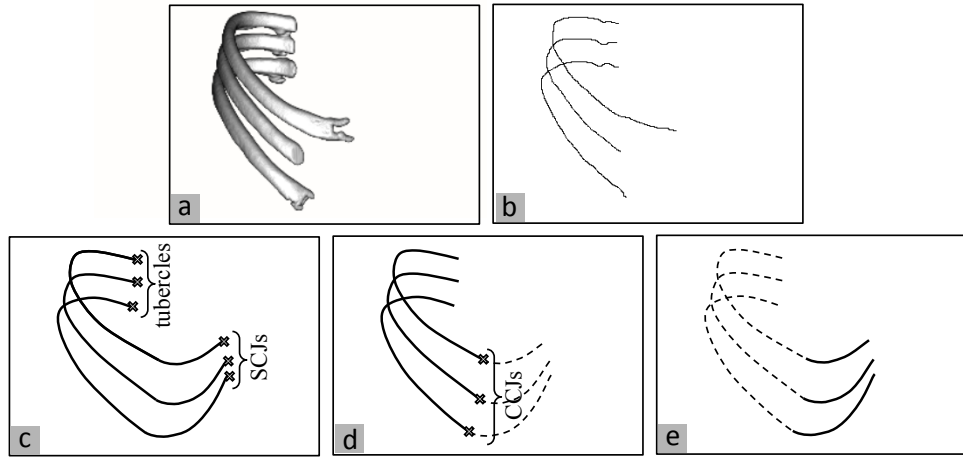
Figure 4.7: (a) 3D right anterior oblique view of ribs number 5 - 7 (patient number 15), (b) ribs irregular centre-line, (c) smoothing splines, each forced to start from related tubrcle and end in its SCJ, (d) ribs smoothed centre-line with adjusted length and (e) estimated centre-lines of costal cartilage number 5 - 7 at right.
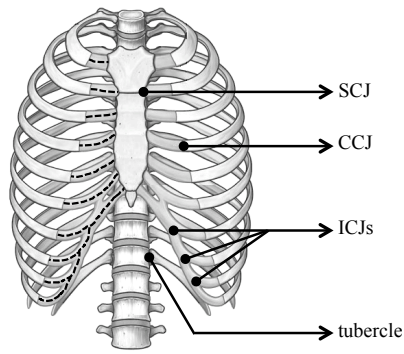
Figure 4.8: Dashed lines illustrate the assumption about costal cartilage extensions from CCJs towards SCJs or ICJs [42].

(vi) Estimate lengths and curvatures of centre-lines corresponding to costal cartilages number eight to ten:

As shown by dashed lines in Figure 4.8, the positions of ICJs are assumed to be in the middle of the centre-line of the preceding cartilage. The same method employed for centre-line of ribs number one to seven is used to fit the centre-line of ribs number eight to ten and their extensions from CCJ towards corresponding ICJ to smoothing splines. By subtracting the rib centre-lines, to which their lengths are already adjusted, the centre-lines of costal cartilages number eight to ten are determined in 3D (see an example in Figure 4.3k).

4.2.2.2 Phase $\mathbb{II}$: Cross-sectional Shape Customization in the Cylindrical Coordinate System

The rib cross-sectional shape, $\mathbb{MASK}$(Rib) hereafter, and costal cartilage cross-sectional shape, $\mathbb{MASK}$(CC) hereafter, are modelled based on patient's anatomy in three steps:

(i) Calculating $\mathbb{M}$, mean area of all rib cross-sections at mid coronal plane:
   To customize the reconstruction algorithm, ribs and costal cartilage cross-sectional areas need to be adjusted to the patient's anatomy. To estimate $\mathbb{M}$, after segmenting the ribs in 3D, cross-sections of all ribs (N objects) at mid-coronal plane are considered. $\mathbb{M}$ is calculated as:

$$\mathbb{M} = (\sum_{i=1}^{N} a_i)/N \qquad (4.4)$$

   where:
   N: total number of rib cross-sections at mid-coronal plane
   a_i: area of the rib cross-section no. i at mid-coronal plane.

(ii) Customizing the rib cross-sectional shape in 100 sections:
   There exists limited information on the accurate shape of a rib cross-section. Accurate exemplary cross-sections at 5%, 25%, 50% and 75% of rib length are available [96], obtained by examining ribs number three to nine of fresh frozen human cadavers (see Figures 4.2b and 4.2c for exemplary rib cross-sections and the definition of rib length as 0% at tubercle and 100% at CCJ). The perimeters of exemplary cross-sectional shapes (as shown in Figure 4.6a), the $\mathbb{RibEXMP}$ hereinafter, are used in the algorithm. All other cross-section characteristics such as height, width and area are directly extracted from the patient's CT dataset. Two assumptions have been made to obtain 100 $\mathbb{MASK}$(Rib)s for reconstructing a rib cross-section along its adjusted length:

   (ii.i) the missing $\mathbb{RibEXMP}$s between 5%, 25%, 50% and 75% of rib length are a smooth transition between two available consecutive $\mathbb{RibEXMP}$s

(ii.ii) $\mathbb{R}\text{ib}\mathbb{EXMP}$s from 0% to 4% and $\mathbb{R}\text{ib}\mathbb{EXMP}$s from 76% to 100% have the same shape as the $\mathbb{R}\text{ib}\mathbb{EXMP}$s at 5% and 100% respectively

In the biometric study [96], ribs of human cadavers were cut perpendicular to the ribs. The proposed reconstruction technique is based on the cylindrical coordinate system, and estimated rib angle θ is used to calculate the level of $\mathbb{R}\text{ib}\mathbb{EXMP}$s stretching in the system. In Figure 4.6c, a rib cross-section obtained from a perpendicular cut to the rib [96] (surface number 2), is stretched in the cylindrical coordinate system (surface number 1), assuming that reconstruction is in the cylindrical coordinate system.

Suppose i and m are the number of ribs and cross-sectional shapes $\mathbb{MASK}(\text{Rib})$, and H^m and $\mathbb{H}^m_i$ denote the heights of the original and the stretched $\mathbb{R}\text{ib}\mathbb{EXMP}$ respectively. If H_iRatio represents the level of height stretching for the rib i then:

$$H_iRatio = 1/\cos\theta_i \tag{4.5}$$

$$\mathbb{H}^m_i = H^m \times H_iRatio \tag{4.6}$$

To adjust the reconstructed volume to the patient's anatomy, the area of the $\mathbb{MASK}(\text{Rib})$s has to be modified as well. An earlier study [96] showed that cross-sectional area remains nearly constant along the rib. Therefore, the level of $\mathbb{SM}^m_i$ resizing/scaling is calculated to obtain $\mathbb{MASK}(\text{Rib})^m_i$ as:

$$ScaleRatio = \overline{Area}_{cs_i}/Area_{\mathbb{SM}^m_i} \tag{4.7}$$

where cs_i denotes the cross-section of rib i from the patient's MDCT dataset, $\mathbb{SM}^m_i$ is the stretched mask (from the previous step) and $\mathbb{MASK}(\text{Rib})^m_i$ represents the final estimated mask at section m for the rib number i. Examples of $\mathbb{MASK}(\text{Rib})^5$, $\mathbb{MASK}(\text{Rib})^{25}$, $\mathbb{MASK}(\text{Rib})^{50}$ and $\mathbb{MASK}(\text{Rib})^{75}$ are shown in Figure 4.6b.

(iii) Estimating the model and size of costal cartilage cross-sectional shape: Although recent studies have discussed accurate rib geometry and anatomy, there is no accurate data about the geometry of human costal cartilages
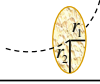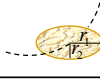
Cross-sectional/*MASK* model	Dimension calculation
a	$r = \sqrt{\mathbb{M}/\pi}$
b	$r_1 = r_2/2$ $r_1 = \sqrt{\mathbb{M}/(2 \times \pi)}$
c	$r_1 = 2 \times r_2$ $r_1 = \sqrt{(2 \times \mathbb{M})/\pi}$
d	$Ratio_{rescaling} = \mathbb{M}/M'$ M' : Area of rib cross-section at 75% of curve length

Figure 4.9: Dimension calculation and assumed models for $\mathbb{MASK}$(CC): (a) circle, (b) vertical ellipse, (c) horizontal ellipse and (d) irregular shape [96]. ($\mathbb{M}$ is the mean area of all rib cross-sections at mid coronal plane).

particularly in terms of cross-section. Therefore, four different models are assumed for $\mathbb{MASK}$(CC) (see Figure 4.9) including: circle, vertical ellipse, horizontal ellipse and an irregular shape. The model Figure 4.9d is taken from a bio-metric study of accurate rib anatomy [96] and also used in step (ii) for patient-customized rib reconstruction in 3D. The irregular shape is assumed to be similar to the exemplary cross-section of the rib at 75% of rib length [96]. Methods for calculating the dimensions of different shapes of $\mathbb{MASK}$(CC) are shown in Figure 4.9.

4.2.2.3 Phase $\mathbb{III}$: Patient-customized 3D Reconstruction in the Cylindrical Coordinate System

At this point, the lengths and curvatures of centre-lines of the ribs and costal cartilage have been accurately determined in 3D. Also, $\mathbb{MASK}$(Rib) and $\mathbb{MASK}$(CC) are modelled based on patient's anatomy. Estimated centre-lines and cross-sectional models are used for rib and costal cartilage reconstruction.

(i) Rib reconstruction in 3D

To reconstruct the ribs in 3D, patient-customized $\mathbb{MASK}$(Rib)s are applied to the estimated centre-lines. In other words, to reconstruct rib number i, its adjusted length is divided into 100 sections and $\mathbb{MASK}$(Rib)$_i^m$ is applied to section m. This step is run on all ribs individually. An example of reconstructed

Patient no. 3   Patient no. 6   Patient no. 9   Patient no. 8
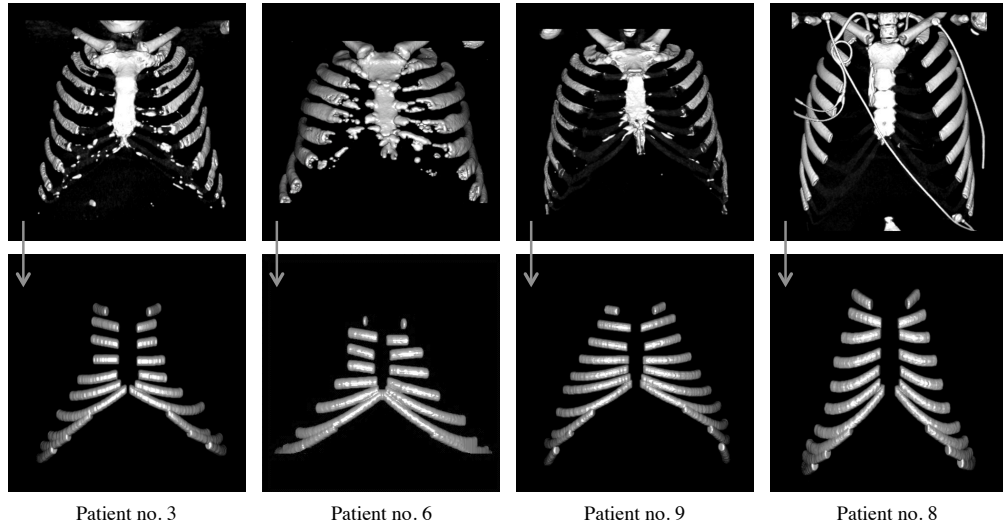
Figure 4.10: Top row: original MDCT datasets (half front coronal view) and bottom row: result of costal cartilage reconstruction in 3D (coronal view). From left to right, the assumed $\mathbb{MASK}(CC)$ is circle, vertical ellipse, horizontal ellipse and the irregular shape (as shown in Figure 4.9).

ribs based on patient's anatomy is shown in Figure 4.3g.

(ii) Costal cartilage reconstruction in 3D

At the final step of costal cartilage reconstruction, by applying an assumed $\mathbb{MASK}(CC)$ (as shown in Figure 4.9) to the cartilage centre-lines in the cylindrical coordinate system, 3D reconstruction is achieved.

Examples of costal cartilage reconstruction in 3D from real patient MDCT datasets are shown in Figures 4.3m and 4.10. In Figure 4.10, patient numbers 3 and 9 were 69 and 18 years old respectively at the time of radiography, and their MDCTs represent high and non costal cartilage calcification respectively. The reconstruction results (bottom row in Figure 4.10) illustrate how well the presented algorithm models the costal cartilages and is applicable to MDCTs with various degrees of cartilage calcification.

4.2.3 Full Diaphragm Modelling in 3D

A novel algorithm for 3D modelling of the full human diaphragm from lung MDCT images is presented in this section. The flowchart of the proposed algorithm for full diaphragm modelling is illustrated in Figure 4.11. The reconstruction algorithm
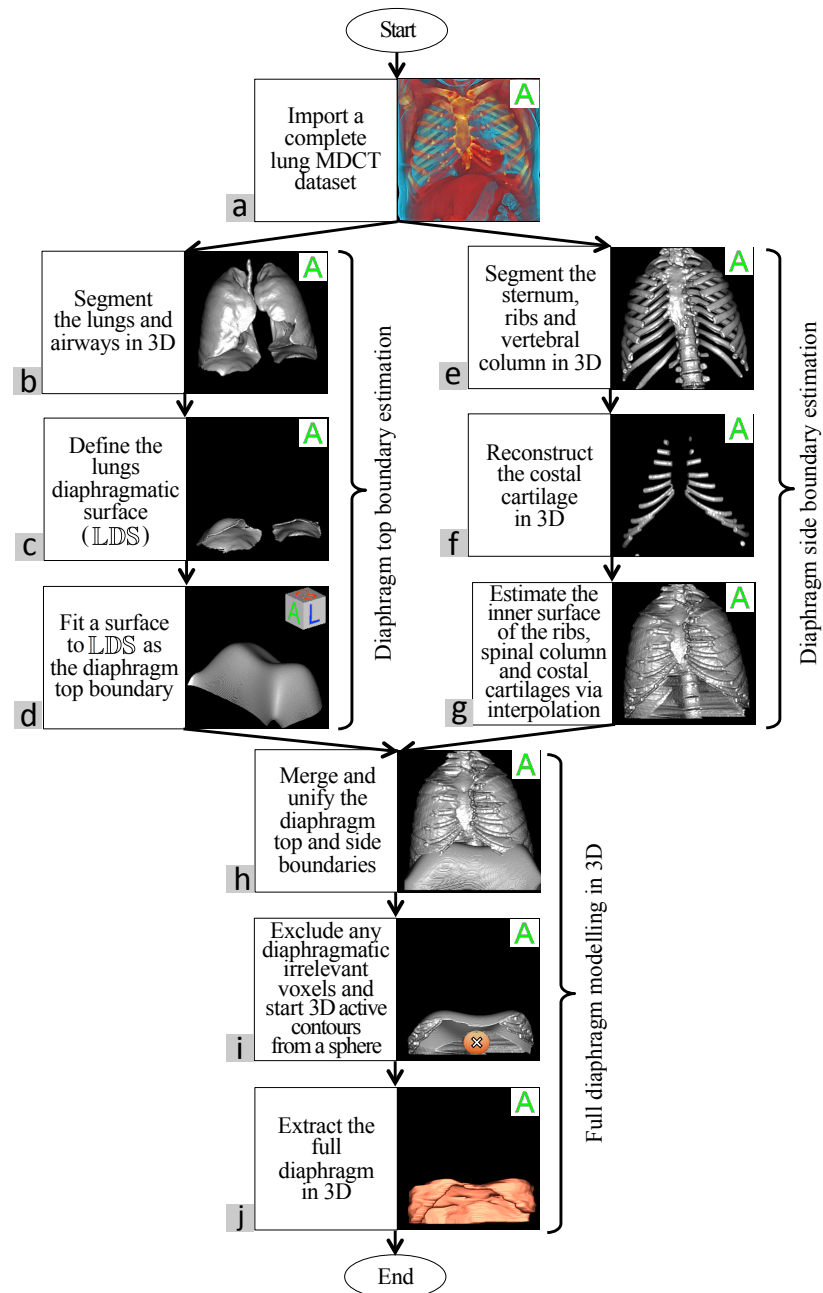
Figure 4.11: Flowchart of diaphragm 3D modelling directly from patient's MDCT dataset. Displayed images illustrate step-by-step diaphragm modelling for patient number 1.

is divided into three main parts: (i) estimating the diaphragm top boundary (ii) estimating the diaphragm side boundary and (iii) modelling the full diaphragm in 3D.
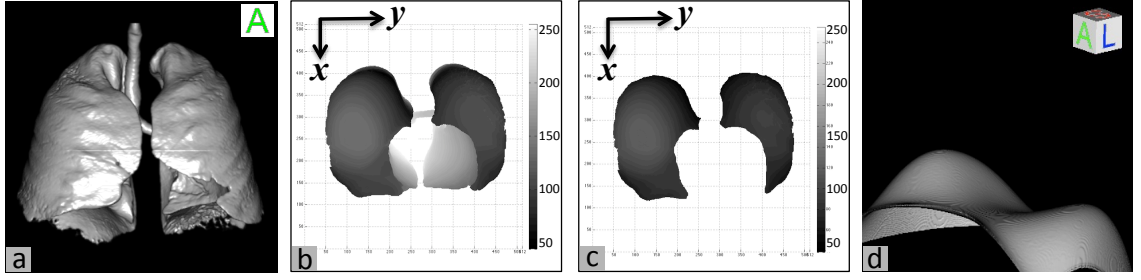
Figure 4.12: (a) Segmented lungs and airways of patient number 7 (b) $\mathbb{LLS}$ (c) $\mathbb{LDS}$ and (d) diaphragm top boundary, estimated by fourth degree polynomial surface.

4.2.3.1 Estimating the Diaphragm Top Boundary

Based on segmented lungs, the lung diaphragmatic surfaces ($\mathbb{LDS}$) are defined in 3D. If the segmented lungs are represented in Cartesian coordinate system, both lungs' lower surfaces ($\mathbb{LLS}$) i.e. $\{\, v_i,\ i = 1, 2, ..., M \,\}$ are a set of voxels $V_i = (X_i, Y_i, Z_i)$ where Z_i is the lowest value for the point (X_i, Y_i). As shown in Figure 4.12b, most often $\mathbb{LLS}$ contains the trachea and lower surfaces of the bronchi, as well as other lung surfaces irrelevant to the diaphragmatic surface. Instead, $\mathbb{LDS}$ may be defined as $\mathbb{LLS}$ voxels whose nomal vector is pointing down and inward within a certain interval [150]. In mathematical terms, if n_{V_i} is the normal vector of the surfaces $\mathbb{LLS}$ at V_i, then $\mathbb{LDS}$ is defined as $\{l_i = v_i, i = 1, 2, ..., m, m \leq M\}$ where the condition $\{-(0.75 * \pi) < n_{V_i} < -(0.25 * \pi)\}$ is satisfied [150]. $\mathbb{LDS}$ is defined as the two biggest components of l_i, refined by the closing operation followed by filling holes (see Figures 4.11c and 4.12c).

The final step of the diaphragm top boundary estimation is the fitting of a surface to the points of $\mathbb{LDS}$. Thin plate spline has been proposed [150] as a good candidate for surface fitting. However, in the current work, the diaphragm top boundary is approximated in 3D via linear and polynomial interpolation as it is much faster than 3D thin plate interpolation (see Figures 4.11d and 4.12d for illustrations of fitted surfaces).

4.2.3.2 Estimating the Diaphragm Side Boundary

The inner surfaces of the sternum, ribs, spinal column and costal cartilages are estimated in 3D by applying the following steps to each slice (axial direction):
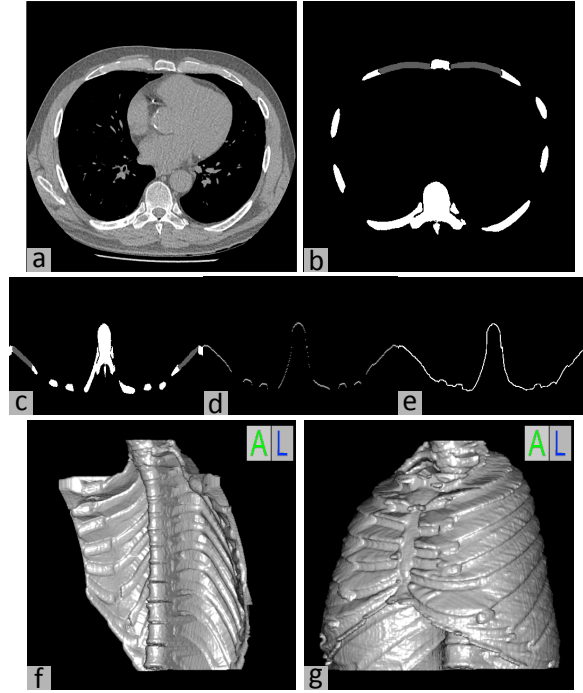
Figure 4.13: (a) Slice number 206 from patient number 7 datasets in axial direction (b) and (c) segmented ribs, sternum and spinal column (white pixels) together with reconstructed costal cartilage (grey pixels) in polar and Cartesian coordinate system respectively (d) top points (of the components in (c)) (e) fitted curve to the top points via linear interpolation (f) and (g) inner surfaces of the ribs, sternum, spinal column and costal cartilage in the Cartesian and cylindrical coordinate system respectively.

(i) convert the image from polar to Cartesian coordinate system (see Figure 4.13c)

(ii) find the top points (see Figure 4.13d)

(iii) estimate the top points as a curve via linear interpolation (see Figure 4.13e). Linear interpolation is used for estimation as it is fast and even though curves are estimated separately (slice by slice), the inner surface represents a consistent surface in 3D (see Figure 4.13f for 3D illustration).

(iv) convert the result from Cartesian to polar coordinate system (see Figures 4.11g and 4.13g).

4.2.3.3 Modelling the Full Diaphragm in 3D

The full diaphragm is modelled by employing 3D active contours [135], which is an extension of the "Snakes" segmentation method [28, 29, 69] in higher dimension.
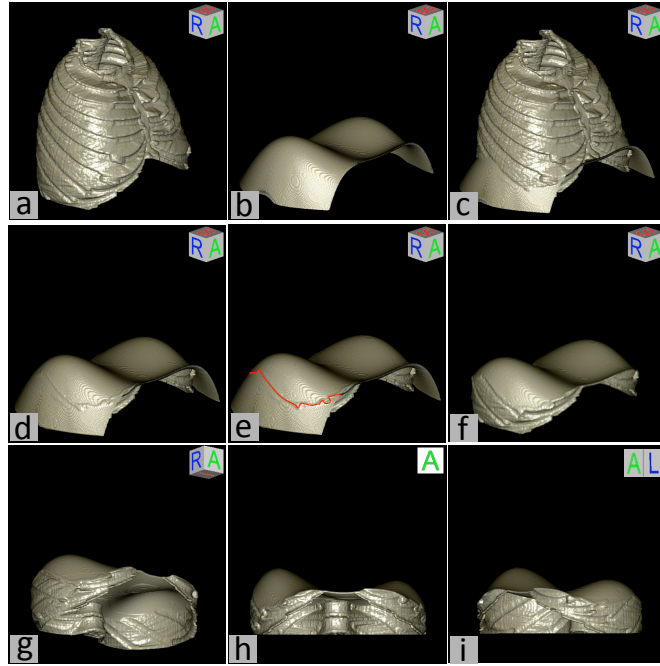
Figure 4.14: (a) to (c) Side, top and unified boundaries, estimated for patient number 11, (d) side boundary removed above the top boundary, (e) parts of top and side boundary intersections is highlighted by red line, (f) to (i) different views of estimated $\mathbb{EB}$.

Generally, the 3D active contour is initialized at a predefined mesh and expands towards a predefined 3D boundary (see Section 2.5.1.3 for more details about active contours).

In the proposed algorithm, encompassing boundary ($\mathbb{EB}$) is determined in two steps:

(i) merging and unifying the diaphragm top and side boundaries in 3D by logically adding corresponding slices of two volumetric data (see Figures 4.11h and 4.14c for two examples and Appendix D for pseudo code).

(ii) removing diaphragmatically irrelevant voxels. Here, irrelevant voxels are those that do not act as a boundary for the diaphragm. In other words, any side boundary voxels above the top boundary and any top boundary voxels out of the side boundary do not impact the 3D active contour and therefore are considered as irrelevant voxels. As shown in Figure 4.14d, all side boundary voxels above the top boundary are removed. Part of the side and top boundary intersection is highlighted in Figure 4.14e by red line. Any top boundary

voxels out of the intersection are considered irrelevant and are removed (see Figures 4.14f to 4.14i for different views of $\mathbb{EB}$ and Figure 4.11i for another example). Pseudocode for removing the boundary irrelevant voxels are provided in Appendix E.

Starting from the centre of $\mathbb{EB}$ (white cross in Figure 4.11i), a symmetrical polygon mesh (i.e. sphere) is forced to act as the initial 3D active contour that expands towards $\mathbb{EB}$. To determine the seed point automatically, 3D convex hull of the $\mathbb{EB}$ is determined and its centre is set as the active contour seed point position. The number of active contour evolving iterations and parameters are chosen so that the deforming mesh fills sharp corners of $\mathbb{EB}$ while keeping the surface smooth.

As the final step, the convex hull of $\mathbb{EB}$ is determined slice by slice (in axial direction) and pixels of the evolved contour inside the convex hull are identified as the diaphragm. In Figure 4.15.a, segmented ribs, vertebral column and reconstructed costal cartilage (grey pixels) from slide number 275 of patient number 5 dataset, are shown and their inner side is assumed as diaphragm side boundary (see Figure 4.15.b). 3D Active contour initiates from a sphere (shown as a red dashed circle in Figure 4.15.b) and expands towards the boundary. Evolved active contour is shown in Figure 4.15.c. Convex hull of the boundary, as shown in Figure 4.15.d, is employed to exclude the active contour out of the boundary, in order to estimate the shape of the diaphragm (see Figure 4.15.f).

The reconstructed diaphragm in 3D from thoracic MDCT dataset of patient number 1 is shown in Figure 4.11j.

4.3 Performance Evaluation

To measure the performance and accuracy, all algorithms were tested separately. Each algorithm was run on a set of MDCT datasets and the results were evaluated using different criteria. The following subsections provide details about the datasets used, experiments and evaluations.
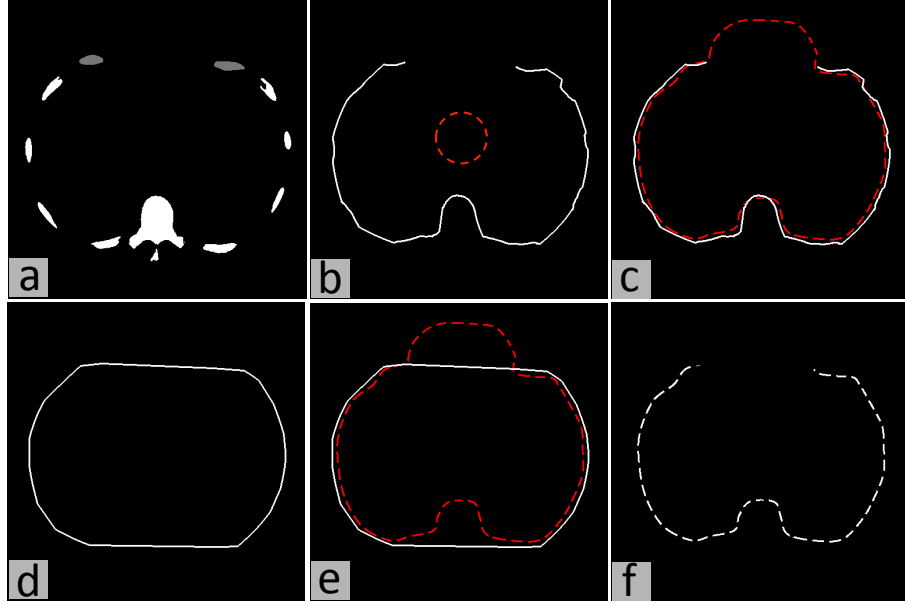
Figure 4.15: (a) Segmented ribs, vertebral column and reconstructed costal cartilage (grey pixels) from slide number 275 of patient number 5, (b) diaphragm side boundary and active contour initial shape (red dashed circle), (c) expanded and stopped active contour (red dashed closed line), (d) convex hull of the side boundary, (e) employing the convex hull to exclude active contour out of the boundary and (f) modelled diaphragm in slide number 275.

4.3.1 Material

The proposed algorithms for ribs and costal cartilage reconstruction as well as the algorithm for diaphragm modelling were tested on 15 complete MDCT datasets. All datasets share the same technical description provided in section 2.5.2.1 and Table 2.1. Demographic data of MDCT datasets, used for evaluating the reconstruction and modelling algorithms, are summarised in Table 4.1.

4.3.2 Experiments and Results

Each technique presented in this chapter was tested separately to measure the accuracy and performance. The result of each experiment was compared with corresponding ground truth using different criteria. Selected images for evaluation were marked and corrected by an experienced radiologist [1] to obtain reference masks. The following sub-sections provide details of the evaluations.

---

[1]Medical Imaging Department, Prince of Wales Hospital, Sydney, NSW, Australia.

Table 4.1: Demographic data of MDCT studies, used for testing and evaluating ribs and costal cartilage reconstruction as well as diaphragm modelling techniques.

MDCT Dataset	
Number of studies	15
Number of slices (per dataset)	380 (on average)
Patient	
Sex	
Male	36%
Female	64%
Age	
Mean	65.5
Range	18 - 86

Table 4.2: Evaluation of rib reconstruction algorithm and average distance errors based on 15 MDCT datasets.

Distance Error Metric $\rightarrow$ Evaluated Plane $\downarrow$	d_{mean}	d_{rms}
mid-coronal plane	0.57	0.82
mid-axial plane	1.31	3.09

4.3.2.1   Experiments on Ribs Reconstruction

The performance of the proposed algorithm for 3D reconstruction of ribs 3 to 9, presented in section 4.2.2, was evaluated quantitatively and qualitatively. For quantitative evaluation, mid-axial and mid-coronal planes from each dataset (30 planes in total) were chosen for performance assessment. In each plane, the bony structures were initialized with the graph cut algorithm and the rib borders were corrected and localized by the radiologist to obtain reference masks.

The distance error between the reference masks and the reconstruction results was measured with two distance metrics, namely d_{mean} and d_{rms} (see section 2.5.2.2 for mathematical formulas) and the result is summarized in Table 4.2. Also, Figure 4.16 shows the distance error for 15 patients individually.

To perform qualitative evaluation, three coronal planes of each dataset (coronal planes number 256 (mid-coronal) and 256$\pm$10) were chosen and the results of rib
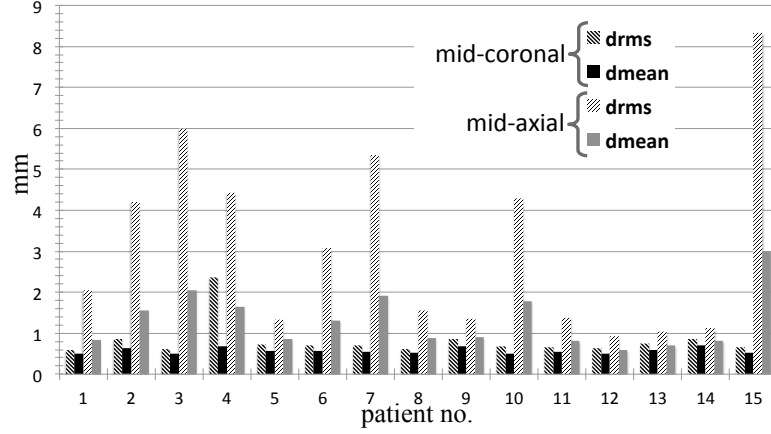
Figure 4.16: d_{mean} and d_{rms} between ground truth and reconstruction result for rib reconstruction.
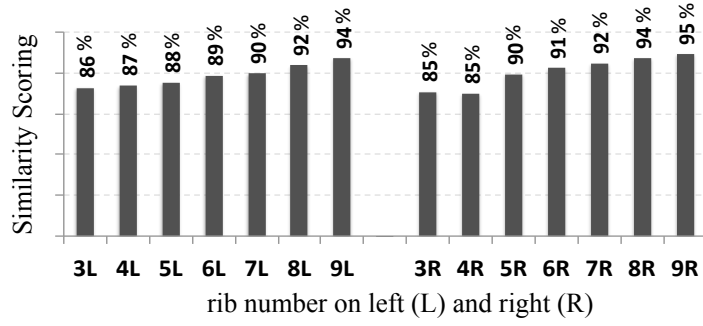
Figure 4.17: Percentage of similarity scores between the reconstructed ribs and original DICOM images.

reconstruction were overlaid on the corresponding DICOM images. All ribs in the overlaid images (45 in total) were assessed individually and scored from 0 to 100 by the radiologist. Scoring was based on morphological similarity, with higher scores indicating more similar shape and 100 being a complete match. The results of similarity scoring are illustrated in Figure 4.17.

4.3.2.2 Experiments on Costal Cartilage Reconstruction

As far as is known, the accuracy of algorithms for human costal cartilage reconstruction has not been reported. In this work, frequently used methods for quantitative evaluation of modelling and reconstructing other parts of the human body were reviewed and used in the experiments. To create ground truth and comparison reference, original MDCT datasets were considered in blinded fashion. From each dataset, two sagittal planes at the right and left, which include the maximum number

of costal cartilage cross-sections, were chosen (30 sagittal planes in total), and the border of each costal cartilage cross-section on the planes was carefully marked by the radiologist.

Each plane of ground truth was compared with the corresponding sagittal plane from the reconstructed model. Comparisons were performed for four assumed cross-sectional shapes, each with area equal to and twice $\mathbb{M}$. Costal cartilage number one was excluded from the ground truth and results, as the first rib cross-sectional shape is broad and flat [42] and different from other ribs.

As listed in Table 4.3, eight criteria were used for performance evaluation (see section 2.5.2.2 for mathematical formulas). *Distance* measures mean distance between costal cartilages centre-points in ground truth and reconstruction result, and distance error between their borders is measured by D_{mean} and D_{rms}.

The results of quantitative evaluations are summarized in Table 4.3 and the best result of each criterion is highlighted.

4.3.2.3 Experiments on Diaphragm Modelling

Run time for automatic modelling of the diaphragm was measured to compare the algorithm and manual segmentation speeds. All processing and evaluations were performed on a standard computer with 2.53 GHz CPU speed and 4 GB RAM. Based on experiments, the run time for diaphragm modelling is roughly 9 minutes, while manual extraction usually takes 3 hours. The run time break down is as follows:

  (i) estimating diaphragm top boundary $\approx$ 60 seconds

 (ii) estimating diaphragm side boundary $\approx$ 270 seconds

(iii) unifying top and side boundaries and excluding irrelevant voxels $\approx$ 30 seconds

(iv) running 3D active contour and identifying $\mathbb{EB}$ neighbouring voxel as diaphragm $\approx$ 180 seconds.

Testing the datasets with different parameter values resulted in different performances. After several experiments, the following parameters values were set for final

Table 4.3: Evaluation of costal cartilages reconstruction algorithm, tested on 15 MDCT datasets.

Performance metric →		DSC (%)	Sensitivity (%)	Specificity (%)	FNR (%)	FPR (%)	Distance (mm)	d_{mean} (mm)	d_{rms} (mm)
Costal cartilage cross-section ↓									
Shape	Area								
Circle	M	65.77	51.10	**99.99**	48.90	**0.01**	2.12	2.02	2.89
	2 × M	**77.45**	**84.79**	99.93	**15.21**	0.07	2.75	1.74	2.49
Horizontal ellipse	M	62.85	48.19	**99.99**	51.81	**0.01**	**2.01**	2.01	2.89
	2 × M	74.79	75.83	99.95	24.17	0.05	2.21	1.79	2.57
Vertical ellipse	M	61.49	49.68	99.98	50.32	0.03	2.48	1.95	2.77
	2 × M	54.85	72.74	99.77	27.26	0.23	4.03	**1.68**	**2.38**
Rib cross-section*	M	65.03	50.83	**99.99**	49.17	**0.01**	2.16	1.98	2.82
	2 × M	74.56	84.31	99.64	15.69	0.36	3.14	1.69	2.42

*at 75% of curve length
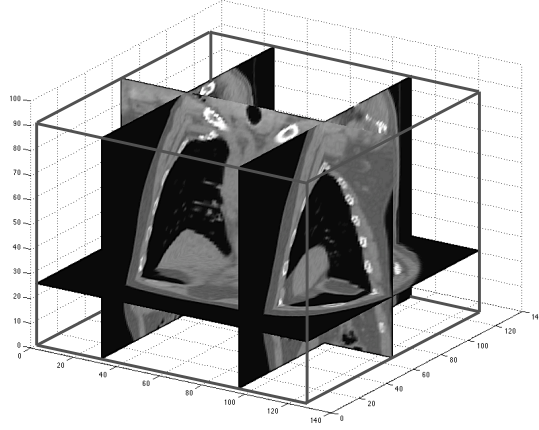
Figure 4.18: Chosen planes to create comparison reference (patient number 13) for diaphragm modelling. Planes from each dataset include an axial, mid-coronal and one-fourth of the sagittal planes from left and right.

evaluation: $w_{int} : 0.1$, $w_{img} : 1$, $w_{con} : 0$ (no external force by user-interface), $\alpha : 1$, $\beta : 0.05$, $w_{line} : 0$ ($\mathbb{EB}$ is a binary image and does not include any line) and $w_{edge} : 1$.

The performance of the proposed algorithm for 3D modelling of the human full diaphragm, presented in section 4.2.3, was evaluated quantitatively by comparing the modelling results with ground truth. To create ground truth, marking all slices that include the diaphragm (roughly 1500 slices) was almost impossible. Instead, to create comparison reference, from each dataset four planes including an axial (chosen in blinded fashion), mid-coronal and one-fourth of the sagittal planes from left and right were chosen for performance assessment (see Figure 4.18 for illustration). On each plane (60 planes in total), first, the diaphragm border was marked manually and then was corrected and localized by the radiologist to obtain reference masks (see top row images in Figure 4.19).

Two metrics were chosen for comparing the modelling results and ground truth, namely mean distance to the closest point ($MDCP$) and Hausdorff Distance (see section 2.5.2.2 for mathematical formulas). These two metrics have been used commonly for assessing the diaphragm border detection [110], top-surface estimation [147] and 3D localization [114].

Regardless of patients' medical history, lungs in test MDCT datasets were exclusively reviewed by the radiologist for abnormalities and diagnosed as follows:

(i) mild emphysema and bronchiectasis (one case)
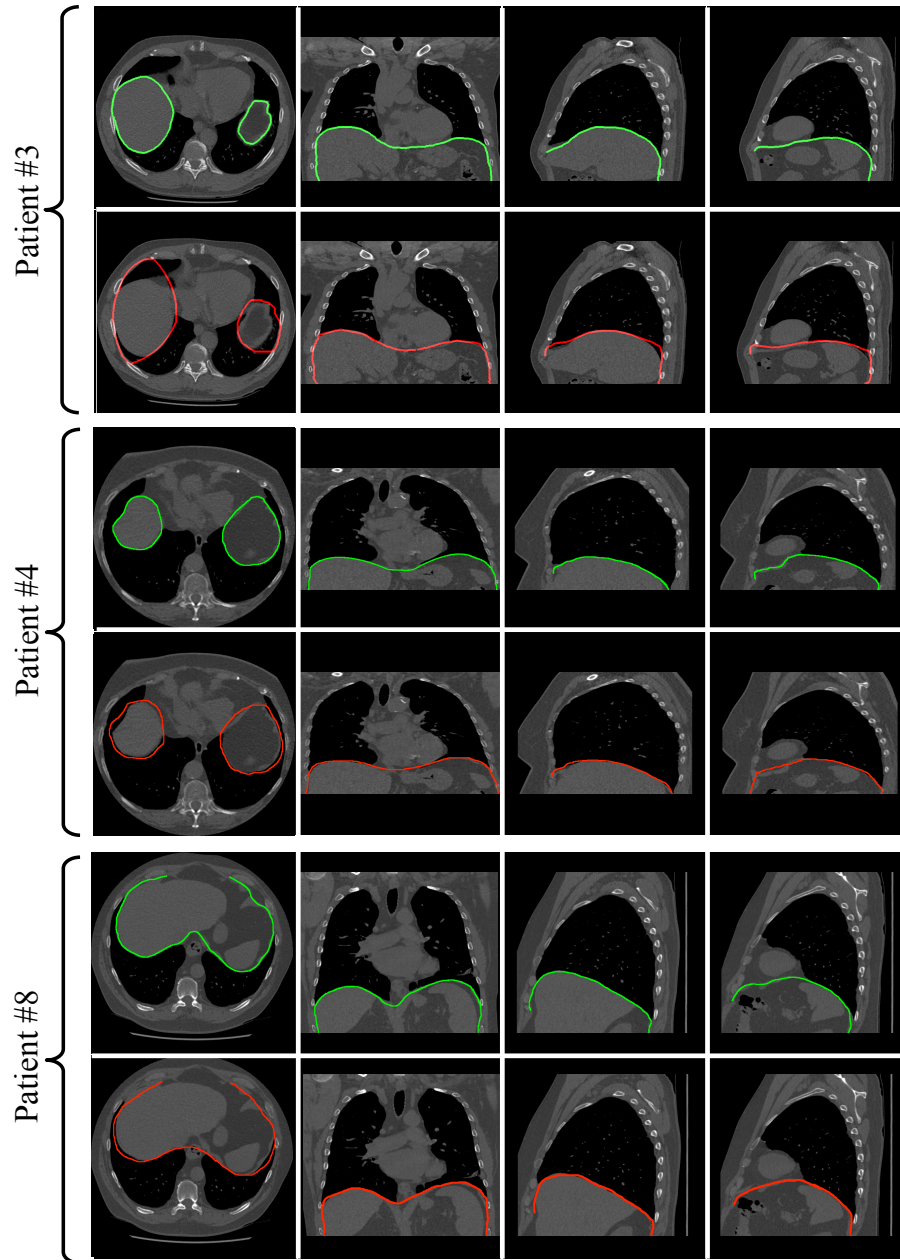
Figure 4.19: In each pair of images, diaphragm ground truth is marked by green lines (top image) and the modelling result is shown by red lines (bottom image). Illustrated images belong to patients number 3, 4 and 8 at axial, mid-coronal and sagittal (one-fourth of planes from left and right) directions.

(ii) multiple lung nodules ranging up to 5 cm in size and probably metastases (one case)

(iii) moderate emphysema (one case)

(iv) severe bronchiectasis with some fibrosis, severe scoliosis (one case)

(v) essentially normal, mild dependent atelectasis (one case)
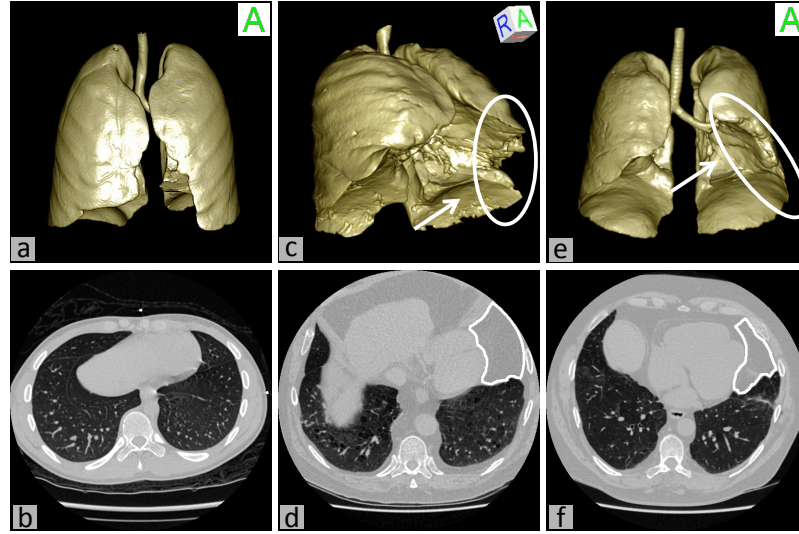
Figure 4.20: (a) and (b) illustrations of normal lungs in 3D and 2D, from a 21 years old patient's dataset (c) and (d) show two cases with enlarged pericardial fat pad in 3D in which lungs abnormal indentation and cut off between the lungs and the diaphragms are marked by arrows and oval respectively (e) and (f) enlarged pericardial fat are marked on 2D slices.

 (vi) essentially normal with several small (about 5 mm) nodules (one case)

 (vii) essentially normal with small calcified nodules (one case)

(viii) normal, however images were taken during expiration (one case)

 (ix) normal (seven cases).

The proposed algorithm failed on two datasets, both with massive fat on the left cardiophrenic angle on top of the diaphragm and next to the heart (clinically known as enlarged pericardial fat pad). These two datasets were excluded from the final reported results. In Figure 4.20 a dataset with normal pericardial fat is shown as well as the datasets with enlarged fat pad (patients number 6 and 12). As marked on Figure 4.20, the enlarged pericardial fat pad pushes a large portion of the left lung and cuts off the lung from the diaphragm. As a result, the lung lower surface does not have normal contact with the diaphragm top surface, which is assumed for diaphragm top boundary estimation.

Also, several experiments confirmed that the performance of the proposed algorithm changes remarkably when the diaphragm top surface is estimated using different methods. It may be inferred that the accuracy of the proposed algorithm is

highly dependent on the lungs' lower surface positions i.e. diaphragm top boundary estimation. The proposed algorithm was tested on the remaining 13 datasets with normal $\mathbb{LDS}$.

To perform evaluation, the diaphragm top boundary was estimated from $\mathbb{LDS}$ using three different methods: linear interpolation and fourth and fifth degree polynomial surfaces. Performance evaluation results are summarized in Table 4.4 and the best results are highlighted.

4.4 Discussion

Qualitative and quantitative evaluations show high similarity between rib reconstruction results and the corresponding reference masks, as well as high similarity to anatomy. As shown in Table 4.2, ribs are reconstructed approximately with 0.94 mm mean distance error and 1.96 mm rms (root mean square) distance error. According to the results, ribs are reconstructed slightly more accurately in the coronal direction than in the axial direction.

According to the qualitative evaluation, shown in Figure 4.17, ribs were reconstructed with 89.85% (on average) similarity to the corresponding datasets. Moreover, from the similarity scores it may be concluded that lower ribs (higher in numbering) were reconstructed more faithfully to anatomy.

Performance of the rib reconstruction algorithm may be improved by transferring the reference axis of the cylindrical coordinate system from the centre of the axial plane to the centre of the rib cage (top view). This modification has been tested manually on some datasets and the results do show improvement in performance. The presented algorithm may be further tested in future using newly released studies on the anatomy of the human ribs i.e. more detailed studies on rib geometry regarding cross-section and length. Moreover the algorithm can inspire researchers interested in reconstructing the ribs in 3D from 2D biplanar images.

Performance of the costal cartilage reconstruction algorithm was evaluated with different criteria. Evaluations show high similarity between reconstruction results and

Table 4.4: Performance evaluation of diaphragm modelling technique, tested on 13 datasets

Evaluation Metric →	Hausdorff distance (mm)			MDCP (mm)		
Method for estimating the diaphragm top surface →	Polynomial surface		Linear interpolation	Polynomial surface		Linear interpolation
Selected slice for evaluation ↓	4th degree	5th degree		4th degree	5th degree	
Axial	**19.78**	22.64	23.68	**6.13**	7.11	6.94
Coronal	**6.93**	8.61	9.36	1.83	**1.76**	1.86
Left sagittal	**9.48**	10.31	10.03	**2.72**	2.77	2.82
Right sagittal	10.24	9.53	**9.16**	3.14	2.81	**2.71**
Average over four slices	**11.61**	12.77	13.06	**3.46**	3.61	3.58

the reference masks, as well as high similarity to anatomy. The proposed algorithm is applicable to MDCTs with varying degrees of costal cartilage calcification.

Based on evaluation results in Table 4.3, the circular cross-section with area twice $\mathbb{M}$ has the highest DSC ($\approx 77.5\%$) and is recommended for costal cartilage 3D reconstruction using the presented algorithm. Also one may conclude that reconstruction with area twice $\mathbb{M}$ (for each of the models) is more similar to the ground truth. According to the results, costal cartilage reconstruction with vertical ellipse cross-section has the lowest DSC (when the cross-section area is assumed to be either equal to or twice $\mathbb{M}$). In other words, when reconstruction is performed in the cylindrical coordinate system, costal cartilage cross-section with vertical ellipse shape has the least similarity to patient's anatomy.

The main sources of the errors may be summarized as follows:

  (i) the reference axis of the cylindrical coordinate system is not adjusted to the centre of the rib cage (top view)

 (ii) ribs lengths and cartilage lengths are not 100% identical to the patient's anatomy, particularly in cases with high degree of cartilage calcification where adjusting ribs lengths and localizing CCJs become challenging tasks

(iii) since the tested area (costal cartilage cross-section on sagittal plane) is very small, even a slight shift in the location of the reconstructed result decreases the accuracy dramatically.

Performance of the reconstruction algorithm may be improved by learning more about human costal cartilage anatomy in terms of length, curvature, cross-sectional model and any possible relation between the geometry of ribs and costal cartilages. Also, more accurate techniques for identifying the degree of costal cartilage calcification and localizing the area where a rib transits to the cartilage i.e. CCJ, may help to improve the result. The proposed algorithm may inspire researchers who are interested in segmenting costal cartilages from other modalities such as MRI [102] and 2D biplanar images.

Diaphragm modelling performance was evaluated with two metrics commonly used for evaluating the diaphragm modelling, namely the Hausdorff distance and

Table 4.5: Standard deviation of the error distances between different test datasets.

| Evaluation Metric → | σ^2 (mm) | |
| | Hausdorff distance | MDCP |
Selected slice for evaluation ↓		
Axial	3.21	2.53
Coronal	1.06	0.98
Left sagittal	1.89	1.46
Right sagittal	2.01	1.58

MDCP. Evaluation shows high similarity between the modelling results and the reference masks with small distance error, provided the lung lower surfaces have normal contact with the diaphragm.

Based on the average Hausdorff distance and *MDCP* in Table 4.4, the presented algorithm does best when the diaphragm top boundary is estimated by a fourth degree polynomial surface and average Hausdorff distance and *MDCP* are only 11.61 mm and 3.46 mm respectively when tested on 52 slices. Therefore, a fourth degree polynomial surface is recommended top boundary estimation from $\mathbb{LDS}$. Error variations between different patients are listed in Table 4.5, when the top boundary is determined by the recommended method.

The algorithm (with either method of top boundary estimation) outperforms the method for diaphragm 3D modelling earlier proposed [115] and a summary of the performance comparison is provided in Table 4.6.

Robustness of the algorithm needs to be improved for datasets with abnormal lower surface position e.g. datasets with enlarged pericardial fat pad or Pneumothorax (collapsed lung). One solution may be to estimate the normal position of the lung lower surfaces before estimating the diaphragm top boundary. Several methods have already been proposed in the literature for robust outlining of the normal lung boundaries with high-density pathologies or significant mis-positioning, which may be leveraged for the purpose.

The proposed algorithm may inspire researchers who are interested in modelling, border detection or motion analysis of the diaphragm from MRI [142], cardiac

Table 4.6: Performance comparison between the proposed algorithm and the method already proposed [115] for modelling the diaphragm in 3D

Comparison Criteria → Diaphragm modelling method ↓	# of patients	Patients' range of age	Slice thickness (mm)	# of evaluated slices	Hausdorff dist. (mm)	MDCP (mm)
Proposed algorithm (method for estimating the diaphragm top surface)						
4th degree polynomial surface	13	18-86	1	52	11.61†	3.46†
5th degree polynomial surface	13	18-86	1	52	12.77†	3.61†
linear interpolation	13	18-86	1	52	13.06†	3.58†
Earlier proposed algorithm [115]	4	2-11	5	73	24.60‡	5.85‡

† Over four slices per dataset, including axial, coronal and two sagittal planes

‡ Over entire diaphragm in 3D

PET images [90], coronary X-ray angiography [110] or 2D projection images of mega-voltage cone beam CT [37].

4.5 Summary

Novel automatic algorithms have been proposed for reconstructing a patient's ribs and costal cartilage and modelling the full diaphragm in 3D from thoracic MDCT datasets. The idea is to computationally reconstruct each rib and costal cartilage cross-section along the estimated centre-line. Estimations are based on the patient's unique anatomy. Latest available anatomical studies have been employed to obtain patient customised, anatomically-faithful reconstruction. The presented technique for diaphragm modelling estimates a 3D boundary for the diaphragm and expands a predefined mesh as 3D active contours towards the boundary. The 3D boundary is determined by the lung lower surfaces and inner surfaces of the lower ribs, spinal column and costal cartilages. Qualitative and quantitative evaluations show high similarity between reconstruction and modelling results using the chosen reference masks, as well as high similarity to anatomy.

Automatic extraction of pleural abnormalities from MDCT images will be dealt with in the next chapter. Techniques to automatically detect calcified pleura in the diaphragmatic area as well as thickened pleura on the costal surfaces from lung MDCT datasets will be presented. Also the experiments to evaluate the performance and accuracy of the technique are provided and their results are discussed.

Chapter 5

Automatic 3D Extraction of Pleural Abnormalities from MDCT Images

Pleural plaques (PPs) and diffuse pleural thickening (DPT) are two main types of non-malignant pleural diseases. Both PPs and DPT affect the outer lining of the pleura and most commonly follow from extensive asbestos exposure over a long period of time. Currently, PPs and DPT are diagnosed non-invasively by subjective investigation of medical images, which is time-consuming and based on subjective judgment.

In this chapter, a fully automatic algorithm for automatic computer aided detection (CADe) of PPs and DPT is presented and tested. The algorithm detects calcified pleura in the diaphragmatic area ($\mathbb{CP}_{diaph}$) and thickened pleura on the costal surfaces ($\mathbb{TP}_{costal}$) from a lung MDCT dataset. This chapter presents comprehensive details of PPs and DPT detection, as well as the testing and evaluation of the algorithm.

Frameworks of the proposed algorithms and technical details of the steps are provided in section 5.1. The algorithm has been tested and evaluated by several experiments and the details are presented in section 5.2. The results of evaluation are discussed thereafter in section 5.3.

5.1 Extraction Framework

A flowchart for automatic PPs and DPT detection in 3D is shown in Figure 5.1. The flowchart includes details of detection, both in the diaphragmatic area and on the pleural costal surfaces. The algorithm is divided into five main parts and as illustrated, separated by dashed lines. Each part of the algorithm consists of different steps and the entire algorithm is summarized as follows:

(i) preliminary segmentations, including:

    (i.i) respiratory organs segmentation, see Figure 5.1b

    (i.ii) chest bone segmentation, see Figure 5.1c

(ii) estimating $\mathbb{InnerLayer}$, see Figure 5.1e

(iii) estimating $\mathbb{OuterLayer}$, including:

    (iii.i) sternum segmentation, see Figure 5.1g

    (iii.ii) vertebral column segmentation, see Figure 5.1f

    (iii.iii) ribs segmentation, see Figure 5.1i

    (iii.iv) detecting and excluding the attached calcified pleura from segmented ribs, see Figure 5.1j

    (iii.v) costal cartilage modelling, see Figure 5.1m

    (iii.vi) $\mathbb{OuterLayer}$ estimation, see Figure 5.1o

(iv) detecting calcified pleura in the diaphragmatic area, including:

    (iv.i) estimating the diaphragm upper surface, see Figure 5.1d

    (iv.ii) extracting calcified pleura in the diaphragmatic area, see Figure 5.1h

(v) extracting PPs and DPT on the pleural costal surfaces, including:

    (v.i) calculating $\overline{\mathbb{D}}$, the mean distance between $\mathbb{InnerLayer}$ and $\mathbb{OuterLayer}$, see Figure 5.1p
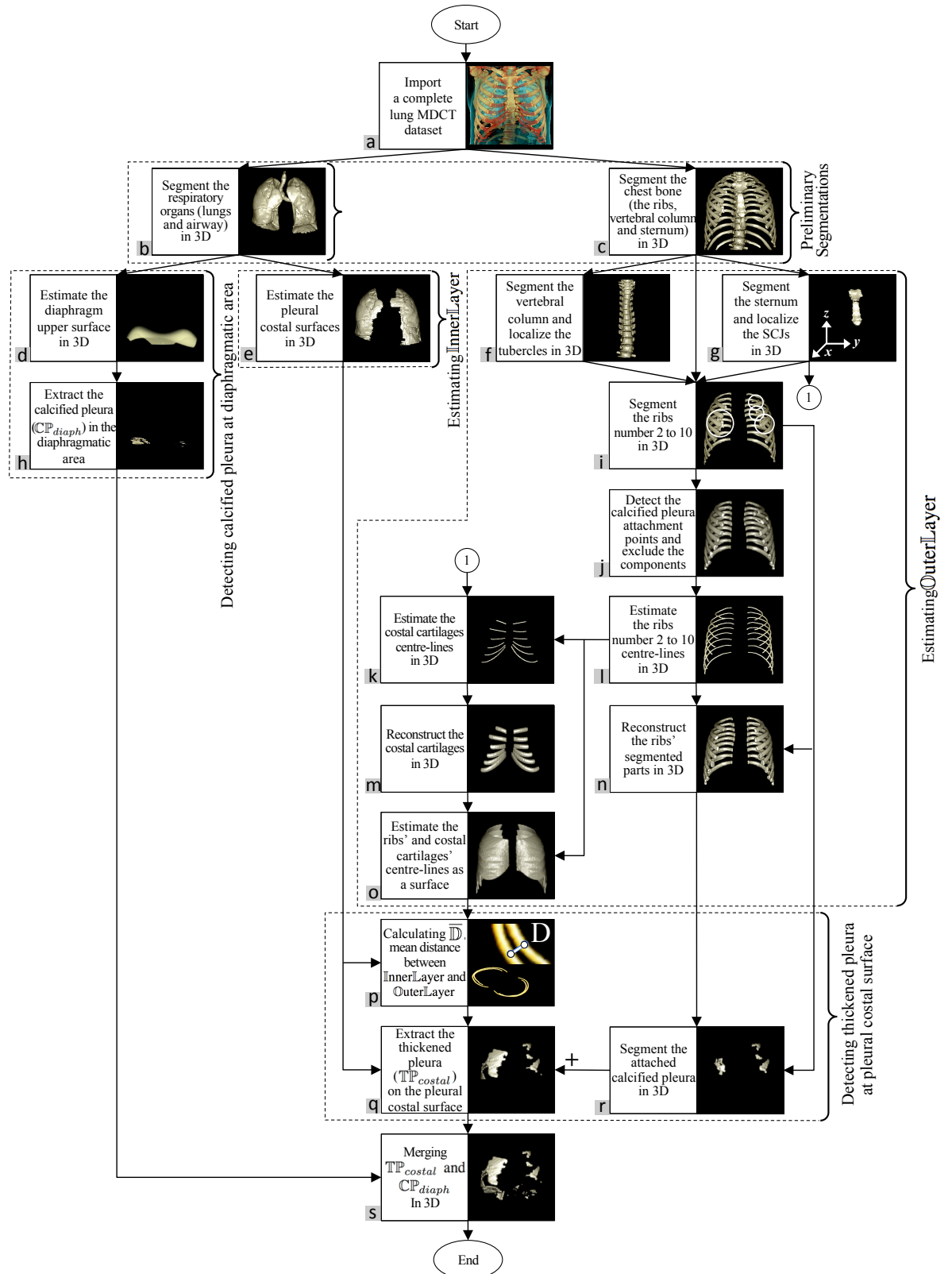
Figure 5.1: Low-level description for detecting calcified and thickened pleura in pleural diaphragmatic and costal surfaces areas from lung MDCT images, dataset belongs to a 79 year old male patient.

(v.ii) extracting thickened pleura on the pleural costal surfaces, see Figure 5.1q.

The following sections provide details of the different parts and steps.

5.1.1   Preliminary Segmentations

Preliminary segmentations include 3D extraction of respiratory organs and chest bone from lung MDCT datasets. Both segmentations are based on the graph cut algorithm and were described in Chapter 3. Based on the experiments and evaluations in sections 3.3.2.1 and 3.3.2.2, 2D graph with 4 - neighbourhood is chosen to build the energy graph for the purpose of graph cut segmentation, for both lung and chest bone extraction. An example of segmented lungs in 3D is in Figure 5.1b, with clearly visible imprints of thickened and calcified pleura on the lungs' outer surface. Examples of segmented ribs, vertebral column and sternum, together with attached calcified pleura to the ribs, are shown in Figure 5.1c.

5.1.2   Detecting Calcified Diaphragmatic Pleura

The top surface of the diaphragm is a common area for involvement of PPs and thickening. The technique presented in Chapter 4 is employed for estimating the upper surface of the diaphragm. As explained in section 4.2.3.1, the diaphragm top surface can be estimated by fitting a surface to the lungs' diaphragmatic surface. Based on testing and evaluations in section 4.3.2.3, estimating the diaphragm upper surface by a fourth degree polynomial surface is recommended and used for detecting calcified pleura in the diaphragmatic area. An example of an estimated diaphragm upper surface in 3D is shown in Figure 5.1d.

By running the graph cut algorithm on MDCT dataset to segment the chest bone (section 5.1.1), some additional objects that are not part of the chest bone, are also segmented. They could be calcified pleura, the patient table, artefacts attached to the patient and occasionally some parts of other organs. Therefore, after ignoring the biggest component of the chest bone in 3D i.e. the ribs, vertebral column, sternum

and possibly the attached clavicle and/or scapula, any other object at a certain vertical distance from the estimated diaphragm upper surface is identified as calcified pleura in the diaphragmatic area ($\mathbb{CP}_{diaph}$ hereafter). In Figure 5.1h, an example of extracted calcified pleura in $\mathbb{CP}_{diaph}$ is shown.

5.1.3   Estimating $\mathbb{InnerLayer}$

Pleural costal surfaces i.e. outer surfaces of the lungs (as shown in Figures 1.1b, c) are estimated in 3D by employing the convex hull algorithm. The technique to estimate the $\mathbb{InnerLayer}$ includes slide by slide subtraction of the dilated convex hull of the segmented lungs from the lung perimeters. The next step is to make a binary matrix of the result in 3D and assign the biggest component as the redundant part. As the final step, the redundancy is removed slide by slide from the perimeters of the segmented lungs. Pseudo code for estimating $\mathbb{InnerLayer}$ in 3D is presented in Appendix F. An example of $\mathbb{InnerSurface}$ (pleural costal surfaces) is shown in Figure 5.1e.

5.1.4   Estimating $\mathbb{OuterLayer}$

$\mathbb{OuterLayer}$ is estimated in 3D as a surface fitted to the centre-lines of the ribs and costal cartilages. To localize the centre-lines of the ribs and costal cartilages, several steps need to be taken as follows:

5.1.4.1   Sternum Segmentation in 3D

As discussed in Chapter 4, to reconstruct the costal cartilage in 3D, which is an essential step for $\mathbb{OuterLayer}$ estimation, localization of the sternocostal joints (SCJs) is needed. On the other hand, localising SCJs in 3D depends on accurate 3D segmentation of the sternum. The algorithm presented in Chapter 3, section 3.2.3.3, is employed to extract the sternum from segmented chest bone as well as SCJs localisation in 3D. An example of the segmented sternum is shown in Figure 5.1g.

5.1.4.2 Vertebral Column Segmentation in 3D

The vertebral column can be isolated in 3D from the segmented chest bone by the following steps:

(i) start from mid-coronal plane and ignore half-front of the segmented chest bone

(ii) localize the bone cross-sections ($\mathbb{N}$ objects) in mid-coronal plane

(iii) calculate $\mathbb{A}$, mean area of $\mathbb{N}$ objects

(iv) remove $\mathbb{N}$ objects while tracing them backward in coronal direction in 3D

(v) stop the tracing procedure for each object by applying a size constraint i.e. when the area of a traced object is larger than twice $\mathbb{A}$.

However, if the patient dataset includes calcified PP attached to a rib or series of ribs, it could lead to mis-localization of the tubercles, sometimes far from their correct location. Therefore, to isolate the vertebral column in 3D and localize the tubercles, a different approach is taken: the tracing procedure starts from the middle of the vertebral column (see Appendix G for steps to find the vertebral column mid-sagittal). Tracing continues in the sagittal direction to the right and left. The procedure stops when the area of the traced object on a sagittal plane is smaller than twice $\mathbb{A}$ and restarts, until all tubercles are localized. An example of the isolated vertebral column in 3D is shown in Figure 5.1f.

5.1.4.3 Ribs Segmentation in 3D

Ribs are segmented in 3D by subtracting the sternum and the vertebral column from the chest bone and may include calcified thickened pleura and/or calcified costal cartilage. Mis-segmented parts are identified and separated in section 5.1.4.4. An example of segmented rib numbers 2 to 10 is shown in Figure 5.1i and attached calcified thickened pleura are marked by white circles. Rib numbers 1, 11 and 12 have been excluded from $\mathbb{O}$uter$\mathbb{L}$ayer estimation as PPs and DPT occur over the fifth to ninth rib and rarely extend beyond them [85].

5.1.4.4   Detection and Segmentation of Attached Calcified Pleura

Calcified pleura attached to a rib or series of ribs decreases the accuracy of PPs and DPT detection and need to be separated. Following is the step by step technique to separate the attached calcified pleura:

(i) The first step is to specify the location where the rib is attached to the calcified pleura and cut it. This is achieved by tracing and analysing the rib cross-section along its length. The tracing procedure is in cylindrical coordinate system, whose origin is at the centre of the image (see Figure 1.1c) and starts from the two endpoints i.e. tubercle and costochondral joint (CCJ). The rib's centre-line is recorded while tracing is performed. The direction of tracing is shown with double curved arrows in Figure 1.1d. Tracing stops when the cross-section area is larger than twice $\mathbb{A}$ (mean area of all ribs' cross-sections in mid-coronal plane). When attachment points are localised, the rib is cut (see Figure 1.1e for illustration and Figure 5.1j for an example in 3D).

(ii) The second step is to reconstruct the rib in 3D where it is cut. The method presented in Chapter 4 for patient-customised rib reconstruction, is used to reconstruct the cut rib. The technique uses the patient's unique anatomy to model the entire rib in 100 sections from the tubercle to CCJ in 3D. Parts of the technique are adopted here to estimate the partially cut rib in the following steps:

   (ii.i) estimate the cut rib centre-line by fitting smoothing splines to the already recorded centre-line (see Figure 5.1l for an example in 3D)

   (ii.ii) adjust the rib lengths and localize the correct positions of CCJs in 3D

   (ii.iii) estimate Θ, the angle between horizontal plane and a flat surface, fitted to the centre-line

   (ii.iv) calculate δ, the number of sections needed to reconstruct the cut piece (see Appendix H)

   (ii.v) customize shape and size of the δ cross-sections

(ii.vi) model the cut rib by applying δ customized cross-sections to the estimated centre-line.

An illustration of a cut and reconstructed rib in 2D is shown in Figure 1.1f. An example of reconstructed ribs that are free from attached calcified pleura is shown in Figure 5.1n.

(iii) As the third step, if a reconstructed rib (as shown in Figure 1.1f) is subtracted from the rib, the attached calcified pleura is accurately extracted (see Figure 1.1g for illustration and Figure 5.1r for an example in 3D).

5.1.4.5 Costal Cartilage Modelling in 3D

As discussed in Chapter 4, due to the natural density of costal cartilage which is close to the adjacent soft tissue e.g. muscles and their considerably varying degree of calcification between individuals, direct segmentation of costal cartilage is a challenging task. Therefore, instead of segmentation, this organ needs to be estimated and modelled in 3D. The technique presented in Chapter 4 is employed to reconstruct the costal cartilage in 3D based on the patient's anatomy. An example of reconstructed costal cartilage is shown in Figure 5.1m.

5.1.4.6 OuterLayer Estimation in 3D

The spaces between the ribs' and costal cartilages' centre-lines are estimated in 3D as a surface by employing a thin plate spline technique. Thin plate is considered as a surface. During surface fitting, for each pair of (x,y) coordinates, not more than one z coordinate should exist. Accordingly, ribs' and costal cartilages' centre-lines are transformed to the Cartesian coordinate system, estimated by a thin plate, and retransformed to cylindrical coordinate system. In Figure 5.1o spaces between centre-lines in Figures 5.1k and 5.1l are filled and estimated in 3D.

5.1.5 Extracting PPs and DPT on Pleural Costal Surfaces

For automatic extraction of thickened pleura on the pleural costal surfaces, the distances between $\mathbb{O}\text{uter}\mathbb{L}\text{ayer}$ and $\mathbb{I}\text{nner}\mathbb{L}\text{ayer}$ (as shown in Figure 5.1p for a certain degree and certain slide number) are investigated in cylindrical coordinate system. Locations of thickened pleura are determined in 3D in two steps:

(i) $\overline{\overline{\mathbb{D}}}$ (patient's mean distance between pleural costal surfaces and rib centre-lines, see Figure 1.1b for illustration of $\mathbb{D}$) is calculated

(ii) locations in 3D where the distance between the estimated surface ($\mathbb{O}\text{uter}\mathbb{L}\text{ayer}$) and costal surfaces of the pleura ($\mathbb{I}\text{nner}\mathbb{L}\text{ayer}$) are relatively larger than $\overline{\overline{\mathbb{D}}}$, are identified as thickened pleura on the pleural costal surfaces ($\mathbb{TP}_{costal}$).

The MDCT dataset is modelled in cylindrical coordinate system and the following notations (as shown in Figure 1.1c) are used:

n: number of slides per dataset

i: slide number

$R_{i\theta}$: rib centre-line at θ degree

$P_{i\theta}$: pleural costal surfaces at θ degree

$dR_{i\theta}$: distance between $R_{i\theta}$ and reference axis

$dP_{i\theta}$: distance between $P_{i\theta}$ and reference axis

$D_{i\theta}$: distance between $R_{i\theta}$ and $P_{i\theta}$

Then:

$$D_{i\theta} = dR_{i\theta} - dP_{i\theta} \tag{5.1}$$

$$\overline{\overline{\mathbb{D}}} = \left\langle \sum_{i=1}^{n} \sum_{\theta=1}^{360} \{D_{i\theta}, \ if \ (\exists! \ R_{i\theta} \ \& \ \exists! \ P_{i\theta})\} \right\rangle \tag{5.2}$$

and

$$\mathbb{TP}_{costal} = \{ \ \mathbb{D}_{I\Theta}, I = 1, 2, ..., n \ , \ \Theta = 1, 2, ..., 360 \ \} \tag{5.3}$$

if

$$\forall \ D_{i\theta} \in \mathbb{D}_{I\Theta} : w . \overline{\overline{\mathbb{D}}} < D_{i\theta} \tag{5.4}$$

where w is a weighting coefficient to control how far from the rib centre-lines is to be considered as abnormal.

An example of detected and extracted $\mathbb{TP}_{costal}$ in 3D is shown in Figure 5.1q.

5.1.6   Detecting Abnormalities on the Lung Surfaces

As the final step, $\mathbb{TP}_{costal}$ and $\mathbb{CP}_{diaph}$ are merged to determine the patient's ARPD as a single volume object. Merged thickened pleura on the pleural costal surfaces and calcified pleura in the diaphragmatic area as a 3D object is shown in Figure 5.1s.

5.2   Performance Evaluation

To measure the performance and accuracy, the proposed techniques for extracting calcified pleura in the diaphragmatic area ($\mathbb{CP}_{diaph}$) and thickened pleura on the pleural costal surface ($\mathbb{TP}_{costal}$), were tested separately. The algorithms were run on a set of MDCT datasets and the results were evaluated using different criteria. The following subsections provide details about the datasets used, experiments and evaluations.

5.2.1   Material

The algorithms were tested on 20 complete lung MDCT datasets of patients diagnosed with existing PPs and/or DPT. All datasets share the same technical description provided in section 2.5.2.1 and Table 2.1. Demographic data of MDCT datasets, used for evaluating the reconstruction and modelling algorithms, are summarised in Table 5.1.

5.2.2   Experiments and Results

The techniques for $\mathbb{CP}_{diaph}$ and $\mathbb{TP}_{costal}$ extraction were tested separately to measure the accuracy and performance. The result of each experiment was compared with

Table 5.1: Demographic data of MDCT studies, used for testing and evaluating $\mathbb{CP}_{diaph}$ and $\mathbb{TP}_{costal}$ extraction techniques.

MDCT Dataset	
Number of studies	20
Number of slices (per dataset)	452 (on average)
Patient	
Sex	
Male	100%
Female	0%
Age	
Mean	74
Range	63 - 83

corresponding ground truth using different criteria. Selected images for evaluation were marked and corrected by an experienced radiologist [1] to obtain reference masks. The following sub-sections provide details of the evaluations.

5.2.2.1 Experiments on $\mathbb{CP}_{diaph}$ Extraction

The performance of the proposed algorithm for segmenting calcified pleura in the diaphragmatic area, presented in section 5.1.2, was evaluated quantitatively. In order to include large portions of patients' diaphragms, the mean of every five slides, starting from diaphragm top dome, were computed and considered for ground truth. All slides between the diaphragm top dome and lower dome and the following 25 slides (see Figure 5.2b for illustration) were included. On each plane (198 planes in total), borders of calcified pleura were marked manually and an experienced radiologist reviewed and confirmed the marked borders.

As explained in section 5.1.2, a defined distance from the estimated diaphragm upper surface is considered for detection of calcified pleura. Vertical distance was assumed as a range between 1 and 20 pixels. The graph in Figure 5.3 shows how performance changes when the vertical distance is changed. Moreover, the graph in Figure 5.4 illustrates the *MDCP* behaviour based on vertical distance changes.

---

[1]Medical Imaging Department, Prince of Wales Hospital, Sydney, NSW, Australia.
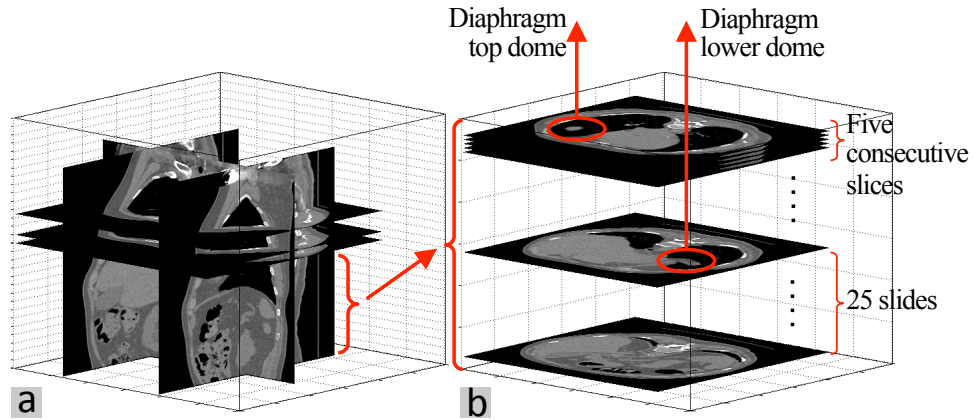
Figure 5.2: (a) Chosen planes to create ground truth of $\mathbb{TP}_{costal}$ and (b) chosen planes to create ground truth of $\mathbb{CP}_{diaph}$ (patient number 1).
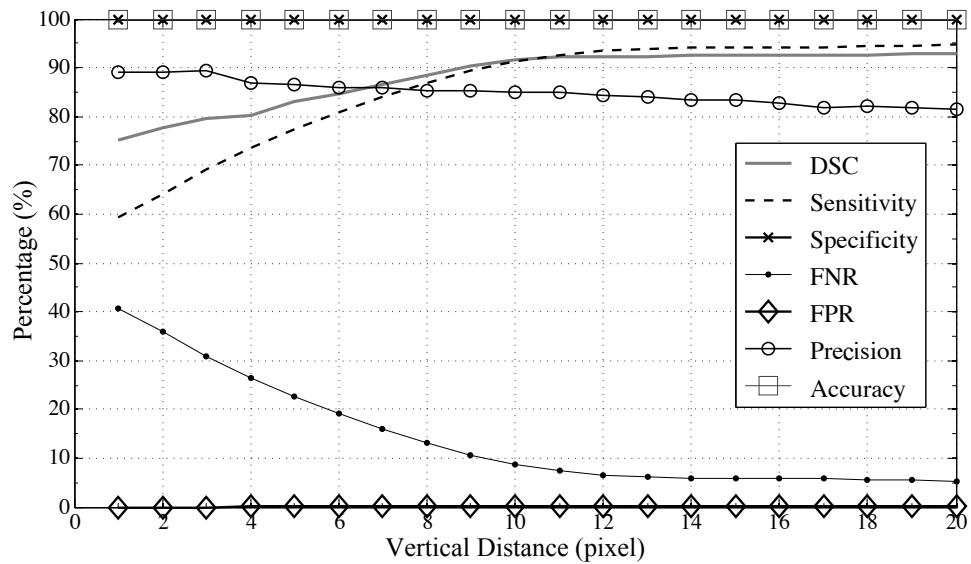
Figure 5.3: Performance evaluation for detecting $\mathbb{CP}_{diaph}$.

5.2.2.2 Experiments on $\mathbb{TP}_{costal}$ Extraction

The proposed algorithm for extracting thickened pleura on the pleural costal surface was evaluated. To create ground truth and comparison reference, from each MDCT dataset six planes including three axial (chosen in blinded fashion), mid-coronal and one-fourth of the sagittal planes from left and right were chosen for performance assessment (see Figure 5.2a for illustration). On each plane (120 planes in total), the border of thickened pleura was marked manually by an experienced radiologist to obtain reference masks.

As illustrated in Figure 5.5, $\overline{\mathbb{D}}$ is calculated for each patient individually based on
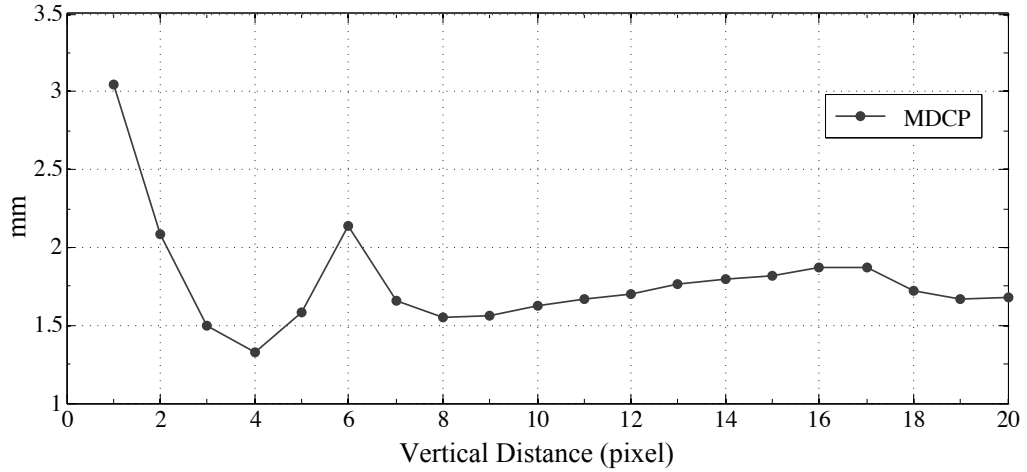
Figure 5.4: *MDCP* between detected $\mathbb{CP}_{diaph}$ and corresponding ground truth.
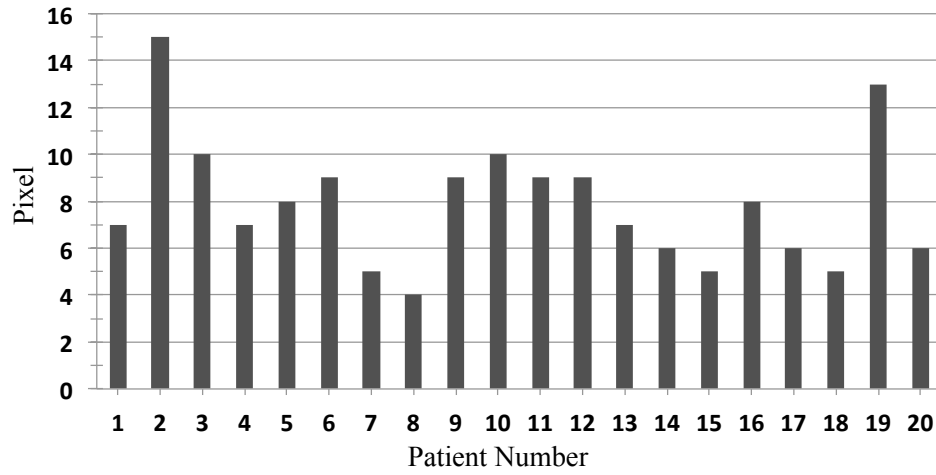
Figure 5.5: $\overline{\overline{\mathbb{D}}}$, computed for each patient individually, based on Equation (5.2).

Equation (5.2). The diversity in $\overline{\overline{\mathbb{D}}}$ values may be related to differences in patients' natural anatomy and also fat mass between rib surfaces and pleural costal surfaces.

In addition, the parameter w in Equation (5.4) was set to three values: 1.2, 1.5 and 2. Detected $\mathbb{TP}_{costal}$ in all chosen planes (in different directions) were compared with their corresponding ground truths. The evaluation results are listed in Table 5.2 and the best performance in each group is highlighted.

5.2.2.3 Volumetric Measurments

Detected $\mathbb{CP}_{diaph}$ and $\mathbb{TP}_{costal}$ were analysed in term of volume. The bar chart in Figure 5.6 shows the rate (percentage) of detected pixels to the total volume of the lungs for each patient individually and the mean, maximum and minimum of

Table 5.2: Performance Evaluation for Detecting $\mathbb{TP}_{costal}$ in 20 MDCT datasets.

Detecting Area →		Pleural costal surfaces								
Performance	Plane Direction →	Axial			Coronal			Sagittal		
Metric ↓	w in Equ. 5.4 →	1.2	1.5	2	1.2	1.5	2	1.2	1.5	2
DSC (%)		**80.13**	67.51	61.95	**74.35**	58.75	18.15	**79.26**	64.74	27.53
FNR (%)		**17.38**	18.83	45.40	**25.08**	43.17	86.08	**22.21**	43.04	79.70
FPR (%)		0.47	1.18	**0.43**	0.20	0.11	**0.04**	0.14	0.13	**0.05**
Sensitivity (%)		**82.62**	81.17	54.60	**74.92**	56.83	13.92	**77.79**	56.96	20.30
Specificity (%)		99.53	98.82	**99.57**	99.80	99.89	**99.96**	99.86	99.87	**99.95**
Precision (%)		**77.78**	57.79	71.58	**75.19**	66.39	43.75	**82.78**	79.69	71.99
Accuracy (%)		**99.20**	98.47	98.69	99.56	99.56	**99.65**	**99.61**	99.42	99.29
MDCP (mm)		**0.13**	0.44	1.55	**0.14**	0.55	4.55	**0.24**	0.66	1.79
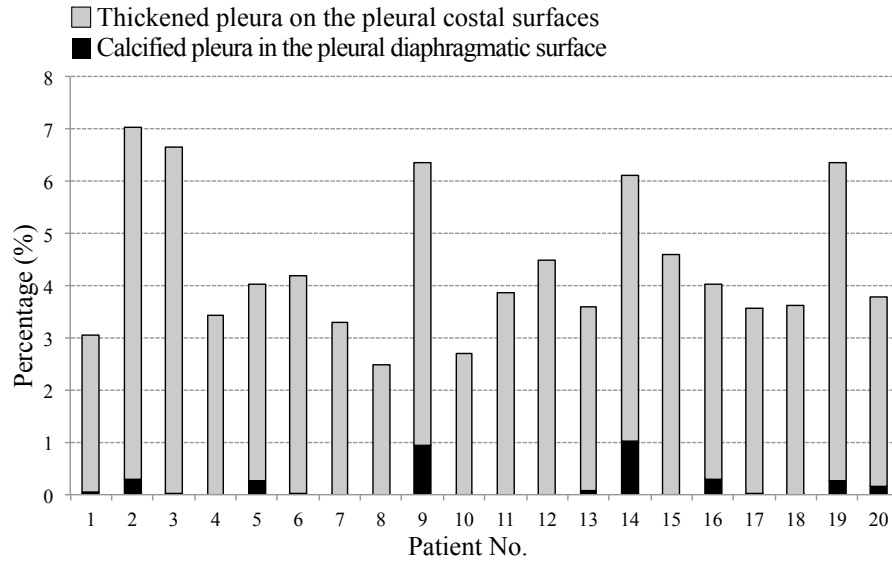
Figure 5.6: Bar chart to illustrate the portions of each patient's lung volume, affected by $\mathbb{CP}_{diaph}$ and $\mathbb{TP}_{costal}$.

Table 5.3: Mean, maximum and minimum percentage of patients' lung volume, affected by $\mathbb{CP}_{diaph}$ and $\mathbb{TP}_{costal}$.

Detected area $\rightarrow$	$\mathbb{CP}_{diaph}$	$\mathbb{TP}_{costal}$
Volume of affected area (%) $\downarrow$		
Mean	0.14	4.23
Minimum	0	2.49
Maximum	0.94	6.73

percentages are provided in Table 5.3. Total lung volume is assumed to be the volume of segmented lungs plus the volumes of detected $\mathbb{CP}_{diaph}$ and $\mathbb{TP}_{costal}$.

5.3   Discussion

According to the results achieved and the graph in Figure 5.3, *Accuracy* and *Specificity* of the $\mathbb{CP}_{diaph}$ detection algorithm are almost 100% and do not change when vertical distance changes. *FPR* being complementary to *Specificity*, is not affected by vertical distance change. *Precision* steadily decreases with change in vertical distance. Regarding *DSC*, *Sensitivity* and *FNR* metrics, the algorithm reaches its highest performance and plateaus when the vertical distance is larger than 12 pixels. It may be interpreted that 12 pixels' distance not only covers the calcified pleura but also

Table 5.4: Performance evaluation for detecting $\mathbb{CP}_{diaph}$ in 20 MDCT datasets, when vertical distance from the estimated diaphragm upper surface is assumed to be 20 pixels.

Detecting Area $\rightarrow$ Performance Metric $\downarrow$	Lung Diaphragmatic Area
DSC (%)	92.84
$Sensitivity$ (%)	94.72
$Specificity$ (%)	99.99
FNR (%)	5.28
FPR (%)	0.01
$Precision$ (%)	81.58
$Accuracy$ (%)	99.98
$MDCP$ (mm)	1.68
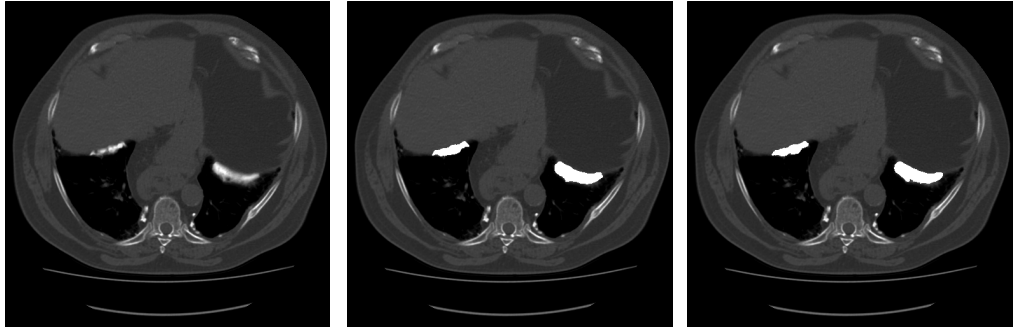
Figure 5.7: From left to right: an example of MDCT image in the diaphragmatic area in axial direction, ground truth and result of automatic $\mathbb{CP}_{diaph}$ detection.

the error in diaphragm upper surface estimation. Further, according to the graph in Figure 5.4, $MDCP$ significantly drops when the vertical distance changes from 1 to 4 pixels and after a local peak at 6 pixels, it becomes almost stable.

Therefore, high performance is achieved in $\mathbb{CP}_{diaph}$ detection when vertical distance from the estimated diaphragm upper surface is assumed to be at least 12 pixels (but distance exceeding 20 pixels is not recommended). In Table 5.4, the performance metrics are shown, when vertical distance is assumed to be 20 pixels, and Figure 5.7 provides an example of $\mathbb{CP}_{diaph}$ detection result and corresponding ground truth.

Based on the experiments on $\mathbb{TP}_{costal}$ detection and Table 5.2, most metrics attain their best value when w is 1.2. Accuracy is very high for all values and their

differences are negligible. *FPR* and *Specificity* (which is associated with *FPR*) have the lowest rate when w is equal to 2. This may be explained by the fact that when w is larger, a smaller portion of space between $\mathbb{O}$uter$\mathbb{L}$ayer and $\mathbb{I}$nner$\mathbb{L}$ayer is considered for $\mathbb{TP}_{costal}$ detection, and a smaller number of pixels may be labelled as positive, which reduces the *FPR* also. Thickened pleura in some test datasets were very small and sometimes less than 100 pixels. Therefore, missing only a small number of pixels in such cases and also approximations adopted in employed methodologies, led to a lower *Sensitivity* of 82%, and associated *FNR* of 17%.

It may be concluded that high performance is achieved when w is equal to 1.2 and is recommended when the proposed algorithm is used for $\mathbb{TP}_{costal}$ detection. Examples of $\mathbb{TP}_{costal}$ detection results in different directions and corresponding ground truths are shown in Figure 5.8.

To sum up, evaluation indicates good accuracy of the algorithm for detection, with higher accuracy in the diaphragmatic areas. As PPs and DPT present as narrow areas on MDCT images, it is likely that the marked ground truth may not be very accurate due to radiologist fallibility. To perform fair evaluation, two other methods may be used to obtain ground truth: marking of the MDCT images by different radiologists, or multiple markings by the same radiologist at different times.

5.4   Summary

A novel algorithm has been proposed for fully automatic 3D detection of calcified and thickened pleura in the pleural diaphragmatic and costal surface areas respectively, from lung MDCT datasets. Calcified pleura in the diaphragmatic area are identified as parts of the patient's dataset, located at a certain vertical distance of the patient's estimated diaphragm and with intensity near to the bone intensity. To localize the thickened pleura on the costal surface, the distance between the pleural costal surface and a surface fitted to the ribs' centre-lines is measured in 3D and $\overline{\mathbb{D}}$, the mean distance, is computed. Any space between the two surfaces whose width exceeds $\overline{\mathbb{D}}$ is identified as detected thickened pleura. Removing the calcified pleura attached to the rib(s) before measuring $\overline{\mathbb{D}}$, improves the algorithm precision. The proposed algorithm
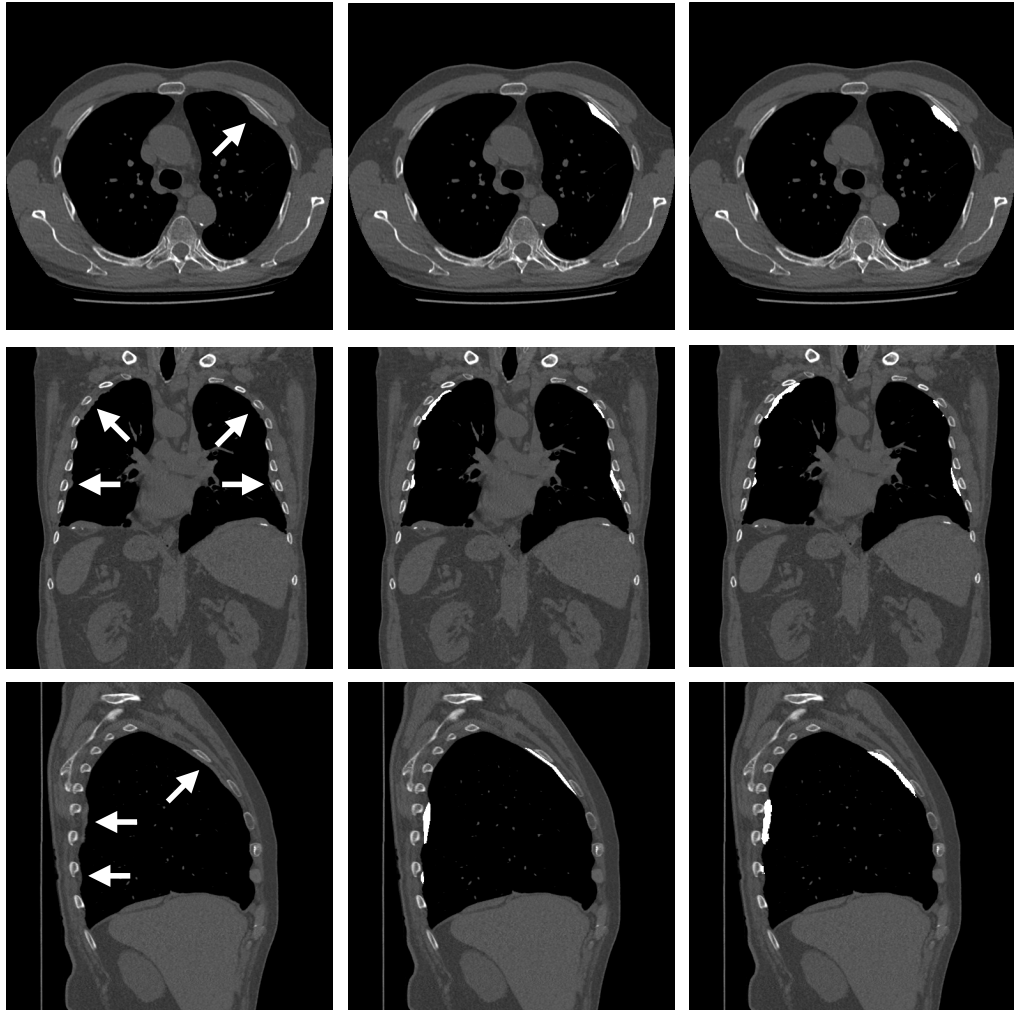
Figure 5.8: From left to right: examples of MDCT images in different directions (axial, coronal and sagittal), corresponding ground truth and result of automatic $\mathbb{TP}_{costal}$ extraction.

was tested on 20 datasets from patients diagnosed with existing PPs and/or DPT. The results of the automatic algorithm were compared with the ground truth using several metrics, and evaluation demonstrates good accuracy of the algorithm for ARPD detection in 3D.

Chapter 6

Conclusion

Pleural plaques (PPs) and diffuse pleural thickening (DPT) are very common asbestos related pleural diseases (ARPD) that are directly linked to asbestos exposure and develop within decades after inhalation of asbestos dust [13, 54, 112]. They are benign conditions that have pleural involvement and thickening. PPs are defined as localised pleural thickening, induced by asbestos, while DPT refers to more generalised pleural thickening [60, 85]. PPs and DPT occur on the pleura and may eventually become calcified. The diaphragm is another potential organ for PP involvement [22, 85, 95].

Medical imaging is necessary for diagnosis of both DPT and PPs as they show no symptoms and may only manifest as breathlessness and chest pain [95]. Therefore both DPT and PPs cannot be detected clinically, and can only be identified non-invasively using medical imaging techniques. Computed tomography (CT) is the preferred imaging modality because it can detect small calcified plaques, and non-calcified plaques/regions of mild DPT that are difficult to appreciate on chest x-ray (CXR) [119]. Currently, multi-detector CT (MDCT) imaging technology is used for DPT and PP detection in high-technology hospitals in Australia.

As far as is known, not many techniques and works on automatic detection of PPs and DPT from medical images have been reported. More specifically, detection of thickened pleura in the diaphragmatic area has not been reported in the literature to date and the limited number of techniques proposed [30, 34, 32, 117] suffer from potential inaccuracies and limitations. Therefore, there is a need for accurate methods

to detect PPs and DPT on the pleural costal surface and in the diaphragmatic area.

6.1   Thesis Summary

A fully automatic technique for 3D extraction of PPs and DPT from lung MDCT images has been presented in this thesis. The proposed algorithm includes detection of calcified pleura in the diaphragmatic area and thickened pleura on the pleural costal surface. Calcified pleura in the diaphragmatic area are identified as parts of the patient's dataset that are located at a certain vertical distance of the patient's estimated diaphragm and with intensity near to that of bone. To localize the thickened pleura on the costal surface area, the distance between the pleural costal surface and a surface fitted to the centre-lines of ribs is measured in 3D and $\overline{\overline{\mathbb{D}}}$, the mean distance, is computed. Any space between the two surfaces whose width exceeds $\overline{\overline{\mathbb{D}}}$ is identified as thickened pleura. Removing the calcified pleura attached to the rib(s) before measuring $\overline{\overline{\mathbb{D}}}$ improves the algorithm precision. The presented algorithm may be divided into five main parts and each part consists of different steps, summarized as follows:

(i) preliminary segmentations, including:

    (i.i) respiratory organs segmentation

    (i.ii) chest bone segmentation

(ii) estimating pleural costal surfaces in 3D as $\mathbb{I}$nner$\mathbb{L}$ayer

(iii) estimating a surface fitted to the centrelines of the ribs and costal cartilages as $\mathbb{O}$uter$\mathbb{L}$ayer, including:

    (iii.i) sternum segmentation

    (iii.ii) vertebral column segmentation

    (iii.iii) ribs segmentation

    (iii.iv) detecting and excluding the attached calcified pleura from segmented ribs

(iii.v) costal cartilage modelling

(iii.vi) $\mathbb{O}$uter$\mathbb{L}$ayer estimation

(iv) detecting calcified pleura in the diaphragmatic area, including:

(iv.i) estimating the diaphragm upper surface

(iv.ii) investigating a certain vertical distance of the estimated surface for extracting existing calcified pleura.

(v) extracting PPs and DPT on the pleural costal surfaces, including:

(v.i) calculating $\overline{\overline{\mathbb{D}}}$, the mean distance between $\mathbb{I}$nner$\mathbb{L}$ayer and $\mathbb{O}$uter$\mathbb{L}$ayer

(v.ii) identifying the locations in 3D where the distance between the layers are relatively larger than $\overline{\overline{\mathbb{D}}}$ as thickened pleura.

The proposed algorithm was tested on 20 MDCT datasets from patients diagnosed with existing PPs and/or DPT. The results of the automatic algorithm were compared with the ground truth using several metrics and evaluation indicates good accuracy of the algorithm.

6.2 Contributions

By accomplishing the goal of thickened pleura detection, this thesis contributes to two important fields, namely medical image analysis and medicine.

6.2.1 Contributions to Medical Image Analysis

The main contributions to medical image analysis may be summarised as follows:

(i) besides a patient's lung features, using other organs for the purpose of referencing and landmarking. The distance between rib and costal cartilage centre-lines and pleural surface is measured and analysed to identify the pleural thickening in 3D

(ii) estimating patient's fat thickness between the rib surface and pleura (usually very thin layer) and excluding it from detected areas to identify the thickened pleura

(iii) distinguishing attached calcified pleura to the rib(s) and separating it in 3D

(iv) detecting the calcified pleura on the lung diaphragmatic surfaces for the first time.

6.2.2   Contributions to Medicine

(i) fast detection of PPs and DPT in 3D that saves time in practice

(ii) possibility of pleural plaque detection of all sizes which is important in medicine as a tiny plaque signifies the same risk for more sinister complications of asbestos exposure as do extensive plaques

(iii) ability to screen patient's chest CT scans, obtained for other reasons, to detect PPs and DPT, which may have a significant impact on managing the patient risks

(iv) accurate measurement of the degree and area of pleural thickening to detect any changes over time. This is important in medicine, as mesothelioma, a dreaded complication of asbestos exposure, usually appears as an area of pleural thickening in the early stages. Screening changes helps a radiologist to assess the risk of the new regions, being a precursor of mesothelioma.

6.3   Limitations and Future Work

The presented technique in this thesis has been successful in developing an automatic algorithm for 3D extraction of PPs and DPT from lung MDCT images. However, the limitations may be investigated to identify opportunities for further research. The following suggestions for further work may be made:

(i) adjust the reference axis of cylindrical coordinate system to the centre of the rib cage and check whether the accuracy increases

(ii) create more valid ground truth, i.e. marked by several radiologists for the purpose of further evaluation and to check the source of errors

(iii) test the presented algorithm on more datasets with a variety of lung diseases and pathologies to investigate the algorithm robustness

(iv) design a program to measure the disease progress in follow up check-ups

(v) design a program to analysis the link between applied treatment and rate of disease progress

(vi) design an algorithm to categorise the segmented thickened pleura into PPs or DPT, based on characteristics

(vii) extend the presented method and modify it to detect pleural thickening in other modalities such as chest X-ray

(viii) test the presented algorithm on datasets taken on different machines and with different parameter settings.

6.4 Concluding Remarks

Pleural plaque detection from a CT dataset is a challenging task. This thesis has presented a technique for 3D detection of calcified pleura in the diaphragmatic area and thickened pleura on the costal surfaces from MDCT images. The proposed algorithms allow accurate and fast detection of thickened pleura that is beneficial in medicine. Although the presented algorithm was designed for MDCT datasets, it might inspire thickened pleura detection in other imaging modalities.

Bibliography

[1] Aquilion computed tomography scanner, toshiba america medical systems @ONLINE http://medical.toshiba.com/products/ct/index.php. [accessed: 25.april.2015].

[2] Asbestos: Elimination of asbestos-related diseases @ONLINE url:http://www.who.int/mediacentre/factsheets/fs343/en/ [accessed 26.dec.2014]. WHO fact sheet number 343.

[3] Asbestos information @ONLINE url:https://asbestossafety.gov.au/ asbestos-information [accessed 26.dec.2014]. Australian Government, Asbestos Safety and Eradication Agency.

[4] Mdct.net's, guide to technology and protocols @ONLINE http://www.mdct.net/eng/infoprotocols/mdcttechnology/ [accessed 02.april.2015]. MDCT technology.

[5] Osirix imaging software @ONLINE http://www.osirix-viewer.com/ [accessed 02.april.2015]. Advanced open-source PACS workstation DICOM viewer.

[6] Modeling costal cartilage using local material properties with consideration for gross heterogeneities. *Journal of Biomechanics*, 44(5):910 – 916, 2011.

[7] Parietal pleura @ONLINE url:http://www.knowyourbody.net/parietal-pleura.html. [accessed: 20.jan.2015], 2015.

[8] A.S. Afroz. An alternative approach of evaluating dice similarity index for pre-segmented blood vessels. 2014.

[9] A.M. Ali and A.A. Farag. Automatic lung segmentation of volumetric low-dose ct scans using graph cuts. In *Proceedings of the 4th International Symposium on Advances in Visual Computing*, ISVC '08, pages 258–267, Berlin, Heidelberg, 2008. Springer-Verlag.

[10] A.M. Ali and A.A. Farag. A novel framework for n-d multimodal image segmentation using graph cuts. In *Image Processing, 2008. ICIP 2008. 15th IEEE International Conference on*, pages 729–732, Oct 2008.

[11] Anatomography. Bodyparts3d, copyright: The database center for life science licensed under cc attribution-share alike 2.1 japan @ONLINE http://commons.wikimedia.org/wiki/file:cervical vertebrae laterla2.png. [accessed: 25.april.2015].

[12] Anatomography. Bodyparts3d, copyright the database center for life science licensed under cc attribution-share alike 2.1 japan @ONLINE http://commons.wikimedia.org/wiki/file:thoracic vertebrae back3.png. [accessed: 25.april.2015].

[13] V.C. Antao, T.C. Larson, and D.K. Horton. Libby vermiculite exposure and risk of developing asbestos-related lung and pleural diseases. *Current Opinion in Pulmonary Medicine*, 18(2):161–167, 2012.

[14] S.G. Armato and W.F. Sensakovic. Automated lung segmentation for thoracic ct: Impact on computer-aided diagnosis1. *Academic Radiology*, 11(9):1011 – 1021, 2004.

[15] W. Bai, W. Shi, C. Ledig, and D. Rueckert. Multi-atlas segmentation with augmented features for cardiac mr images. *Medical Image Analysis*, 19(1):98 – 109, 2015.

[16] K.G. Baum, E. Schreyer, S. Totterman, J. Farber, J. Tamez-Pena, and P. Gonzalez. Application of the dice similarity coefficient (dsc) for failure detection of a fully-automated atlas based knee mri segmentation method, 2010.

[17] M. Behr, L. Thollon, P.J. Arnoux, T. Serre, S.V. Berdah, P. Baque, and C. Brunet. 3d reconstruction of the diaphragm for virtual traumatology. *Surgical and Radiologic Anatomy*, 28(3):235–240, 2006.

[18] R. Beichel, H. Bischof, F. Leberl, and M. Sonka. Robust active appearance models and their application to medical image analysis. *Medical Imaging, IEEE Transactions on*, 24(9):1151–1169, 2005.

[19] R. Beichel, G. Gotschuli, E. Sorantin, F. Leberl, and M. Sonka. Diaphragm dome surface segmentation in ct data sets: a 3d active appearance model approach. *SPIE Proceedings, Medical Imaging 2002*, 4684:475–484, 2002.

[20] R. Beichel, S. Mitchell, E. Sorantin, F. Leberl, A. Goshtasby, and M. Sonka. Shape and appearance based segmentation of volumetric medical images. In *Image Processing, 2001. Proceedings. 2001 International Conference on*, volume 2, pages 589–592, 2001.

[21] T. Bo and J. Li. Preliminary analysis of thorax ct image pre-processing and 3d modeling of patients with pectus excavatum. *Advanced Materials Research*, 459:465–468, 2012.

[22] D. Bouros. *Pleural Disease*, volume 229 of *Lung Biology in Health and Disease*. Taylor and Francis Inc, New York, second edition, 2009.

[23] Y. Boykov and G. Funka-Lea. Graph cuts and efficient n-d image segmentation. *Int. J. Comput. Vision*, 70(2):109–131, November 2006.

[24] Y. Boykov and V. Kolmogorov. An experimental comparison of min-cut/max-flow algorithms for energy minimization in vision. *Pattern Analysis and Machine Intelligence, IEEE Transactions on*, 26(9):1124–1137, Sept 2004.

[25] Y. Boykov, O. Veksler, and R. Zabih. Markov random fields with efficient approximations. In *Computer Vision and Pattern Recognition, 1998. Proceedings. 1998 IEEE Computer Society Conference on*, pages 648–655, Jun 1998.

[26] Y. Boykov, O. Veksler, and R. Zabih. Fast approximate energy minimization via graph cuts. *Pattern Analysis and Machine Intelligence, IEEE Transactions on*, 23(11):1222–1239, Nov 2001.

[27] M.S. Brown, M.F. McNitt-Gray, N.J. Mankovich, J.G. Goldin, J. Hiller, L.S. Wilson, and D.R. Aberie. Method for segmenting chest ct image data using an anatomical model: preliminary results. *Medical Imaging, IEEE Transactions on*, 16(6):828–839, Dec 1997.

[28] V. Caselles, F. Catt, T. Coll, and F. Dibos. A geometric model for active contours in image processing. *Numerische Mathematik*, 66(1):1–31, 1993.

[29] V. Caselles, R. Kimmel, and G. Sapiro. Geodesic active contours. *International Journal of Computer Vision*, 22(1):61–79, 1997.

[30] K. Chaisaowong, C. Akkawutvanich, C. Wilkmann, and T. Kraus. A fully automatic probabilistic 3d approach for the detection and assessment of pleural thickenings from ct data. In *Computational Intelligence in Medical Imaging (CIMI), 2013 IEEE Fourth International Workshop on*, pages 14–21, April 2013.

[31] K. Chaisaowong, B. Bross, A. Knepper, T. Kraus, and T. Aach. Detection and follow-up assessment of pleural thickenings from 3d ct data. volume 1, pages 489–492, 2008.

[32] K. Chaisaowong, P. Jager, S. Vogel, A. Knepper, T. Kraus, and T. Aach. Computer-assisted diagnosis for early stage pleural mesothelioma: Automated extraction of pleura to detect pleural thickenings from thoracic ct images. In *Proc. International Workshop on Advanced Image Technology*, pages 229–234, Bangkok, January 8–9, 2007.

[33] K. Chaisaowong, S.K. Keller, and T. Kraus. Automatic spatiotemporal matching of detected pleural thickenings. volume 9069, 2014.

[34] K. Chaisaowong, A. Knepper, T. Kraus, and T. Aach. Application of supervised range-constrained thresholding to extract lung pleura for automated detection of pleural thickenings from thoracic ct images. volume 6514, 2007.

[35] K. Chaisaowong, N. Saekor, S. Roongruangsorakarn, T. Kraus, and T. Aach. Automatic 3d modeling of pleural thickening through thin plate spline interpolation. In *Electrical Engineering/Electronics, Computer, Telecommunications and Information Technology (ECTI-CON), 2011 8th International Conference on*, pages 1019–1022, May 2011.

[36] P. Chang, J.Y. Lai, J.C. Chen, and C.J. Wang. Quantitative evaluation of bone and cartilage changes after the ravitch thoracoplasty by multislice computed tomography with 3-dimensional reconstruction. *The Journal of Thoracic and Cardiovascular Surgery*, 134(5):1279 – 1283, 2007.

[37] M. Chen, J. Bai, and R.A.C. Siochi. A new method of diaphragm apex motion detection from 2d projection images of mega-voltage cone beam ct. *Physics in Medicine and Biology*, 58(3):715, 2013.

[38] Y. Chen, Z. Wang, J. Hu, W. Zhao, and Q. Wu. The domain knowledge based graph-cut model for liver {CT} segmentation. *Biomedical Signal Processing and Control*, 7(6):591 – 598, 2012. Biomedical Image Restoration and Enhancement.

[39] Z.G. Chu, J.Q. Yu, Z.G. Yang, L.Q. Peng, H.L. Bai, and X.M. Li. Correlation between sternal depression and cardiac rotation in pectus excavatum: Evaluation with helical ct. *American Journal of Roentgenology*, 195(1):W76–W80, 2010.

[40] Connexions. Alveolus diagram @ONLINE https://commons.wikimedia.org/wiki/file:alveolus-diagram.svg. [accessed: 04.july.2015].

[41] L.R. Dice. Measures of the amount of ecologic association between species. *Ecology*, 26(3):297–302, 1945.

[42] R.L. Drake, W. Vogl, A.W.M. Mitchell, and H. Gray. *Gray's Anatomy for Students.* Gray's Anatomy Series. Churchill Livingstone/Elsevier, 2010.

[43] J. Dworzak, H. Lamecker, J. von Berg, T. Klinder, C. Lorenz, D. Kainmller, H. Seim, H.C. Hege, and S. Zachow. 3d reconstruction of the human rib

cage from 2d projection images using a statistical shape model. *International Journal of Computer Assisted Radiology and Surgery*, 5(2):111–124, 2010.

[44] P. Faltin and K. Chaisaowong. 3d surface-based detection of pleural thickenings. *Acta Polytechnica*, 51(5):39–44, 2011.

[45] P. Faltin, K. Chaisaowong, T. Kraus, and T. Aach. Markov-gibbs model based registration of ct lung images using subsampling for the follow-up assessment of pleural thickenings. In *Image Processing (ICIP), 2011 18th IEEE International Conference on*, pages 2181–2184, Sept 2011.

[46] P. Faltin, K. Chaisaowong, T. Kraus, and D. Merhof. Consistent follow-up segmentation of pleural thickenings. In *Biomedical Imaging (ISBI), 2014 IEEE 11th International Symposium on*, pages 1368–1372, April 2014.

[47] A. Farag, J. Graham, and A. Farag. Robust segmentation of lung tissue in chest ct scanning. In *Image Processing (ICIP), 2010 17th IEEE International Conference on*, pages 2249–2252, Sept 2010.

[48] D.E. Fletcher and J.R. Edge. The early radiological changes in pulmonary and pleural asbestosis. *Clinical Radiology*, 21(4):355–365, 1970.

[49] M. Gargouri, J. Tierny, E. Jolivet, P. Petit, and E.D. Angelini. Accurate and robust shape descriptors for the identification of rib cage structures in ct-images with random forests. In *Biomedical Imaging (ISBI), 2013 IEEE 10th International Symposium on*, pages 65–68, April 2013.

[50] H. Gray, H. Ellis, B.K. Berkovitz, and S. Standring. *Gray's Anatomy, The Anatomical Basis of Clinical Practice*. Churchill Livingstone, New York, 39th edition, 2005.

[51] H. Gray and L. Warren Harmin. *Anatomy of the Human Body*. Bartleby, Philadelphia: Lea and Febiger, 20th edition, 2000.

[52] D.M. Greig, B.T. Porteous, and A.H. Seheult. Exact maximum a posteriori estimation for binary images. *Journal of the Royal Statistical Society*, 51:271–279, 1989.

[53] S. Grenier, S. Parent, and F. Cheriet. Personalized 3d reconstruction of the rib cage for clinical assessment of trunk deformities. *Medical Engineering & Physics*, 35(11):1651 – 1658, 2013.

[54] T.L. Guidotti, A. Miller, D. Christiani, G. Wagner, J. Balmes, P. Harber, C.A. Brodkin, W. Rom, G. Hillerdal, M. Harbut, and F.H.Y. Green. Diagnosis and initial management of nonmalignant diseases related to asbestos. *American Journal of Respiratory and Critical Care Medicine*, 170(6):691–715, 2004.

[55] S.S. Han and J.O.V. Holmstedt. *Human microscopic anatomy*. McGraw-Hill, 1981.

[56] H. Handels, T.M. Deserno, H.P. Meinzer, and T. Tolxdorff. Image analysis and modeling in medical image computing recent developments and advances. *Methods of Information in Medicine*, 51(5):395–397, 2012.

[57] R.M. Haralick and L.G. Shapiro. Image segmentation techniques. volume 548, pages 2–9, 1985.

[58] P. Harremoes, D. Gee, M. MacGarvin, A. Stirling, J. Keys, B. Wynne, and S.G. Vaz. *The Precautionary Principle in the 20th Century: Late Lessons from Early Warnings*. Taylor & Francis, 2013.

[59] T. Hastie and R. Tibshirani. Generalized additive models for medical research. *Statistical methods in medical research*, 4(3), 1995.

[60] G. Hillerdal. Non-malignant asbestos pleural disease. *Thorax*, 36(9):669–675, 1981.

[61] A.B. Holbrook and K.Butts Pauly. Segmentation of costal cartilage in abdominal ct data using watershed markers. *AIP Conference Proceedings*, 911(1):226–231, 2007.

[62] S. Holcombe, S. Ejima, H. Huhdanpaa, A. Jones, and S.C. Wang. Ribcage characterization for fe using automatic ct processing. In *Biomedical Imaging: From Nano to Macro, 2008. ISBI 2008. 5th IEEE International Symposium on*, pages 648–651, May 2008.

[63] S. Hu, E.A. Hoffman, and J.M. Reinhardt. Automatic lung segmentation for accurate quantitation of volumetric x-ray ct images. *Medical Imaging, IEEE Transactions on*, 20(6):490–498, June 2001.

[64] P. Hua, Q. Song, M. Sonka, E.A. Hoffman, and J.M. Reinhardt. Segmentation of pathological and diseased lung tissue in ct images using a graph-search algorithm. In *Biomedical Imaging: From Nano to Macro, 2011 IEEE International Symposium on*, pages 2072–2075, March 2011.

[65] D.P. Huttenlocher and K. Kedem. Computing the minimum hausdorff distance for point sets under translation. In *Proceedings of the Sixth Annual Symposium on Computational Geometry*, SCG '90, pages 340–349, New York, NY, USA, 1990. ACM.

[66] D.P. Huttenlocher, G.A. Klanderman, and W.J. Rucklidge. Comparing images using the hausdorff distance. *Pattern Analysis and Machine Intelligence, IEEE Transactions on*, 15(9):850–863, Sep 1993.

[67] J.N. Kaftan, A. Bakai, M. Dasc, and T. Aach. Locally adaptive fuzzy pulmonary vessel segmentation in contrast enhanced ct data. In *Biomedical Imaging: From Nano to Macro, 2008. ISBI 2008. 5th IEEE International Symposium on*, pages 101–104, May 2008.

[68] L. Kang, W. Xiaodong, D.Z. Chen, and M. Sonka. Optimal surface segmentation in volumetric images-a graph-theoretic approach. *Pattern Analysis and Machine Intelligence, IEEE Transactions on*, 28(1):119–134, 2006.

[69] M. Kass, A. Witkin, and D. Terzopoulos. Snakes: Active contour models. *International Journal of Computer Vision*, 1(4):321–331, 1988.

[70] S. Kidd. How to activate your diaphragm to improve breathing and performance @ONLINE url:http://breakingmuscle.com/cycling/how-to-activate-your-diaphragm-to-improve-breathing-and-performance. [accessed: 24.jan.2015].

[71] S. Kido and A. Tsunomori. Automated extraction of pleural effusion of three-dimensional thoracic ct images. In *Progress in Biomedical Optics and Imaging Proceedings of SPIE*, volume 7260, 2009.

[72] H. Kim, J.H. Hwang, S.Y. Lim, J.K. Pyon, G.H. Mun, S.I. Bang, S.H. Choi, and K.S. Oh. Preoperative rib cartilage imaging in 3-dimensional chest computed tomography for auricular reconstruction for microtia. *Annals of Plastic Surgery, Recunstructive Surgery*, pages 1–7, 2012.

[73] T. Klinder, C. Lorenz, J. von Berg, S.P.M. Dries, T. Blow, and J. Ostermann. Automated model-based rib cage segmentation and labeling in ct images. In Nicholas Ayache, Sbastien Ourselin, and Anthony Maeder, editors, *Medical Image Computing and Computer-Assisted Intervention MICCAI 2007*, volume 4792 of *Lecture Notes in Computer Science*, pages 195–202. Springer Berlin Heidelberg, 2007.

[74] T. Klinder, J. Ostermann, M. Ehm, A. Franz, R. Kneser, and C. Lorenz. Automated model-based vertebra detection, identification, and segmentation in {CT} images. *Medical Image Analysis*, 13(3):471 – 482, 2009.

[75] C. Koehler and T. Wischgoll. Knowledge-assisted reconstruction of the human rib cage and lungs. *IEEE Comput. Graph. Appl.*, 30(1):17–29, January 2010.

[76] P. Korfiatis, S. Skiadopoulos, P. Sakellaropoulos, C. Kalogeropoulou, and L. Costaridou. Combining 2d wavelet edge highlighting and 3d thresholding for lung segmentation in thin-slice ct. *British Journal of Radiology*, 80(960):996–1005, 2007.

[77] Ashish K.R., Ananda S.C., A. Elnakib, F. Khalifa, A. Soliman, G. Beache, and A. El-Baz. Kidney segmentation using graph cuts and pixel connectivity. *Pattern Recognition Letters*, 34(13):1470 – 1475, 2013.

[78] H. Ladjal, J. Saade, M. Beuve, J. Azencot, J.M. Moreau, and B. Shariat. 3d biomechanical modeling of the human diaphragm based on ct scan images. In Mian Long, editor, *World Congress on Medical Physics and Biomedical*

Engineering May 26-31, 2012, Beijing, China, volume 39 of *IFMBE Proceedings*, pages 2188–2191. Springer Berlin Heidelberg, 2013.

[79] LadyofHats. Planes of body, copyright: Connexions web site (http://cnx.org) @ONLINE http://commons.wikimedia.org/wiki/file:planes of body.jpg. [accessed: 25.april.2015].

[80] J.K. Leader, B. Zheng, R.M. Rogers, F.C. Sciurba, A. Perez, B.E. Chapman, S. Patel, C.R. Fuhrman, and D. Gur. Automated lung segmentation in x-ray computed tomography: Development and evaluation of a heuristic threshold-based scheme. *Academic Radiology*, 10(11):1224–1236, 2003.

[81] J. Lee and A.P. Reeves. Segmentation of individual ribs from low-dose chest ct, 2010.

[82] B. Li and J.M. Reinhardt. Automatic generation of object shape models and their application to tomographic image segmentation, 2001.

[83] C. Li, X. Wang, S. Eberl, M. Fulham, Y. Yin, and D. Feng. Fully automated liver segmentation for low- and high- contrast ct volumes based on probabilistic atlases. In *Image Processing (ICIP), 2010 17th IEEE International Conference on*, pages 1733–1736, Sept 2010.

[84] Q. Li, F. Li, and K. Doi. Computerized detection of lung nodules in thin-section ct images by use of selective enhancement filters and an automated rule-based classifier. *Academic Radiology*, 15(2):165–175, 2008.

[85] R.W. Light. *Pleural Diseases*. Wolters Kluwer/Lippincott Williams and Wilkins Health, Philadelphia, sixth edition, 2013.

[86] P.J. Lynch. Lungs, simple diagram of lungs and trachea @ONLINE http://commons.wikimedia.org/wiki/file:lungs diagram simple.svg. [accessed: 25.april.2015].

[87] E.N. Marieb, K. Hoehn, and M. Hutchinson. *Human Anatomy and Physiology*. Pearson Education, Limited, 2014.

[88] S.J. Martin, J. Dey, M.A. King, and B.F. Hutton. Segmenting and tracking diaphragm and heart regions in gated-ct datasets as an aid to developing a predictive model for respiratory motion-correction. In *Nuclear Science Symposium Conference Record, 2007. NSS '07. IEEE*, volume 4, pages 2680–2685, 2007.

[89] J.R. McClelland, D.J. Hawkes, T. Schaeffter, and A.P. King. Respiratory motion models: A review. *Medical Image Analysis*, 17(1):19 – 42, 2013.

[90] S.J. McQuaid, T. Lambrou, V.J. Cunningham, V. Bettinardi, M.C. Gilardi, and B.F. Hutton. The application of a statistical shape model to diaphragm tracking in respiratory-gated cardiac pet images. *Proceedings of the IEEE*, 97(12):2039–2052, Dec 2009.

[91] S.J. McQuaid, T. Lambrou, and B.F. Hutton. A novel method for incorporating respiratory-matched attenuation correction in the motion correction of cardiac petct studies. *Physics in Medicine and Biology*, 56(10):2039–2052, 2011.

[92] A. Mehnert and P. Jackway. An improved seeded region growing algorithm. *Pattern Recognition Letters*, 18(10):1065 – 1071, 1997.

[93] G. Meurant. *Asbestos and Disease*. Environmental sciences. Elsevier Science, 2012.

[94] J. Milenkovia, O. Chambers, Marolt M., and J.F. Tasia. Automated breast-region segmentation in the axial breast mr images. *Computers in Biology and Medicine*, 62:55–64, 2015.

[95] S.E. Miles, A. Sandrini, A.R. Johnson, and D.H. Yates. Clinical consequences of asbestos-related diffuse pleural thickening: A review. *Journal of Occupational Medicine and Toxicology*, 3(1), 2008.

[96] M. Mohr, E. Abrams, C. Engel, Long W.B., and M. Bottlang. Geometry of human ribs pertinent to orthopedic chest-wall reconstruction. *Journal of Biomechanics*, 40(6):1310 – 1317, 2007.

[97] K.L. Moore, A.F. Dalley, and A.M.R. Agur. *Clinically Oriented Anatomy.* Clinically Oriented Anatomy. Wolters Kluwer Health, 2013.

[98] A.H. J. Moreira, P.L. Rodrigues, J. Fonseca, A.C.M. Pinho, N.F. Rodrigues, J. Correia-Pinto, and J.L. Vilaa. Pectus excavatum postsurgical outcome based on preoperative soft body dynamics simulation, 2012.

[99] Geoffrey M.G.and Muhammad N. The anatomy of the ribs and the sternum and their relationship to chest wall structure and function. *Thoracic Surgery Clinics*, 17(4):473 – 489, 2007. Thoracic Anatomy, Part I Chest Wall, Airway, Lungs.

[100] K. Nakagomi, A. Shimizu, H. Kobatake, M. Yakami, K. Fujimoto, and K. Togashi. Multi-shape graph cuts with neighbor prior constraints and its application to lung segmentation from a chest {CT} volume. *Medical Image Analysis*, 17(1):62 – 77, 2013.

[101] F.H. Netter. *Atlas of Human Anatomy.* Netter Basic Science. Elsevier Health Sciences, 39th edition, 2014.

[102] Y. Noorda, L. Bartels, and J. Pluim. Segmentation of the cartilage in the rib cage in 3d mri. In Hiroyuki Yoshida, David Hawkes, and MichaelW. Vannier, editors, *Abdominal Imaging. Computational and Clinical Applications*, volume 7601 of *Lecture Notes in Computer Science*, pages 229–237. Springer Berlin Heidelberg, 2012.

[103] M.P.M. Pato, N.J.G. Santos, P. Areias, E.B. Pires, M. de Carvalho, S. Pinto, and D.S. Lopes. Finite element studies of the mechanical behaviour of the diaphragm in normal and pathological cases. *Computer Methods in Biomechanics and Biomedical Engineering*, 14(6):505–513, 2011.

[104] B. Pazokifard and A. Sowmya. 3-d segmentation of human sternum in lung mdct images. In *Engineering in Medicine and Biology Society (EMBC), 2013 35th Annual International Conference of the IEEE*, pages 3351–3354, July 2013.

[105] B. Pazokifard and A. Sowmya. Efficient graph cuts based extraction of vertebral column and ribs in lung mdct images. In *Image Processing (ICIP), 2013 20th IEEE International Conference on*, pages 1182–1186, Sept 2013.

[106] B. Pazokifard and A. Sowmya. Lung segmentation with graph cuts: Graph size versus performance. *AIP Conference Proceedings*, 1559(1):315–322, 2013.

[107] B. Pazokifard, A. Sowmya, and D. Moses. Automatic patient-customised 3d reconstruction of human costal cartilage from lung mdct dataset. *International Journal of Computer Assisted Radiology and Surgery*, pages 1–8, 2014.

[108] B. Pazokifard, A. Sowmya, and D. Moses. Patient-customized 3d reconstruction of human ribs from lung mdct dataset. In *Biomedical Imaging (ISBI), 2014 IEEE 11th International Symposium on*, pages 1131–1135, April 2014.

[109] B. Pazokifard, A. Sowmya, and D. Moses. Automatic 3d modelling of human diaphragm from lung mdct images. *International Journal of Computer Assisted Radiology and Surgery (under revision)*, 2015.

[110] S. Petkov, X. Carrillo, P. Radeva, and C. Gatta. Diaphragm border detection in coronary x-ray angiographies: New method and applications. *Computerized Medical Imaging and Graphics*, 38(4):296 – 305, 2014.

[111] D.L. Pham, C. Xu, and J.L. Prince. Current methods in medical image segmentation. *Annual Review of Biomedical Engineering*, 2(2000):315–337, 2000.

[112] S. Prazakova, P.S. Thomas, A. Sandrini, and D.H. Yates. Asbestos and the lung in the 21st century: an update. *The Clinical Respiratory Journal*, 8(1):1–10, 2014.

[113] S. Ramakrishnan, C. Alvino, L. Grady, and A. Kiraly. Automatic three-dimensional rib centerline extraction from ct scans for enhanced visualization and anatomical context. *Proc. SPIE 7962, Medical Imaging 2011: Image Processing*, pages 79622X–1–79622X–12, 2011.

[114] R.M. Rangayyan, S. Banik, and G.S. Boag. Landmarking and segmentation of computed tomographic images of pediatric patients with neuroblastoma. *International Journal of Computer Assisted Radiology and Surgery*, 4(3):245–262, 2009.

[115] R.M. Rangayyan, R.H. Vu, and G.S. Boag. Automatic delineation of the diaphragm in computed tomographic images. *Journal of Digital Imaging*, 21(1):134–147, 2008.

[116] K.J. Rechowicz and F.D. McKenzie. A strategy for simulating and validating the nuss procedure for the minimally invasive correction of pectus excavatum. In *(BMEI)*, volume 4, pages 2370 –2374, oct. 2011.

[117] M. Rudrapatna, V. Mai, A. Sowmya, and P. Wilson. Knowledge-driven automated detection of pleural plaques and thickening in high resolution ct of the lung. In GaryE. Christensen and Milan Sonka, editors, *Information Processing in Medical Imaging*, volume 3565 of *Lecture Notes in Computer Science*, pages 270–285. Springer Berlin Heidelberg, 2005.

[118] B. Sandoz, A. Badina, S. Laporte, K. Lambot, D. Mitton, and W. Skalli. Quantitative geometric analysis of rib, costal cartilage and sternum from childhood to teenagehood. *Medical and Biological Engineering and Computing*, 51(9):971–979, 2013.

[119] I.J. Selikoff. The occurrence of pleural calcification among asbestos insulation workers. *Annals of the New York Academy of Sciences*, 132(1):351–367, 1965.

[120] H. Shen, L. Liang, M. Shao, and S. Qing. Tracing based segmentation for the labeling of individual rib structures in chest ct volume data. In Christian Barillot, DavidR. Haynor, and Pierre Hellier, editors, *Medical Image Computing and Computer-Assisted Intervention MICCAI 2004*, volume 3217 of *Lecture Notes in Computer Science*, pages 967–974. Springer Berlin Heidelberg, 2004.

[121] H. Shi and Q. Liu. To generate a finite element model of human thorax using the vch dataset. volume 7496, 2009.

[122] T.W. Shields, J. LoCicero, C.E. Reed, and R.H. Feins. *General Thoracic Surgery.* Number v. 1 in General Thoracic Surgery. Wolters Kluwer Health/Lippincott Williams & Wilkins, 2009.

[123] H. Shikata, G. McLennan, E.A. Hoffman, and M. Sonka. Segmentation of pulmonary vascular trees from thoracic 3d ct images. *Journal of Biomedical Imaging*, 2009:24:1–24:11, January 2009.

[124] A. Shimizu, K. Nakagomi, T. Narihira, H. Kobatake, S. Nawano, K. Shinozaki, K. Ishizu, and K. Togashi. Automated segmentation of 3d ct images based on statistical atlas and graph cuts. In *Proceedings of the 2010 International MICCAI Conference on Medical Computer Vision: Recognition Techniques and Applications in Medical Imaging*, MCV'10, pages 214–223, Berlin, Heidelberg, 2011. Springer-Verlag.

[125] A.F.D Silva, J.S. Silva, B.S. Santos, and C. Ferreira. Fast pulmonary contour extraction in x-ray ct images: a methodology and quality assessment, 2001.

[126] I. Sluimer, A. Schilham, M. Prokop, and B. Ginneken. Computer analysis of computed tomography scans of the lung: a survey. *Medical Imaging, IEEE Transactions on*, 25(4):385–405, April 2006.

[127] I.C. Sluimer, M. Niemeijer, and B. Ginneken. Lung field segmentation from thin-slice ct scans in presence of severe pathology, 2004.

[128] R.S. Snell. *Clinical Anatomy by Systems.* M - Medicine Series. Lippincott Williams & Wilkins, 2007.

[129] M. Sonka and J.M. , Fitzpatrick. *Medical Image Processing and Analysis*, volume 2 of *Handbook of Medical Imaging.* SPIE, 2009.

[130] T. Sorensen. *A Method of Establishing Groups of Equal Amplitude in Plant Sociology Based on Similarity of Species Content and Its Application to Analyses of the Vegetation on Danish Commons.* Biologiske Skrifter // Det Kongelige Danske Videnskabernes Selskab. I kommission hos E. Munksgaard, 1948.

[131] J. Staal, B. van Ginneken, and M.A. Viergever. Automatic rib segmentation and labeling in computed tomography scans using a general framework for detection, recognition and segmentation of objects in volumetric data. *Medical Image Analysis*, 11(1):35 – 46, 2007.

[132] E.J. Stern, S.J. Swensen, and J.P. Kanne. *High-Resolution CT of the Chest: Comprehensive Atlas.* Wolters Kluwer Health, 2012.

[133] M. Stojkovic, J. Milovanovic, N. Vitkovic, M. Trajanovic, N. Grujovic, V. Milivojevic, S. Milisavljevic, and S. Mrvic. Reverse modeling and solid free-form fabrication of sternum implant. *Australasian Physical & Engineering Sciences in Medicine*, 33(3):243–250, 2010.

[134] S. Sun, C. Bauer, and R. Beichel. Automated 3-d segmentation of lungs with lung cancer in ct data using a novel robust active shape model approach. *Medical Imaging, IEEE Transactions on*, 31(2):449–460, Feb 2012.

[135] D. Terzopoulos, A. Witkin, and M. Kass. Symmetry-seeking models and 3d object reconstruction. *International Journal of Computer Vision*, 1:211–221, 1987.

[136] J. Van Cleemput, H. De Raeve, J.A. Verschakelen, J. Rombouts, L.M. Lacquet, and B. Nemery. Surface of localized pleural plaques quantitated by computed tomography scanning: No relation with cumulative asbestos exposure and no effect on lung function. *American Journal of Respiratory and Critical Care Medicine*, 163(3 I):705–710, 2001.

[137] A. Vaziri, H. Nayeb-Hashemi, and B. Akhavan-Tafti. Computational model of rib movement and its application in studying the effects of age-related thoracic cage calcification on respiratory system. *Computer Methods in Biomechanics and Biomedical Engineering*, 13(2):257–264, 2010. PMID: 19927242.

[138] S.S. Vedam, V.R. Kini, P.J. Keall, V. Ramakrishnan, H. Mostafavi, and R. Mohan. Quantifying the predictability of diaphragm motion during respiration with a noninvasive external marker. *Medical Physics*, 30(4):505–513, 2003.

[139] F.P. Vidal, P.F. Villard, and E. Lutton. Tuning of patient-specific deformable models using an adaptive evolutionary optimization strategy. *Biomedical Engineering, IEEE Transactions on*, 59(10):2942–2949, Oct 2012.

[140] P.F. Villard, W. Bourne, and F. Bello. Modelling organ deformation using mass-springs and tensional integrity. In Fernando Bello and P.J.Eddie Edwards, editors, *Biomedical Simulation*, volume 5104 of *Lecture Notes in Computer Science*, pages 221–226. Springer Berlin Heidelberg, 2008.

[141] M.R. Villarreal. Diagram of a human female skeleton @ONLINE url:http://commons.wikimedia.org/wiki/file:human-skeleton-front-en.svg. [accessed: 23.jan.2015], 2007.

[142] P. Vostatek, D. Novak, T. Rychnovsk, and J. Wild. Diaphragm postural function analysis using magnetic resonance. In *Information Technology and Applications in Biomedicine (ITAB), 2010 10th IEEE International Conference on*, pages 1–4, Nov 2010.

[143] J. Wang, F. Li, and Q. Li. Automated segmentation of lungs with severe interstitial lung disease in ct. *Medical Physics*, 36(10):4592–4599, 2009.

[144] Q. Wang, Q. Chang, Y. Qiao, Y. Zhu, G. Huang, and J. Yang. Knowledge-based segmentation of spine and ribs from bone scintigraphy. In Bao-Liang Lu, Liqing Zhang, and James Kwok, editors, *Neural Information Processing*, volume 7062 of *Lecture Notes in Computer Science*, pages 241–248. Springer Berlin Heidelberg, 2011.

[145] W. Wen-dong, S. Yi-kai, W. Huan, and Y. Li-na. Research on biomechanical model of children with pectus excavatum. In *Biomedical Engineering and Informatics, 2009. BMEI '09. 2nd International Conference on*, pages 1–4, Oct 2009.

[146] D. Wu, D. Liu, Z. Puskas, C. Lu, A. Wimmer, C. Tietjen, G. Soza, and S.K. Zhou. A learning based deformable template matching method for automatic rib centerline extraction and labeling in ct images. In *Computer Vision and*

Pattern Recognition (CVPR), 2012 IEEE Conference on, pages 980–987, June 2012.

[147] R. Yalamanchili, D. Chittajallu, P. Balanca, B. Tamarappoo, D. Berman, D. Dey, and I. Kakadiaris. Automatic segmentation of the diaphragm in non-contrast ct images. In *Biomedical Imaging: From Nano to Macro, 2010 IEEE International Symposium on*, pages 900–903, April 2010.

[148] L. Zhang and Q. Li, X.and Hu. Automatic rib segmentation in chest ct volume data. In *Biomedical Engineering and Biotechnology (iCBEB), 2012 International Conference on*, pages 750–753, May 2012.

[149] B. Zheng, J.K. Leader, G.S. Maitz, B.E. Chapman, C.R. Fuhrman, R.M. Rogers, F.C. Sciurba, A. Perez, P. Thompson, W.F. Good, and D. Gur. A simple method for automated lung segmentation in x-ray ct images, 2003.

[150] X. Zhou, H. Ninomiya, T. Hara, H. Fujita, R. Yokoyama, H. Chen, T. Kiryu, and H. Hoshi. Automated estimation of the upper surface of the diaphragm in 3-d ct images. *Biomedical Engineering, IEEE Transactions on*, 55(1):351–353, 2008.

[151] K.H. Zou, S.K. Warfield, A. Baharatha, C. Tempany, M.R. Kaus, S.J. Haker, W.M. Wells, F.A. Jolesz, and R. Kikinis. Statistical validation of image segmentation quality based on a spatial overlap index. *Academic Radiology*, 11:178–189, 2004.

[152] S.W. Zucker. Region growing: Childhood and adolescence. *Computer Graphics and Image Processing*, 5(3):382 – 399, 1976.

Appendix A

Followings are pseudo code for slice by slice removing the artefacts and extraneous pixels around the patient's body from the original MDCT dataset:

input:

$\mathbb{MDCT}_{x,y,z} = \{s_1, s_2, ... s_n\}$,

where {

$s_i = slice\#i$ *of MDCT dataset in intensity format,*

$x, y = dimension$ *of CT slice,*

$n = number$ *of slices in the MDCT dataset,*

$z = n$

}

initialize:

$S = 0_{x,y}$,

$\mathbb{BODY} = 0_{x,y,z}$,

$\mathbb{BODY}_{x,y,z} = \{b_1, b_2, ... b_n\}$,

$\mathbb{T} = 0_{x,y,z}$ *(as trimmed dataset),*

$\mathbb{T}_{x,y,z} = \{t_1, t_2, ... t_n\}$,

Threshhold = mean intensity of the patient's muscle

main: {

for (i = 1; i<= n; i ++) {

$S = Threshhold < s_i$,

$b_i = S$

}

$\mathbb{BODY} = $ *biggest component of* $\mathbb{BODY}$,

```
for (i = 1; i<= n; i ++) {
```

$$t_i = s_i \ . * b_i,$$

where $.*$ represents multiply the corresponding elements of two matrices

```
    }
}
```

Appendix B

Followings are pseudo code for identifying the lungs in segmentation result, using the graph cut algorithm:

input:

$\mathbb{R}_{x,y,z} = \{r_1,\ r_2,\ ... r_n\},$

where {

$r_i = result\ graph\ cut\ on\ slice\#i\ of\ the\ MDCT\ dataset$

$x, y = dimension\ of\ CT\ slice,$

$n = number\ of\ slices\ in\ the\ MDCT\ dataset,$

$z = n$

}

initialize:

$I = 0_{x,y},$

main: {

for (i = 1; i<= n; i ++) {

invert $r_i,$

$I = r_i\ with\ filled\ holes,$

where .* represents multiply the corresponding elements of two matrices

}

$\mathbb{R} = biggest\ component\ of\ \mathbb{R},$

for (i = 1; i<= n; i ++) {

fill the holes in $r_i,$

}

}

Appendix C

Followings are pseudo code for removing the scapula and the clavicle from segmented chest bone in 3D:

input:

$\mathbb{BONE}_{x,y,z} = \{s_1, \ s_2, \ ... \ s_n\}$

where {

    s_i=*binary slide#i (segmented bone=1),*

    x, y=*dimension of CT slice,*

    $n =$ *number of slices in the MDCT dataset,*

    z=n

}

initialize:

    $i = 0,$

    $N_0 = 0,$

    $\mathbb{O} = 0_{x,y},$

main: {

  for interval=[1 : y/5 , 4 × y/5 : y] {

    while ($N_0 = 0$ & $i \leqslant z$) {

    i++

    detect s_i(:,interval),

    $N_0 =$ *number of detected pixels equal to 1*

  }

  Object = detected pixels equal to 1 in s_i,

  $\mathbb{O}$ *(Object)=1,*

$C=$ *centre of the Object in* $\mathbb{O}$,

$N_1 = N_0$,

$N_2 = N_0$,

s_i *(Object)* $= 0$,

$i{+}{+}$

while $(N_2 \leqslant N_1 \times 2 \,\&\, i \leqslant z)$ {

  $N_1 = N_2$,

  start from C, detect pixels equal to 1 in s_i *using* $\mathbb{RG}^*$,

  Object = detected pixels,

  N_2 *= number of detected pixels*,

  $\mathbb{O}$ *(Object)* $= 1$,

  $C=$ *centre of the Object in* $\mathbb{O}$,

  s_i *(Object)* $= 0$,

  $i{+}{+}$

  }

 }

$\mathbb{RG}^*$: Region Growing algorithm

Appendix D

Followings are pseudo code for merging and unifying the diaphragm top and side boundaries in 3D:

input:

$\mathbb{TB}_{x,y,z} = \{t_1,\ t_2,\ ...,\ t_n\}$ *(* $\mathbb{TB}$*: top boundary),*

$\mathbb{SB}_{x,y,z} = \{s_1,\ s_2,\ ...,\ s_n\}$ *(* $\mathbb{SB}$*: side boundary),*

$\mathbb{UB} = 0_{x,y,z}$ *(* $\mathbb{UB}$*: unified boundary),*

$\mathbb{UB}_{x,y,z} = \{u_1,\ u_2,\ ...,\ u_n\}$

where {

$t_i = $ *binary slice #i,*

$s_i = $ *binary slice #i,*

$u_i = $ *unified boundary slice #i,*

$x, y = $ *dimension of CT slice,*

$z = n : $ *#of slices per dataset*

}

initialize:

$p = 1$

main:

while { $p \leqslant z$

$u_p = t_p\ +\ s_p,$

$p\ ++$

}

convert $\mathbb{UB}_{x,y,z}$ *to logic format*

Appendix E

Followings are pseudo code for removing diaphragmatic irrelevant voxels from the expanded active contour in 3D:

input:

$\mathbb{TB}_{x,y,z} = \{t_1, t_2, ..., t_n\}$,

$\mathbb{SB}_{x,y,z} = \{s_1, s_2, ..., s_n\}$,

$\mathbb{UB}_{x,y,z} = \{u_1, ..., u_n\}$,

$\mathbb{EB} = 0_{x,y,z}$ *(*$\mathbb{EB}$*: encompassing boundary)*,

$\mathbb{EB}_{x,y,z} = \{e_1, e_2, ..., e_n\}$,

$\mathbb{IU} = 0_{x,y}$,

$\mathbb{IS} = 0_{x,y}$,

$\mathbb{I} = 0_{x,y}$

main:

step 1:

```
for (p = 1; p<= x; p++) {
    for (q = 1; q<= y; q++) {
        find w : t_w(p, q) ≠ 0,
            UB_{p,q,1:w-1} = 0
    }
}
```

step 2:

```
for (p = 1; p<= z; p++) {
    IU=u_p,
    fill holes of IU,
```

$$\mathbb{IS} = s_p,$$

fill holes of $\mathbb{IS}$,

$$\mathbb{I} = \mathbb{IU} \cap \mathbb{IS},$$

$$e_p = \mathbb{I}$$

}

$$\mathbb{IS} = s_p,$$

fill holes of $\mathbb{IS}$,

$$\mathbb{I} = \mathbb{IU} \cap \mathbb{IS},$$

$$e_p = \mathbb{I}$$

Appendix F

Following is pseudo code to identify pleural costal surfaces from segmented lung in 3D:

   input:

     $\mathbb{LUNG}_{x,y,z} = \{s_1, \ s_2, \ ... \ s_n\}$

       where s_i=binary slide#i (segmented lung=1),

          x,y=dimension of CT slice,

          z=n

   initialize:

     $\mathbb{V} = 0_{x,y,z}$

     $\mathbb{VP} = 0_{x,y,z}$ *($\mathbb{VP}$: matrix of pleura)*

   main: {

    for (i = 1; i<= n; i++) {

      I=s_i ,

      I_p=perimeter I,

      I_c=covexhull of I_p,

      I_{dc}=dilated I_c,

      $\mathbb{V}_{:,:,i}$=I_p-I_{dc},

    }

    $\mathbb{V}'$=$\mathbb{V}$ biggest component in 3D

    for (i = 1; i<= n; i++) {

      I=s_i ,

      I_f=holes filled I,

      I_p=perimeter I_f,

      $\mathbb{VP}_{:,:,i}$=I_p-$\mathbb{V}'_{:,:,i}$

    }

   }

Appendix G

Followings are steps to find the vertebral column mid-sagittal plane from segmented chest bone slices:

  (i) build up segmented chest bone in 3D from axial slices

  (ii) ignore half-front of the segmented chest bone (Figure G.1a)

  (iii) map all coronal planes into a binary 2D plane (Figure G.1b)

  (iv) find the column on the binary 2D image that has the most non-zero pixels or if there is more than one column having highest number of non-zero pixels, choose the middle column (dashed line in Figure G.1b)

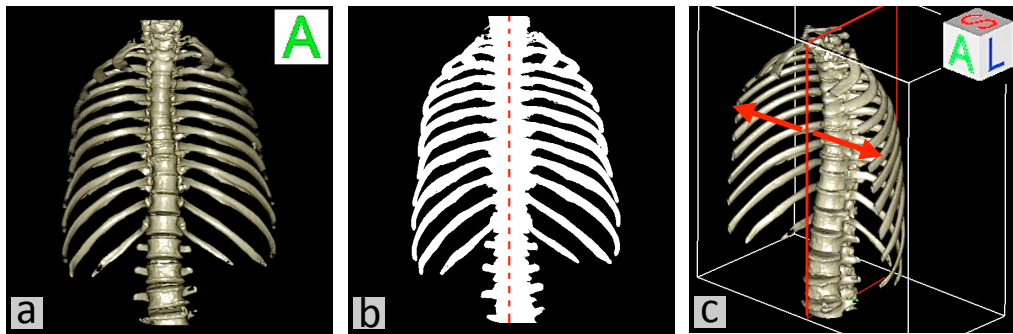 (v) map the chosen column in sagittal direction as tracing base (Figure G.1c)

Figure G.1: Steps to find the vertebral column mid-sagittal plane.

Appendix H

According to an anatomy study that examined ribs from fresh frozen human cadavers [96], human rib's cross-sectional shape varies along the length. Exemplary cross-sections at 5%, 25%, 50% and 75% of rib length are shown in Figure 4.2, if a rib length is defined as 0% at tubercle and 100% at CCJ.

In order to find δ, the number of sections needed to reconstruct the cut rib in 3D, a rib is modelled in cylindrical coordinate system. If θ_{rib} is the rib's orientation from tubercle to CCJ and $\theta_{tubercle}$ and θ_{CCJ} are orientations of two rib subsections, as shown in Figure H.1, then:

$$\delta = 100 \times (1 - (\theta_{tubercle} + \theta_{CCJ})/\theta_{rib}) \tag{H.1}$$

Moreover, if $\underset{m}{\overset{n}{\mathbb{S}}}(\Delta) = \{s_i,\, i = m+1, m+2, ..., n\}$ denotes a set of cross-sections for 3D modelling of Δ (one piece curved object e.g. rib) in $n - m$ sections, then

$$\underset{0}{\overset{100}{\mathbb{S}}}(rib) = \{s_r, r = 1, 2, ..., 100\} \tag{H.2}$$

$$\underset{0}{\overset{P}{\mathbb{S}}}(tubercle) = \{s_p, p = 1, 2, ..., P\}, \mathbb{S}(tubercle) \in \mathbb{S}(rib) \tag{H.3}$$

$$\underset{Q}{\overset{100}{\mathbb{S}}}(CCJ) = \{s_q, q = Q+1, Q+2, ..., 100\}, \mathbb{S}(CCJ) \in \mathbb{S}(rib) \tag{H.4}$$

then

$$\underset{P}{\overset{Q}{\mathbb{S}}}(cut) = \{s_k, k = P+1, P+2, ..., Q\}, \mathbb{S}_{cut} \in \mathbb{S}_{rib} \tag{H.5}$$

and also

$$\delta = Q - p \tag{H.6}$$

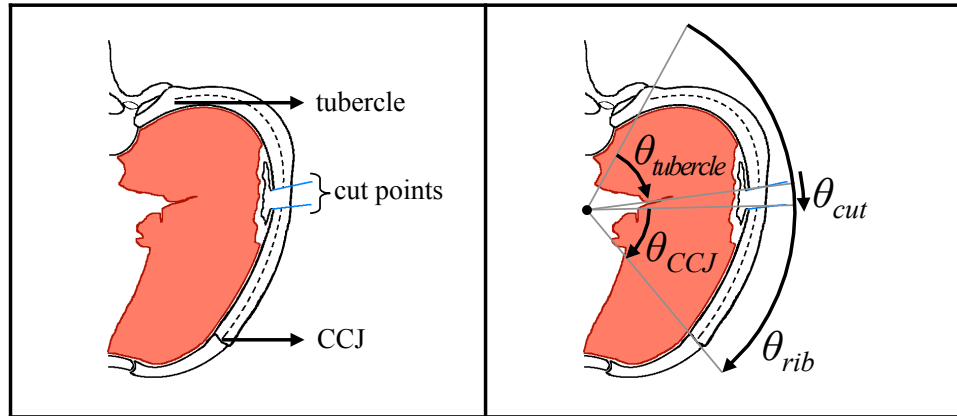The notable point is that each section is not necessarily equal to one degree. For

Figure H.1: Calculating the θ_{cut} (degree) and δ (number of sections), needed to reconstruct a piece of rib.

example if $\theta_{rib}=150°$, then there is 1.5° between two consecutive sections and 20 cross-sections are needed to build a cut rib with $\theta_{cut}=30°$.